The Effect of Near-Well Heterogeneity on Spatial Distribution of Salt Precipitation During CO_2 Injection

Tuva Maria Hovland Graham

Integrated Master's Program in Energy at Geophysical Institute

Department of Physics and Technology
University of Bergen, Norway

June, 2024

Acknowledgements

I want to thank my supervisor Prof. Martin Fernø at the Department of Physics and Technology at the University of Bergen, for his guidance and valuable discussions around the topic of this thesis. I would also like to thank my co-supervisor Dr. Sarah Eileen Gasda at NORCE for her availability, and for lending her expertise through this process. Thank you to both for the opportunity to work on this project.

I would like to thank Dr. David Landa Marban for his help with OPM, and for providing me with the configuration- and input files. Thank you for taking time to help me with the problems that occurred, and for teaching me about the simulator. I would also like to thank Benyamine Benali for the IT support in the starting phase of this project.

Thank you to Magnus Moldekleiv for contribution of knowledge and valuable discussions around OPM and this year.

Finally, thank to my husband Joel Graham and the rest of my family for always supporting and believing in me.

Tuva Maria Hovland Graham
Bergen, June 2024

Abstract

The world is in need of a shift to cleaner energy, and carbon storage is expected to be an important part of the transition. Geological carbon storage is a process in which captured carbon dioxide (CO_2) is injected into the subsurface for storage. There are several trapping mechanisms operating at different timescales which prevents the CO_2 from leaking back to the surface. Saline aquifers, which are reservoirs filled with formation brine, are good options for storage as they offer high storage capacity. A problem when storing CO_2 in such reservoirs is that the salinity in the brine can cause salt to precipitate, when water evaporates into the CO_2, which can effect injectivity.

This project investigated how the degree of heterogeneity affected the spatial distribution of salt precipitation during CO_2 injection. Numerical simulations were performed using OPM Flow, and two models were utilized. First, a 3D model where results were plotted in 2D with a focus near the injection well. To plot the 2D results, provided configuration files were utilized, which set the simulations and created input files. Several runs were simulated with different permeabilities, as well as different orders and numbers of layers. Half of the runs were simulated with salt precipitation included and half of the runs with it excluded, to compare the distribution of the injected CO_2. In the second model, two homogeneous cases based on the 2D geometry of the SPE CSP 11B benchmark model were simulated. One case with salt precipitation was compared to one without salt precipitation.

The results demonstrated that in homogeneous and slightly heterogeneous systems, greater blockage occurred next to the injection well. This affected injectivity of CO_2 into the layers where salt had clogged the well. A higher bottom hole pressure when compared to more heterogeneous runs was also observed. When the degree of heterogeneity was large, salt precipitated in the high permeability layers. As they provide better flow capacities, capillary backflow had a better effect in these layers. The homogeneous runs provided unexpected locations of the dry-out zone, which could be because of errors in the numerical simulations. More studies could be performed to investigate the effect on CO_2 distribution with temperature variations. Additionally, studies on varying degrees of heterogeneity in the 3D grid of the SPE CSP 11C benchmark model could be conducted.

List of Figures

List of Tables

Nomenclature

A_α	Accumulation terms
A	Cross secional area
b_α	Factor for shrinkage/expansion
c_w^{salt}	Concentration of salt in water
g	Gravitational acceleration constant
h	Hydraulic head
k_r	Relative permeability
k_{ej}	Effective permeability of phase j
k_{rj}	Relative permeability of phase j
$m_\emptyset$	Pore volume multiplier
P_c / P^{cap}	Capillary pressure
P_e	Capillary entry pressure
P_n / p_{nw}	Pressure of the non-wetting fluid
P_w	Pressure of the wetting fluid
q	Volumetric flow rate
q_α	Outflux density component
r_{og} / r_{go}	Oil to gas / gas to oil ratio
r_{eff}	Effective radius of a pore channel
s_n	Non-wetting fluid saturation
s_s	Salt precipitation saturation
s_w	Wetting fluid saturation
s_α	Fluid phase saturation
u_a	Velocity of component α
v	Velocity
V_b	Bulk volume
V_p	Void volume

v_α	Phase fluxes
$\emptyset$	Porosity
$\emptyset_{ref}$	Reference porosity
α	Fluid phase / Fluid component
γ	Interfacial tension (IFT) / A positive exponent
κ	Hydraulic conductivity
λ	Phase mobility / Shape exponent
μ	Viscosity
ρ	Density
ϕ_c	Residual porosity

Abbreviations

BHP	Bottom hole pressure
CCUS	Carbon Capture Utilization and Storage
CO_2	Carbon dioxide
EOR	Enhanced oil recovery
GCS	Geological carbon storage
GHG	Greenhouse gases
IEA	International Energy Agency
IFT	Interfacial tension
IPCC	Intergovernmental Panel on Climate Change
OPM	Open Porous Media
$scCO_2$	Supercritical CO_2
SPE CSP 11	The 11th Society of Petroleum Engineers Comparative Solution Project

Contents

Chapter 1

Introduction

1.1 Motivation

Climate change is a rising concern for the world today. Burning of fossil fuels, transportation, food production and over-consumption are all factors that contribute to release of greenhouse gases (GHG) in the atmosphere, leading to warming of the planet (United Nations, n.d.). The Intergovernmental Panel on Climate Change (IPCC) publishes reports and assesses climate change with scientific basis (Intergovernmental Panel on Climate Change (IPCC), n.d.). According to the IPCC, an increase of 54% of net anthropogenic GHG emissions occurred from 1990 to 2019 (Intergovenmental Panel on Climate Change (IPCC), 2023). In 2015, at the United Nations Climate Change Conference, the Paris Agreement was shaped with the goal to limit global warming to 2° Celsius below pre-industrial temperatures, ideally 1.5 (UNFCCC, n.d.; IEA, 2020). Reaching the goals of the Paris Agreement requires a significant cut in carbon emissions (Huang & Zhai, 2021), and with an increasing demand of electricity, countries must find a way to reduce their power emissions (IEA, 2020). Investment in sustainable energy sources is a must, and the reliance on fossil fuels must come to an end (United Nations, 2022).

According to IEA (International Energy Agency), CCUS (carbon capture, utilization and storage), needs to be an essential component in this shift (IEA, 2021). Various projects, such as enhanced oil recovery (EOR) projects and acid gas projects, has demonstrated the feasibility of storing carbon dioxide (CO_2) underground as a mitigation tool (Benson et al., 2005). It is a technology where captured CO_2 is injected into deep underground geological formations for storage (Fernø et al., 2023). Existing storage projects has proven the low risk of CO_2 leaking back to the surface, as long as storage cites are carefully selected, appraised, and monitored (IEA, 2021). Saline aquifers are examples of possible CO_2 storage formations, which are reservoirs filled with formation water (brine) with high storage capacity (Benson et al., 2005). A challenge when injecting CO_2 into such a reservoir is the potential for precipitation of salt, which occurs when water evaporates, increasing the salinity in the brine until it reaches its solubility limit, where

salt will start to precipitate out of the phase (Norouzi et al., 2021; Miri & Hellevang, 2016).

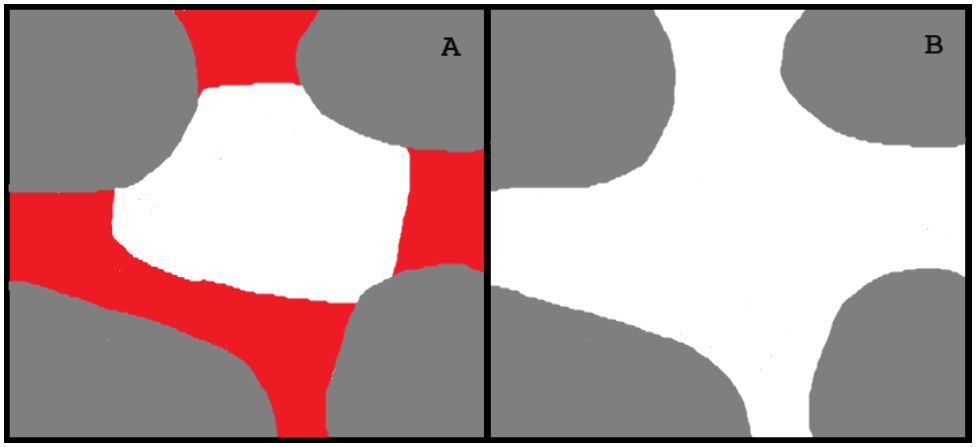

Figure 1.1: Schematic of salt precipitation on the rock surface of a porous medium. A: Formation dry-out where solid salt occupies part of the pore space. B: Pore space filled with 100% solid salt. The red color represents the injected CO_2, the white color represents solid salt, and the grey color represents the rock grains. Figure created with inspiration from Landa-Marbán et al. (2024).

Figure 1.1 illustrates a porous medium where salt has precipitated, which occur on the surface of the rock (Landa-Marbán et al., 2024). Literature has found that salt precipitation can cause an impairment on permeability, and effect porosity and injectivity of a reservoir (Guyant et al., 2015; Zhang et al., 2024; Bacci et al., 2011; Norouzi et al., 2021). Akindipe et al. (2021) concluded that salt precipitation occurs in the near-well region because of drying, caused by evaporation of water, resulting in undesirable consequences on injectivity. Pruess and Muller (2009) describes that heterogeneities can direct the injected CO_2, and thus be an important contributing factor to how salt precipitation and dry-out occur in a medium. This master thesis will investigate the effects of heterogeneity on spatial distribution of salt precipitation, and the subsequent effect on CO_2 injection. The study will contribute to the field of research by performing numerical simulations on models with various permeabilities, to examine where salt precipitates in systems with varying degrees of heterogeneity.

1.2 Objective

The objective of this master thesis is to study the spatial distribution of salt precipitation in systems with different degree of heterogeneity. More specifically, permeability alterations have been performed in two different models to investigate how the degree of heterogeneity contributes to solid salt clogging near an injection well. Understanding how heterogeneity affects the distribution of salt precipitation is important for CO_2 injection processes.

Numerical simulations have been performed using OPM Flow on two different models, where cases with salt precipitation and without salt precipitation have been simulated for comparison on the spatial distribution of CO_2 saturation during and after injection. The first is a 3D model, where results have been plotted with a focus near the injection well. Here, a total of 32 runs have been simulated with varying degrees of heterogeneity. The second model is based on the SPE CSP 11B benchmark grid. Here, permeability has been altered in cells next to the injection well.

Chapter 2

Background and Theory

Storing captured CO_2 in deep permeable and porous sedimentary basins overlaid by an impermeable cap rock falls under the collective term GCS (geological carbon storage) (Fernø et al., 2023). This section will introduce key elements in GCS by presenting potential storage cites, various CO_2 trapping mechanisms and the physics behind fluid flow in porous media. Salt precipitation, capillary backflow and formation dry-out will be explained, and important factors regarding properties of CO_2 and brine will be briefly described at the end of this chapter.

2.1 Geological CO_2 Storage

2.1.1 Performance Factors and Storage Options

There are three performance factors to be considered in the process of selecting a suitable CO_2 storage site: the capacity must be adequate so that all the intended CO_2 can be stored, the injectivity must be adequate to handle the rate of the injection, and the CO_2 must be trapped so it does not leak back into the atmosphere (containment) (Celia et al., 2015; Loizzo et al., 2010). CO_2 storage sites are located more than 1 km deep underground where the CO_2 is trapped permanently (Krevor et al., 2023). Storing CO_2 can be done in a variety of different sedimentary basins including depleted oil and gas reservoirs or saline aquifers (Krevor et al., 2023; Wang, 2013). Depleted oil and gas reservoirs are known to provide adequate containment because of the accumulation of hydrocarbons (Loizzo et al., 2010). An advantage of depleted oil and gas reservoirs is the low pore pressure during injection of CO_2, but a disadvantage is the large amount of wells which can pose an increased risk of leakage (Loizzo et al., 2010). According to Benson et al. (2005), saline aquifers provide the largest volumes of storage. These are reservoirs filled with formation brine, where the concentration of brine increases with depth (from 800-2000 m) (Edem et al., 2022).

2.1.2 Saline Aquifers

According to the IPCC, total capacity for saline aquifers is estimated to be 1000 $GtCO_2$ (Benson et al., 2005). Efficiency is a key factor in storage capacity and can be classified into characteristics of the aquifer (such as pressure, temperature and salinity), aquitard (such as capillary entry pressure), operation (such as number of injection wells), and regulatory constraints (such as maximum bottom-hole pressure) (Bachu, 2015; Celia et al., 2015). In contrast to depleted oil and gas reservoirs, saline aquifers are not known to the same level, and as such, factors including heterogeneity are not well known in these formations (Loizzo et al., 2010), which is the main uncertainty in plume migration prediction (Krevor et al., 2023).

Another negative side of saline aquifers is that evaporation of water into CO_2 can lead to precipitation of salt, which occurs when the evaporation increases the salinity in the brine until it reaches its solubility limit, where salt will start to precipitate out of the phase (Norouzi et al., 2021; Miri & Hellevang, 2016). There is a general agreement in literature, both by numerical simulations and experimental studies, that salt precipitation can cause an impairment on permeability (Guyant et al., 2015; Zhang et al., 2024; Bacci et al., 2011). Prior to precipitation of salt, there is only one solid phase present in the formation (rocks), but as salt precipitates, an additional solid phase (precipitated salt) occurs at the rock surface (Landa-Marbán et al., 2024). As salt precipitates, the absolute permeability of a rock can be reduced, but literature has found that the relative permeability of CO_2 can increase because of the evaporation of the residual water (Miri & Hellevang, 2016; Ott et al., 2015; Roels et al., 2014).

Sedimentary rocks can either be clastic or non-clastic, where clastic sedimentary rocks are a result of weathering and erosion of rocks, whilst non-clastic sedimentary rocks are either made up from precipitated minerals or organic remains (Zolotukhin & Ursin, 2000). Sandstone and shale are examples of clastic rocks, classified by their grain size (Zolotukhin & Ursin, 2000). Hydrocarbon reservoirs are often located in sandstones, and because of the high permeability and porosity of the rock, it is also a good option for storing CO_2 (Kim et al., 2023). Sleipner, located in the North Sea, has injected CO_2 into the saline aquifer Utsira Sand since 1996 (Chadwick et al., 2004). Here, CO_2 is injected into a 200-300 m thick and 800-1000 m deep sandstone (Ringrose, 2020).

If the variation in permeability in a reservoir approaches zero, the formation is homogeneous, and if it reaches one, the formation is very heterogeneous (Wang, 2013). Enhanced capillary trapping may occur as a result of various capillary pressure values in a heterogeneous reservoir (Sun et al., 2023). Additionally, a heterogeneous reservoir may consist of low permeability layers, which can cause the injected CO_2 to migrate horizontally further into the reservoir than in a homogeneous system (Sun et al., 2023). The degree of heterogeneity can be measured by the coefficient of variation (CV), or the Dykstra-Parsons Coefficient (V_K), see Equation 2.1, which is

a method where the standard deviation is divided by the mean permeability (Tiab & Donaldson, 2012).

$$V_K = \frac{s}{\bar{k}} \tag{2.1}$$

Here, s is the standard deviation and $\bar{k}$ is the average permeability, and the standard deviation can be calculated based on Equation 2.2 (Tiab & Donaldson, 2012).

$$s = \sqrt{\frac{\sum_{i=1}^{n}(k_i - \bar{k})^2}{n-1}} \tag{2.2}$$

Here, n is the number of data points and k_i is the permeability (Tiab & Donaldson, 2012). The following values for V_K indicates the degree of heterogeneity: $V_k = 0$ is a homogeneous reservoir, $0 < V_k < 0.25$ is a slightly heterogeneous reservoir, $0.25 < V_k < 0.50$ is a heterogeneous reservoir, $0.50 < V_k < 0.75$ is a very heterogeneous reservoir, $0.75 < V_k < 1.00$ is an extremely heterogeneous reservoir and $V_k = 1$ is a perfect heterogeneous reservoir (Tiab & Donaldson, 2012).

2.1.3 Trapping Mechanisms

There are various trapping mechanisms operating at different time scales and length scales that mitigates leakage of CO_2, the security of which increases with time after injection (Nordbotten & Celia, 2011). CO_2 is mobile and buoyant, so after injection, it migrates upwards in the reservoir until it laterally spreads under a low permeability rock (caprock) (Zhang & Song, 2013; Celia et al., 2015). This trapping mechanism is called structural or stratigraphic, where the caprock acts as a seal, preventing CO_2 from leaking up to the surface (Nordbotten & Celia, 2011). Solubility trapping is where CO_2 dissolves into the brine by mass transfer, leading to an increase in density in which gravity causes the CO_2 to sink towards the bottom of the reservoir (Zhang & Song, 2013). This dissolution also leads to carbonic acid formation which lowers the pH of the brine (Nordbotten & Celia, 2011). Mineralization is a trapping mechanism where CO_2 can permanently be stored as part of the matrix of the formation (Flett et al., 2007). This occurs as the dissolved CO_2 alters the reservoir geochemically which can lead to mineral dissolution and precipitation of new solid minerals (Miri, 2015). This is the most secure way of trapping (Nordbotten & Celia, 2011).

The last trapping mechanism is residual trapping, where CO_2 is left immobile as small clusters in pore spaces of the rocks (Zhang & Song, 2013). After injection, when CO_2 migrates upwards in the reservoir because of density differences, brine starts occupying pore spaces that previously was occupied by CO_2, leaving behind residual trapped CO_2 (Zhang & Song, 2013). This occurs when water has as stronger adhesive force to the rock grains than CO_2, meaning the system is

water wet (Zolotukhin & Ursin, 2000). The wetting fluid will spread on the solid surface, creating a smaller wetting-angle (contact angle) with it than the non-wetting fluid (Zolotukhin & Ursin, 2000). This wetting angle can be measured in the laboratory, where an angle less than $90°\theta$ means the denser fluid is the wetting fluid, whilst an angle more than $90°\theta$ means the less dense fluid is the wetting fluid (Zolotukhin & Ursin, 2000). Residual trapping of CO_2 is an important mechanism, however, residual saturation of brine can lead to difficulties when injecting CO_2 into a reservoir (Nordbotten & Celia, 2011). As CO_2 is injected, the two-phase zone travels away from the well and is lead by a flooding front, leaving behind residual brine trapped in one, or several, of the following ways: as films around the grain, liquid bridges, or pools (Miri & Hellevang, 2016; Miri et al., 2015). Water from the trapped brine will eventually evaporate into the CO_2 when exposed to a flow of $scCO_2$ (supercritical CO_2), increasing the concentration of salt in the brine, which causes a dry-out region to develop (Miri & Hellevang, 2016; Liu et al., 2013).

2.2 Fluid Flow in Porous Media

2.2.1 Flow Equations

Prior to injection of CO_2, only one single fluid phase (brine) is present in the pore spaces of the rocks, however, as CO_2 is injected, the dynamics become more complex and a multi-phase fluid flow must be considered. Henry Darcy performed experiments on a water flow through column of sand (Nordbotten & Celia, 2011), and a low permeability caprock has previously been introduced as one of the CO_2 trapping mechanisms. The permeability of a rock defines how easily a fluid can flow through a mediums interconnected pores, and it is represented in Darcy's Law in Equation 2.3 (Nordbotten & Celia, 2011).

$$q_{Darcy} = \kappa \frac{A(h_2 - h_1)}{l} \tag{2.3}$$

Here, q represents the volumetric flow rate $[L^3T^{-1}]$, where L is denotes as the length of the column and T is denoted as time, k represents the hydraulic conductivity $[LT^{-1}]$, A represents the cross-sectional area of the sand column $[L^2]$, h_1 and h_2 are the hydraulic head differences $[L]$ and l is the length of the column $[L]$ (Nordbotten & Celia, 2011). This equation can be applied when only one fluid is present in the pore space (Nordbotten & Celia, 2011). Permeability is related to the hydraulic conductivity, however, the permeability is dependent only on the porous media, not the fluids, but the hydraulic permeability is a function of both, and the relationship between these variables can be expressed by Equation 2.4 (Nordbotten & Celia, 2011).

$$\kappa = \frac{k\rho g}{\mu} \tag{2.4}$$

Here, k is the permeability [Darcy], ρ is the density of the fluid [ML^{-3}], where M denotes mass, g is the gravity constant [LT^{-2}] and μ is the viscosity of the fluid [$ML^{-1}T^{-1}$]. Permeability is directly related to porosity (ϕ), which is the fraction of the total available void space where a fluid can be stored in a rock, see Equation 2.5 (Nordbotten & Celia, 2011; Zolotukhin & Ursin, 2000).

$$\phi_a = \frac{V_p}{V_b} \tag{2.5}$$

Here, V_p represents the void volume and V_b represent the bulk volume (Zolotukhin & Ursin, 2000). In a multi-phase fluid flow, each of the fluids will occupy some fraction of the pores, and now, their phase saturation (s_a) defines the amount each fluid fills the void volume of the rock (ϕs_a) (Nordbotten & Celia, 2011). Here, a represents the individual fluid phase (in this case gaseous or aqueous). When the pores are 100% saturated the sum of the fluids is equal to 1, see formula 2.6 (Nordbotten & Celia, 2011).

$$s_n + s_w = 1 \tag{2.6}$$

Here, s_n is the non-wetting phase and s_w is the wetting phase. With two fluids present in a porous media, relative permeability must be accounted for. This is a measure relating the absolute permeability to the effective permeability (permeability of each fluid when more than one fluid is present), see formula 2.7 (Zolotukhin & Ursin, 2000).

$$k_{ej} = k_{rj} \cdot k \tag{2.7}$$

Here, k_{ej} is the effective permeability to phase j, k_{rj} is the relative permeability to phase j and k is the absolute permeability. Drainage is the process in which the wetting fluid is displaced by the non-wetting fluid, and in a water-wet system, CO_2 displaces brine when injected into the aquifer at high pressure, forming fluid-fluid interfaces (Nordbotten & Celia, 2011). Conversely, imbibition is the process in which the wetting fluid displaces the non-wetting fluid (Anderson, 1987). The pressure difference between the fluids phases is defined as capillary pressure, see Equation 2.8 (Nordbotten & Celia, 2011).

$$P^{cap} \equiv p_n - p_w \tag{2.8}$$

Here, p_n is the non-wetting fluid pressure and p_w is the wetting fluid pressure. Interfacial tension (IFT) is a property of two contacting immiscible fluids and is one of the parameters capillary pressure depends on (Zolotukhin & Ursin, 2000). Also, capillary pressure is sensitive to micro-scale

heterogeneity because the amount of pressure is dependent on the radius of the pore channels (Zolotukhin & Ursin, 2000). This is represented in Equation 2.9 (Nordbotten & Celia, 2011).

$$(p_n - p_w) = (p^{cap})_{max} = \frac{2\gamma\cos(\theta)}{r_{eff}} \tag{2.9}$$

Here, γ is the IFT, θ is the contact angle and r_{eff} is the effective radius of the pore channel. Capillary pressure is dependent several parameters, including phase saturation (Zolotukhin & Ursin, 2000), and this relationship is illustrated in Figure 2.1. Three flow regions develop as CO_2 is injected into the saline aquifer: one aqueous zone, one two-phase zone and one dry-out zone (Ott et al., 2012; Zeidouni et al., 2009; Norouzi et al., 2021), where injection characteristics control the velocity of the two-phase zone (Miri & Hellevang, 2016). Figure 2.1 illustrate that capillary pressure is very high at low water saturation.

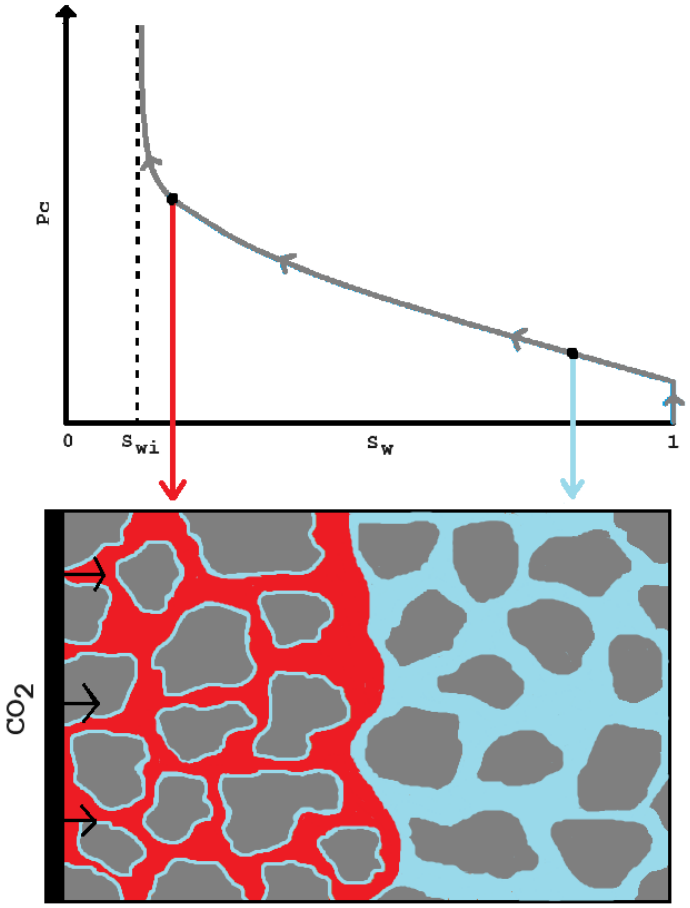

Figure 2.1: Schematic of a capillary pressure curve as CO_2 (red color) is injected into a water-wet system filled with brine (blue color). Here, the horizontal axis on the curve represent the wetting phase saturation (s_w), and the vertical axis on the curve represent capillary pressure (C_p). The injection well is illustrated on the left side of the bottom figure, and the grey color represent the rock grains. The bottom figure was created with inspiration from Miri and Hellevang (2016).

Figure 2.1 illustrate a system where residual brine is left in the pore spaces around the rock grains, and that the curve does not reach zero water saturation as a result of this.

2.2.2 Capillary Backflow and Formation Dry-Out

The dry out front is formed when water evaporates to the point where no brine is left in the pore space of the medium (Liu et al., 2013). Zhang et al. (2024) studied salt precipitation and drying of brine by performing experiments on four microfluidic chips with different wettability and pore structures. One of the conclusions from the authors was that higher saturation of residual brine after gas breakthrough occurred in heterogeneous chips, and they found that hydrophilic chips lead to more salt precipitation near the injection well because of capillary backflow (especially in heterogeneous chips), causing injectivity reduction (Zhang et al., 2024). Capillary backflow is a phenomenon that occurs when the downstream brine is supplied back to the upstream brine (at the evaporation front), which happens because of the rapid evaporation in this area (He et al., 2019).

As previously mentioned, brine can be trapped in several ways, such as films around the rocks (Miri & Hellevang, 2016). This is illustrated in Figure 2.1. Norouzi et al. (2021) found that capillary backflow has the strongest effect near the injection well and is the primary source of salt precipitation in this area, whilst thermodynamics plays the biggest role in salt precipitation further away from the well (Norouzi et al., 2021). Akindipe et al. (2021) found that amount of salt precipitation is greater in smaller pores because of inefficient displacement of brine. They also found that higher injection rates lead to less deposits of salt in the near well regions, and that porosity reductions, correlated to amount of salt deposits, are more significant at lower injection rates. This supports the findings of Yang et al. (2023) which concluded that trapped brine cannot be displaced by gas at a low injection rate, and that diffusion leads to brine evaporation near the inlet where salt will precipitate.

Miri and Hellevang (2016) found three drying regimes which can cause salt to precipitate in various forms: one diffusive regime, one capillary regime and one evaporate regime, and the authors also describe that salt precipitation can occur by salt diffusion and salt self enhancing, in addition to capillary backflow. For example, salt precipitation at the evaporation front can occur because salt is hydrophilic, leading to even more brine being supplied back through the water films, further supporting the evaporation process (Miri et al., 2015; Miri & Hellevang, 2016). Pruess and Muller (2009) concluded that heterogeneity can be a contributing factor to how salt precipitation and dry-out occur in a medium, and found from their study that salt precipitated in the dry-out zone.

2.3 Fluid Properties

When CO_2 is injected into a reservoir for storage, it is typically injected deep enough underground so that it overcomes the critical point of the gas, meaning the CO_2 is in a supercritical state ($scCO_2$), where it has properties of both a gas and a liquid (Nordbotten & Celia, 2011). Gaseous CO_2 is less dense and less viscous than brine, which can result in upwards migration of the CO_2 (gravity override) (Nordbotten et al., 2005). Figure 2.2 illustrates how CO_2 migrates inside the reservoir when injected into a brine filled formation.

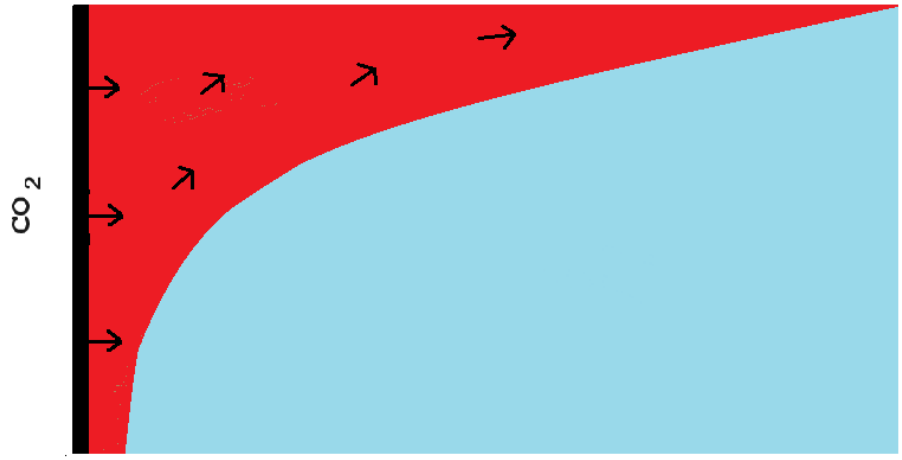

Figure 2.2: Schematic of the upwards migration of CO_2 in a homogeneous reservoir. The black column on the left side of the figure represent the injection well. The arrows indicate how CO_2 migrates upwards and spreads under the cap rock. Created with inspiration from Nordbotten et al. (2005).

The migrating CO_2 is determined by the intrinsic properties of the rock and fluid, i.e. the density, viscosity, permeability and porosity, but also by the fractures and faults distributed in the reservoir (Fernø et al., 2023). As CO_2 is injected, the main driver of the flow is the hydrodynamic (hydraulic head differences from variations in pressures around the injection well) and buoyancy forces, whilst the viscous- and capillary forces work against it (Bachu, 2015). An unfavorable mobility ratio can occur because of the difference in viscosity (Nordbotten et al., 2005). According to Bachu (2015), the mobility ratio (λ) between brine and CO_2 can be calculated by Equation 2.10, where λ_μ represents the phase mobility.

$$\lambda_\alpha = \frac{k_{r\alpha}}{\mu_\alpha} \tag{2.10}$$

Here, $k_{r\alpha}$ is the relative permeability of the phase, and μ_α represent the viscosity of the phase (Bachu, 2015). Properties of the CO_2 will depend on pressure and temperature, whilst properties in brine depend on composition (such as salinity), and an equation of state (EoS) calculates the

density and viscosity values in relation to these dependencies (Nordbotten & Celia, 2011). CO_2 and brine are only slightly miscible, as CO_2 and brine are present simultaneously inside the pore spaces, interphase mass transfer can cause components to change phase, CO_2 can dissolve into the brine, and water can evaporate into the CO_2 (Nordbotten & Celia, 2011).

Chapter 3

Simulation Methods and Approach

This section introduces the concept of reservoir simulation and describes the numerical simulator utilized in this study. Governing equations will be introduced, including models for salt precipitation. A description of the models will be introduced at the end.

3.1 Reservoir Simulation

Parameters dependent on flow change with time in real reservoirs, but in order for a computer to solve the equations of such a system, the reservoir must be divided into a grid where properties are constant within each cell (Pettersen, 2006). An example of a reservoir grid model is illustrated in Figure 3.1, which represents a simplified version of a real reservoir.

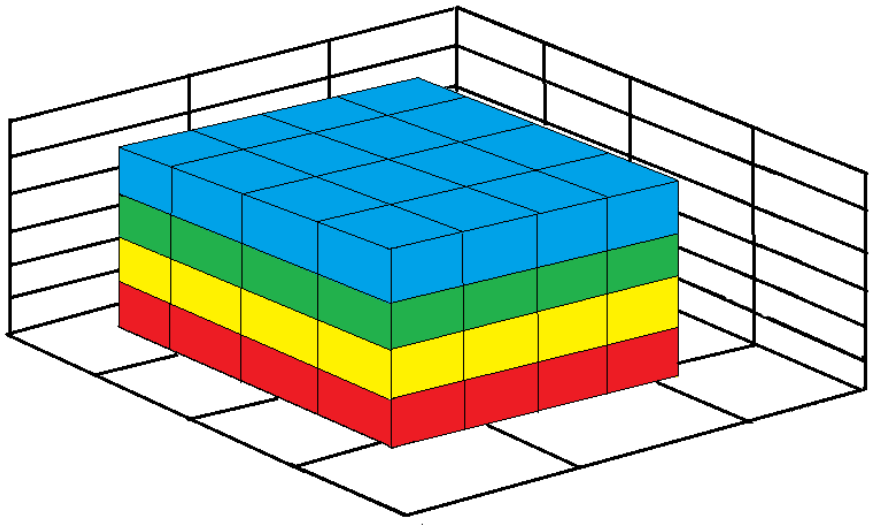

Figure 3.1: Schematic of a Cartesian model. The colors indicate depth, where the blue color represent the top of the reservoir, and the red color represent the bottom of the reservoir.

Modelling of a reservoir is useful in predicting fluid flow behavior, and it involves several steps such as collecting available reservoir data, analyse the data, building geological models, integrating data, and simulation of fluid flow models (Khalili & Ahmadi, 2023). History matching, optimization and and estimation of reserves are other steps involved in the process (Khalili & Ahmadi, 2023). The advantage of reservoir simulation is the ability to discover optimal performance scenarios prior to production in a real life reservoir (Pettersen, 2006). As the flow equations in a real reservoir provides uncertainty, the exact results from a field will not be obtained by such numerical simulations, however, simulated data can after some time be evaluated and compared to production (Pettersen, 2006). There are several steps involved in reservoir simulations, including generation of a grid and numerical modeling where equations for fluid flow are solved (Khalili & Ahmadi, 2023). Petrophysical properties, such as permeability and porosity vary in a real reservoir, and in a reservoir grid such values are defined in each cell (Pettersen, 2006). OPM Flow is the numerical simulator utilized in this study, which will presented in the next section.

3.2 Open Porous Media Simulator

Open Porous Media (OPM) promotes open-source simulation where source-codes for the simulator OPM Flow can be requested on GitHub (Rasmussen et al., 2021). It is a black-oil model where input and output files follow the same structure as the industry standard, and the following phases and components are included: oleic, aqueous and gaseous phases, and water, oil and gas components (Rasmussen et al., 2021).

3.2.1 Governing Equations

The model equations consist of continuous- and discrete equations, where the continuous equations are comprised of partial differential equations formed by the law of conservation of mass (Rasmussen et al., 2021). This section presents the governing equations used by the simulator, and every equation is retrieved from Rasmussen et al. (2021). Equation 3.1 demonstrates the partial differential equations for a component α.

$$\frac{\partial}{\partial t}(\phi_{ref} A_\alpha) + \nabla \cdot u_\alpha + q_\alpha = 0 \tag{3.1}$$

Here, ϕ_{ref} is the reference porosity, A_α is the accumulation terms, u_α is the velocity for component α and q_α is outflux density of component α for a well (Rasmussen et al., 2021). The equation for the accumulation terms, as well as the fluxes, are calculated by OPM Flow using Equation 3.2.

$$A_w = m_\emptyset b_w s_w, u_w = b_w v_w \tag{3.2a}$$

$$A_o = m_\emptyset (b_o s_o + r_{og} b_g s_g), u_o = b_o v_o + r_{og} b_g v_g \tag{3.2b}$$

$$A_g = m_\emptyset (b_g s_g + r_{go} b_o s_o), u_g = b_g v_g + r_{go} b_o v_o \tag{3.2c}$$

Here, A_w, A_o and A_g are the accumulation terms for water, oil and gas, respectively, $m_\emptyset$ is the pore volume multiplier, b_α is the factor for shrinkage or expansion for a phase, s_α is the phase saturation, r_{og} is the oil to gas ratio when oil is vaporized into the gaseous phase, and r_{go} is the gas to oil ratio when gas is dissolved into the oleic phase, v_w, v_o and v_g is the velocity of the water, oil and gas phase, respectively (Rasmussen et al., 2021). v_α is the phase fluxes, demonstrated in Equation 3.3, which is a version of Darcy's Law (Rasmussen et al., 2021).

$$v_\alpha = -\lambda_\alpha K(\nabla p_\alpha - \rho_\alpha g) \tag{3.3}$$

Here, λ_α is the phase mobility, K is the permeability, p_α is the phase pressure, ρ_α is the phase density and g is the vector for the gravitational acceleration (Rasmussen et al., 2021). Equation 3.4 defines the discrete equations of the model, in addition to the residuals, for each cell (i) and pseudo-component α (Rasmussen et al., 2021).

$$R_{\alpha,i} = \frac{\phi_{ref,i} V_i}{\Delta t}(A_{\alpha,i} - A^0_{\alpha,i}) + \Sigma_{j \in C(i)} u_{\alpha,ij} + q_{\alpha,i} = 0 \tag{3.4}$$

Here, the accumulation equations for A_α are previously demonstrated by Equation 3.2, Δt is the length of the timestep, $C_{(i)}$ is the cells connected to cell i, and connection of cells are denoted as ij (Rasmussen et al., 2021). The equations for the fluxes are presented in Equation 3.5 (Rasmussen et al., 2021).

$$u_w = b_w v_w \tag{3.5a}$$

$$u_o = b_o v_o + r_{og} b_g v_g \tag{3.5b}$$

$$u_g = b_g v_g + r_{go} b_o v_o \tag{3.5c}$$

Equation 3.2.1 demonstrates the saturation and capillary pressure equations, which are used for the continuous and discrete equations (Rasmussen et al., 2021):

$$s_w + s_o + s_g = 1 \tag{3.6}$$

$$P_{c,ow} = p_o - p_w \tag{3.7}$$

$$p_{c,og} = p_o - p_g \tag{3.8}$$

Rasmussen et al. (2021) describes that in a system with miscible flow, another variable must be introduced to account for miscibility, denoted as either s_g, r_{go} or r_{og}, to track the phase that has not vaporized or dissolved into another phase. Here, $x = s_g$ indicates presence of all three phases, $x = r_{go}$ indicates the absence of the gaseous phase, and r_{og} indicates the absence of the oleic phase (Rasmussen et al., 2021). Earlier versions of OPM Flow has not allowed for fluids to communicate with the solid rocks surrounding it, however, recent updates of the boundary conditions allow for communication in some aquifers (Rasmussen et al., 2021). There are two well models used in OPM, where the standard well model is the default (Rasmussen et al., 2021).

Current updates allows OPM Flow to run simulations with salt precipitation (Landa-Marbán et al., 2024), where a component for water in gas is added as well as an additional solid phase component (salt) (Baxendale, 2023). The salt precipitation model in OPM constitutes of the following conservation equations, Equation 3.9, Equation 3.10 and Equation 3.11, for salt, water and gas, respectively, and every equation is retrieved from the OPM manual (Baxendale, 2023).

$$\frac{\partial}{\partial t}[\phi b_w s_w c_w^{\text{salt}} + m_\phi \phi_0 s_s \rho^{\text{salt}}] + \nabla \cdot (c_w^{\text{salt}} b_w v_w) + c_w^{\textbf{salt}} q_w = 0 \tag{3.9}$$

$$\frac{\partial}{\partial t}[\phi (b_w s_w + r_{wg} b_g s_g)] + \nabla \cdot (b_w v_w + r_{wg} b_g v_g) + q_w = 0 \tag{3.10}$$

$$\frac{\partial}{\partial t}[\phi (b_g s_g + r_{go} b_o s_o)] + \nabla \cdot (b_g v_g + r_{go} b_o v_o) + q_g = 0 \tag{3.11}$$

Where ϕ is the porosity, b_α is the shrinkage/expansion factor for phase α (calculated as the ratio of the surface volume by the the reservoir volume), s_α is the phase saturation, c_w^{salt} is the concentration of salt in water, m_ϕ is the multiplier of the pore volume, ϕ_0 is the reference porosity, s_s is the salt precipitation saturation, ρ^{salt} is the solid salt density, q_α is the component for out flow of a well, r_{wg} is the water-gas ratio (when water has evaporated into gas) and r_{go} is the gas-oil ratio (when gas has dissolved into the oleic phase) (Baxendale, 2023). The salt conservation equation for oil is not included in this section, however, it can be found in the OPM manual (Baxendale, 2023).The equations account for reduction of porosity and permeability, and Equation 3.12 illustrates the new porosity equation (Baxendale, 2023).

$$\phi = (1 - s_g) m_\phi \phi_0 \tag{3.12}$$

The associated reduction in permeability can be defined by the keyword PERMFACT, which is the permeability multiplication factor, and the relationship between the two properties are illustrated in Equation 3.13 (Baxendale, 2023).

$$\frac{k}{k_0} = (\frac{\phi - \phi_c}{\phi_0 - \phi_c})^{\gamma} \tag{3.13}$$

Where γ is a positive exponent, and when the permeability is zero, ϕ_c is the residual porosity (Baxendale, 2023).

3.2.2 Input File

The keywords OPM uses in the input file are presented in this section. RUNSPEC is the first keyword which defines parameters such as the model dimensions and phases present, followed by the GRID keyword, which defines the geology of the grid (Baxendale, 2023). EDIT is an optional keyword, where properties from the GRID keyword can be edited (Baxendale, 2023). PROPS, REGION and SOLUTION are the next three keywords, where the first describes the fluid phase- and rock properties, the second describes regions and how the properties from the PROPS section are distributed, and the last initializes the model (Baxendale, 2023). SUMMARY and SCHEDULE are the last two keywords, the first being optional and allows for writing of time vector data into output files, and the second defines several parameters including parameters of the well, if wells are open or shut, as well as timse teps and tuning (Baxendale, 2023).

3.2.3 Configuration Files and Visualization

Two open-source frameworks have been utilized in this study, one near well framework (Landa-Merban & von Schultzendorff, 2023) and one SPE CSP 11 framework (Landa-Merban et al., 2023), and configuration files have been used, which set the simulations and create input files (Landa-Marbán et al., 2024). Original files were provided by the first author of the frameworks. Various flags have been utilized in the simulations, to generate 2D plots with a focus near the injection well, and to specify the scale of the plots (Landa-Merban & von Schultzendorff, 2023). In this study, permeability values, thickness and number of layers, and tuning are entries that have been changed from the original provided configuration- and input files. Additionally, in the SPE CSP 11B benchmark case, injection has been changed from cyclic injection to continuous injection, and the years simulated have been increased. Lines have been incorporated in the 2D plots to indicate the separation between layers, and the permeability values are included in figures for clarification. In addition to the plots from the open-source frameworks, the post processing tool ResInsight, which enables visualization i 3D, has be utilized (ResInsight, n.d.).

3.3 Simulation Plan and Model Setup

Two models are utilized in this study to examine the effects of heterogeneity on the spatial distribution of salt precipitation near an injection well. First a layered case will be studied where multiple simulations have been conducted. Then, the SPE CSP 11 benchmark model will be studied with a grid refinement near the well. Both cases are introduced in this section.

3.3.1 Layering Cases

The layered model consist of a 3D cake grid with a total of 32 400 cells, with 81 cells in the z-direction along the injection well. The grid is presented in Figure 3.2, and this figure has been scaled for a better visualization of the model as it is only 40.5 m deep and 10000 m long. The well is located at the corner of the grid, and CO_2 is injected through the entire column for 37 days into the reservoir which is initially filled with brine. The plotted results will have a focus near the injection well as illustrated on the right side of the figure.

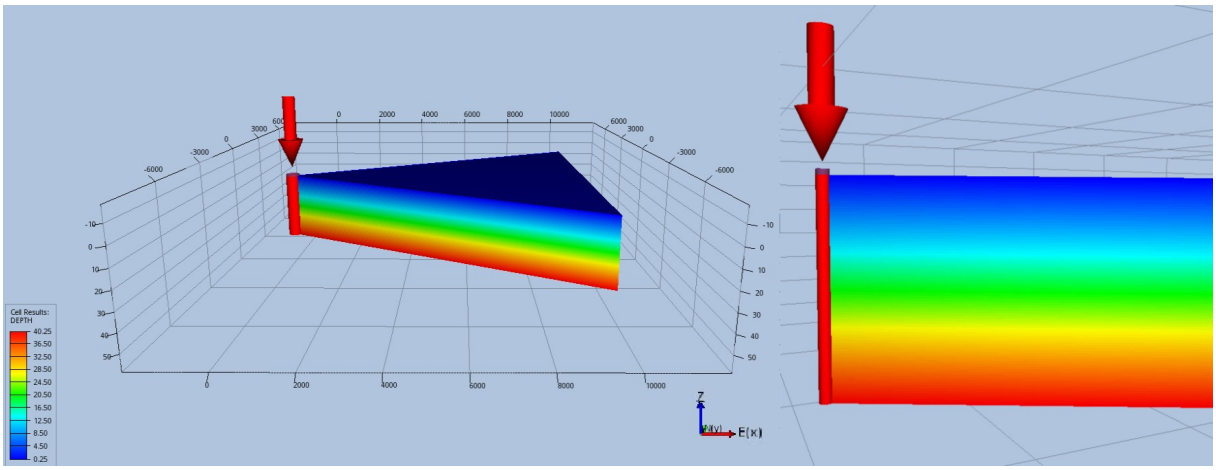

Figure 3.2: Representation of the 3D cake model which is initially filled with brine. The scale represent depth which is 42.5 m, and the length of the model 10000 m. The injection well is represented by the red cylinder and CO_2 is injected through the entire column for 37 days.

This case has been chosen because it is concentrated near a well, and the near-well region is the location where literature has found capillary backflow to be a chief component for precipitation of salt (Norouzi et al., 2021). A total of 32 runs with various orders of layering, number of layers and different permeabilities have been simulated in OPM. Every run has an average permeability of 800 mD. In 16 runs keywords for salt precipitation is included in the input file and for the other 16 runs it is excluded. This provides an opportunity for comparison of the effect of salt precipitation on the spatial distribution of CO_2 saturation. To provide a clear distinction between the runs with and without salt precipitation they will be referred to as sub-runs (*a* and *b*), where *a* is including salt precipitation and *b* is excluding salt precipitation. As an example, when referring

to Run 1, both sub-runs are included. However, if a specific sub-run is discussed, it will be referred to as either Run 1a or Run 1b.

The base case (Run 1) will be introduced and discussed at first. Run 1 consists of three layers with the following permeabilities from top to bottom in the formation: 1500 mD, 750 mD, 150 mD. The next 5 runs (Run 2 - Run 6) consist of three layers with the same three permeabilities as the base case but various orders of layering. Next, a total of 6 runs (Run 7R - Run 12R) use three layers with random generated permeabilities (ranging from 92 mD to 1275 mD) with an average permeability of 800 mD. To add complexity, three runs (Run 13RM - Run 15RM) consisting of 12 layers each with random generated permeabilities have been simulated. Lastly, one homogeneous run (Run 16H) consisting of one layer with 800 mD is included for comparison. Difference in layering and permeability values have been simulated in order to study the effect of permeability on the distribution of salt precipitation. and each run is summarised in Table 3.1.

Table 3.1: Summary of each run, made from different orders of permeability and different number of layers. The following labels are utilized for clear identification of each run: a = including salt precipitation, b = excluding salt precipitation, R = random generated permeabilities, M = many layers, H = homogeneous. The order of permeability values are represented from top to bottom in the formation.

Number of layers	Run number identifier	Permeability [mD]
3	1 (a & b)	1500, 750, 150
	2 (a & b)	1500, 150, 750
	3 (a & b)	750, 1500, 150
	4 (a & b)	750, 150, 1500
	5 (a & b)	150, 1500, 750
	6 (a & b)	150, 750, 1500
	7R (a & b)	947, 801, 652
	8R (a & b)	768, 92, 1091
	9R (a & b)	691, 922, 787
	10R (a & b)	501, 1275, 624
	11R (a & b)	418, 1167, 815
	12R (a & b)	244, 1065, 1091
12	13RM (a & b)	1012, 802, 586
	14RM (a & b)	998, 673, 729
	15RM (a & b)	558, 1404, 438
1	16H (a & b)	800

A near-well GitHub repository has been utilized for the simulations, and the configuration file has been provided by the first author (Landa-Merban & von Schultzendorff, 2023). The base case model consist of three layers with different permeabilities, and properties of the model are presented in Table 3.2. From the provided configuration files, number of layers has been changed to one, three and twelve for the different simulations, see Table 3.1. Additionally, permeability and thickness of layers has been changed. Permeability in the x- and z- directions (PERMX and PERMZ) were changed to be identical within each layer.

Table 3.2: Properties of the model, salt precipitation entries and dimensions of the model. Permeability, numbers- and thickness of the Base Case (Run 1) are included.

Properties of the Model	Value
Reservoir length [m]	10000
Reservoir height [m]	40.5
Number of layers	3
Thickness of each layer [m]	13.5
Rock permeabilities [mD] (top to bottom)	1500, 750, 150
Porosity [%]	20.0
Temperature [$°C$]	60.0
Initial salt solubility limit [kg/m^3]	268
Initial salt concentration [kg/m^3]	138

Two configuration files for this layered case have been provided, one including salt precipitation and one excluding salt precipitation. The configuration files are included in appendix A.1, the input file with salt precipitation is included in appendix B.1 and the input file without salt precipitation is included in appendix C.1. The keywords WATER, GAS, CO2STORE and DISGASW were included in the RUNSPEC section of both input files. These keywords activate various models, the first two activating a water phase and a gas phase, the third keyword activates storage of CO_2, which accounts for solubility of CO_2 and water, and the last keyword specifies the dissolution of gas in water (Baxendale, 2023). The data file with salt precipitation consisted of additional phase keywords in the RUNSPEC section, namely BRINE, PRECSALT and VAPWAT. The first keyword activates tracking of brine, the second keyword activates the salt precipitation model, and the third activates vaporization of water into the gas phase, which can be either dry or wet (Baxendale, 2023). In this input file the keyword SALTSOL was included in the PROPS section, which defines a maximum salt solubility and is activated by the PRECSALT and VAPWAT keyword (Baxendale, 2023). Additionally, the keyword for the initial salt concentration is SALTVD, which was included in the SOLUTION section (Baxendale, 2023). The relative permeability curve and capillary pressure curve for this model are represented in Figure 3.3.

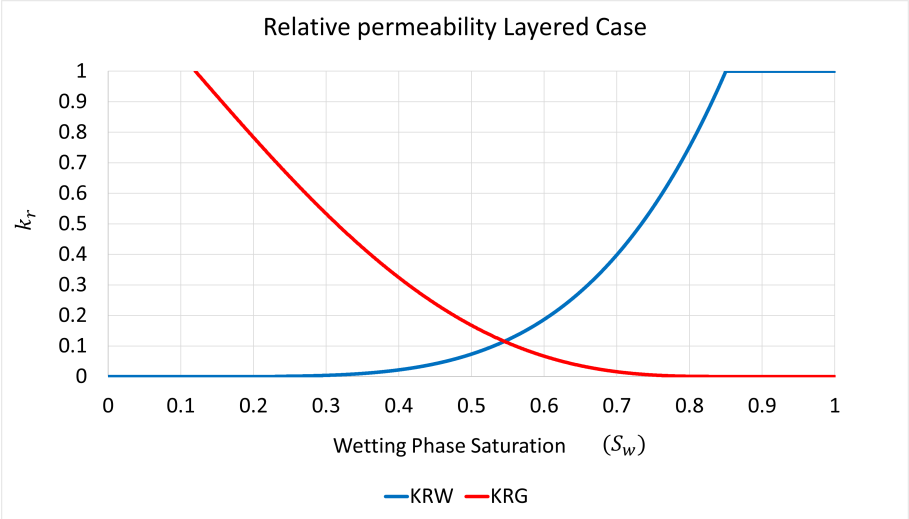

(A)

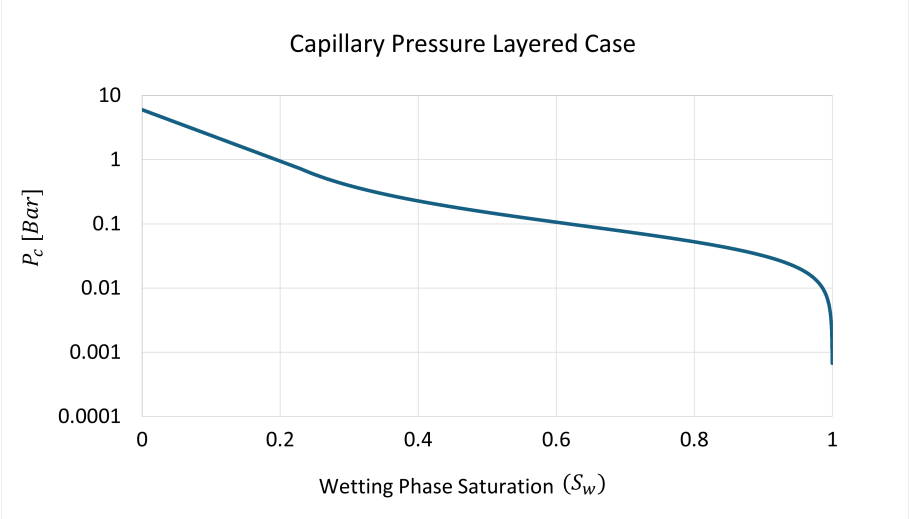

(B)

Figure 3.3: A: Relative permeability curves for the wetting phase (water) and non-wetting phase (gas). B: Capillary pressure curve plotted logarithmically.

Figure 2.1 in section 2.2.1 illustrated a system where residual water saturation was left around the rock grains at high capillary pressure. Figure 3.3B illustrates that $s_w = 0$ at high capillary pressure, which indicates that a dry-out zone has formed, where water has evaporated and there is no brine left in the pore space (Liu et al., 2013).

The following equations were included in the provided configuration file, and to create the input tables, the Brooks-Corey model was adopted (Landa-Marbán et al., 2024; Corey, A. T., 1954). Relative permeability for the wetting phase (water) is represented in Equation 3.14, relative permeability for the non-wetting phase (gas) is represented in Equation 3.15 and capillary pressure is represented in Equation 3.16, and each equation is retrieved from Landa-Marbán et al. (2024). Hysteresis is not activated in the model.

$$k_{rw} = \left(\frac{(s_w - s_{rw})}{(1 - s_{rw} - s_{rg})}\right)^4 \tag{3.14}$$

$$k_{rg} = \left(1 - \left(\frac{(s_w - s_{rw})}{(1 - s_{rw} - s_{rg})}\right)^2\right) \cdot \left(1 - \left(\frac{(s_w - s_{rw})}{(1 - s_{rw} - s_{rg})}\right)^2\right) \tag{3.15}$$

$$p_c = p_e\left(\frac{(s_w - s_{rw})}{(1 - s_{rw})}\right)^{-\frac{1}{\lambda}} - 1\Big)^{\frac{-1}{\lambda}} \tag{3.16}$$

Here, k_{rw} and k_{rg} are the relative permeabilities of water and gas, respectively, S_{rw} is the residual water saturation, S_{rg} is the residual gas saturation, p_c is the capillary pressure, p_e is the entry pressure, λ is a shape exponent (Landa-Marbán et al., 2024).

3.3.2 SPE CSP 11B Benchmark Model

The second model utilized in the study is the 11th Society of Petroleum Engineers Comparative Solution Project (SPE CSP 11) (Society of Petroleum Engineers, 2023). This is a benchmark case developed to provide a platform for development and verification of methods related to geological CO_2 storage simulations (Nordbotten et al., 2024). The benchmark consist of three versions, version A, B and C, which are based on various geometries at different scales (Nordbotten et al., 2024). Version A (laboratory scale) and B (field scale) are 2D models, and version C (field scale) is a 3D model (Nordbotten et al., 2024). This study will utilize version B, where the geometry is based on features of the Norwegian Continental shelf (Nordbotten et al., 2024). Every equation in this section is either retrieved from Nordbotten et al. (2024) or from the provided input- and configuration files. This case has been utilized to investigate the effects of salt precipitation in a more realistic and complex model, and the grid model is illustrated in Figure 3.4.

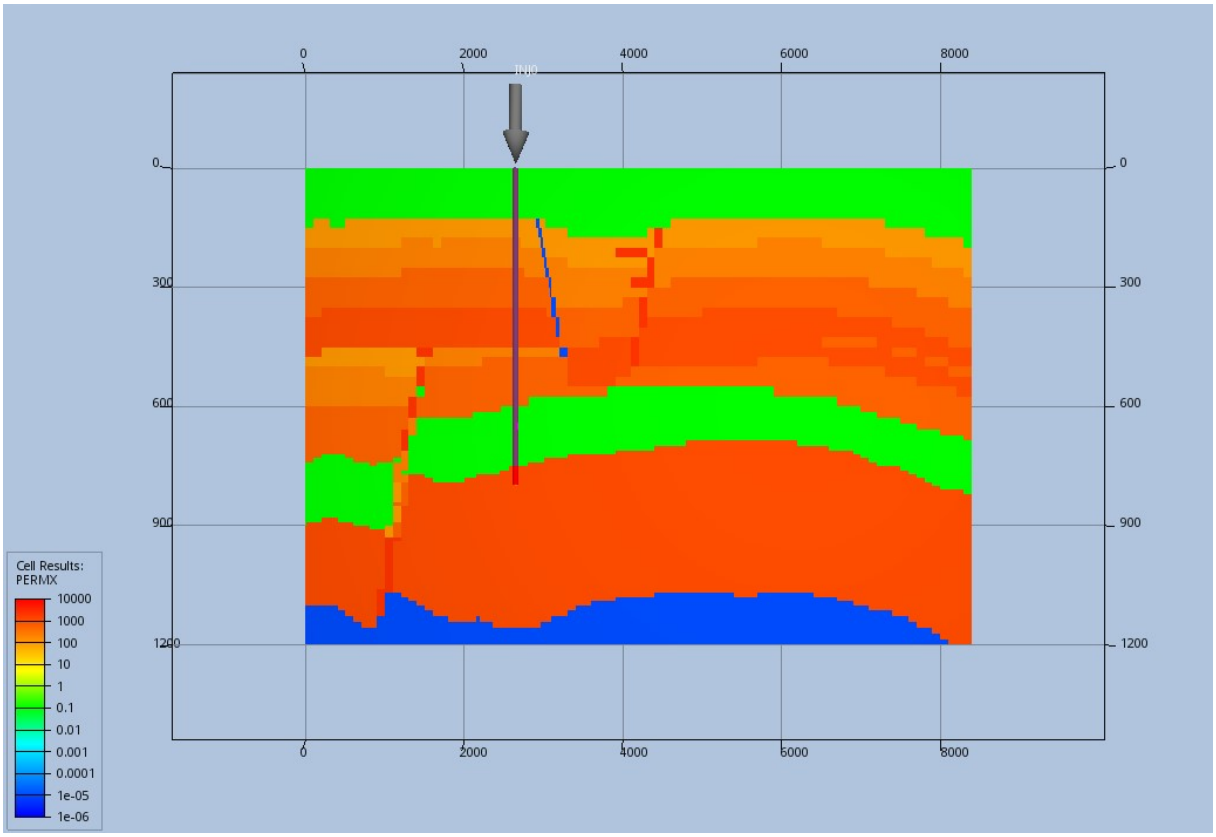

Figure 3.4: Representation of the SPE CSP 11B benchmark grid, obtained by the provided configuration file. The injection well is indicated by the grey line on the figure, and the colors represent permeability in the x-direciton (PERMX).

The color scale in the figures indicate the permeability of the reservoir. For this case the configuration file was simulated to generate the input files, and the input files were simulated directly via flow (not via a command line, as was the case for the layered model). Every configuration file and input file was provided by the first author of the utilized frameworks (Landa-Merban et al., 2023). The configuration file included refined grid cells around the well, in addition to the keyword EQUALS, which allow for arrays, such as permeability, to be specified with a constant (Baxendale, 2023). The SPE CSP 11B benchmark model consist of two wells, where well 1 continuously injects CO_2 for 50 years, and well 2 starts injection at year 25 (Nordbotten et al., 2024). In this study, however, well 2 is not accounted for as only the 25 first years have been simulated. The geology in the SPE CSP 11B benchmark consist of seven facies, with different pemerabilities and porosities in each facie (Nordbotten et al., 2024). The rock- and fluid properties, as well as the dimensions of the model are illustrated in Table 3.3. The values in the table are retrieved from the provided configuration file and input files and from Nordbotten et al. (2024).

Table 3.3: Properties and Dimensions and Salt Precipitation Entries of the SPE CSP 11b Model. Permeability and porosity are included for each facie.

Properties of the Model	Value
Length [m]	8400
Width [m]	1.00
Depth [m]	1200
Permeability 1 [mD]	0.10132
Permeability 2 [mD]	101.324
Permeability 3 [mD]	202.650
Permeability 4 [mD]	506.625
Permeability 5 [mD]	1013.25
Permeability 6 [mD]	2026.50
Permeability 7 [mD]	$1.00 \cdot 10^{-5}$
Porosity 1 [%]	10.0
Porosity 2 [%]	20.0
Porosity 3 [%]	20.0
Porosity 4 [%]	20.0
Porosity 5 [%]	25.0
Porosity 6 [%]	35.0
Porosity 7 [%]	$1.00 \cdot 10^{5}$
Salt solubility limit [$kgsm^3$]	268
Initial salt concentration [kg/m^3]	138

The facies are included in Figure 3.5, and the information on the locations of the facies are retrieved from Nordbotten et al. (2024). In this model, changes were only made to the input file, not the configuration file, where permeability of two grid cells were changed to 100 mD and 1500 mD. Figure 3.4 illustrates the grid refinements around the well, and the two cells with adjusted permeabilities are illustrated by the black frame. The changes in permeability provided identical permeability average for these two cells as for the runs in the layered case (800 mD). The configuration file is provided in appendix A.2, the data file with salt precipitation is included in appendix B.2 and the data file without salt precipitation is included in appendix C.2 .

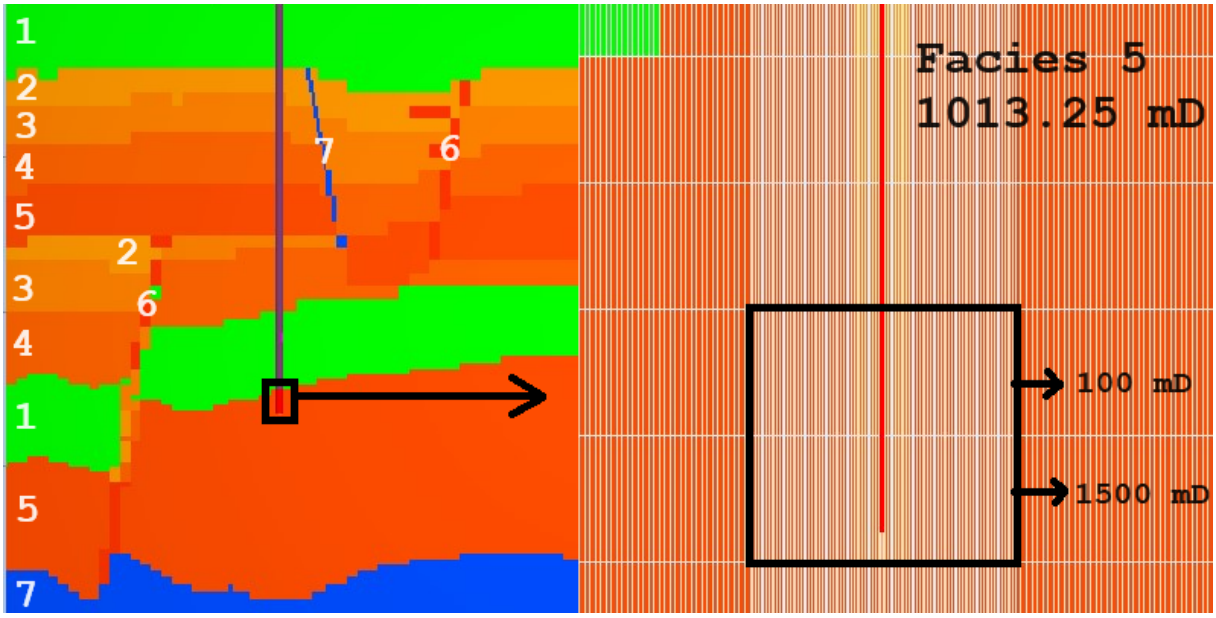

Figure 3.5: Representation of the location of the two cells with adjusted permeability, as well as the location of the seven different facies in the benchmark grid. The cells are located at the bottom of the injection well, where the top cell was changed to 100 mD and the bottom cell was changed to 1500 mD.

From the provided configuration file, the permeability value in two cells under the EQUALS keyword has been changed for this study. Additionally the following keywords have been changed: WCONINJE has been changed from a cyclic injection to a continuous injection, TSTEPS has been changed from four years to 25 and three years, and TUNING has been adjusted. One case including salt precipitation has been simulated over 25 years, and one case excluding salt precipitation was simulated over three years. The reason as to why the case without salt precipitation was simulated over a much shorter time period, was because of computational problems when running this case in OPM Flow. It was, however, not expected that the case without salt precipitation would be more difficult for the computer to run than the case with salt precipitation. To achieve similar number of outputs for comparison between the two cases, the case including salt precipitation was simulated one additional time over three years with adjusted time steps. Salt precipitation only occurred in two cells over three years, however, in the 25 year case, it occurred in one additional cell (the cell located above the two cells with adjusted permeabilities, see Figure 3.5). The relative permeability curve and the capillary pressure curve are illustrated in Figure 3.6.

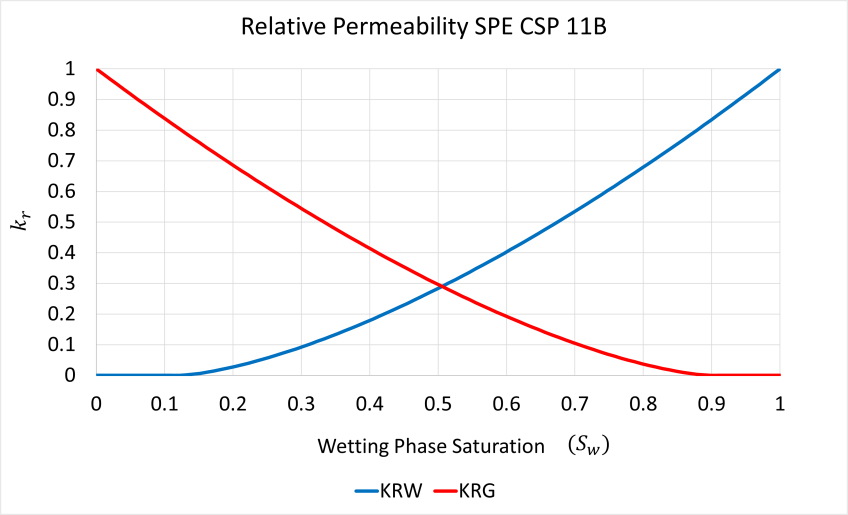

(A)

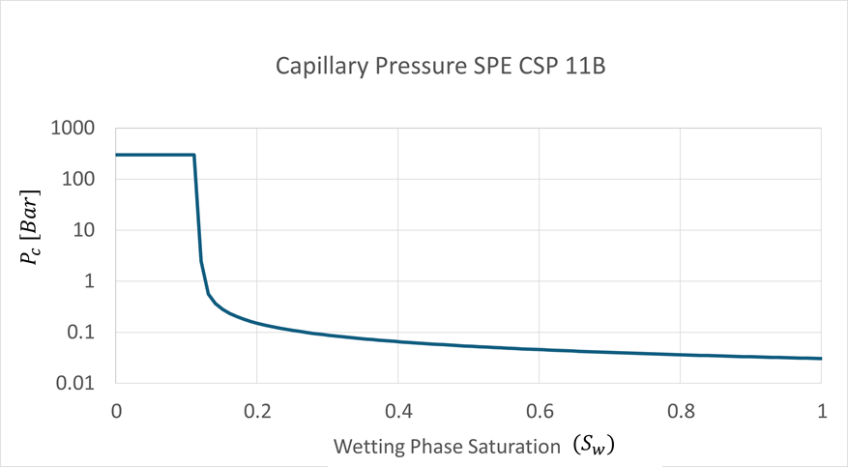

(B)

Figure 3.6: A: Relative permeability curves for the wetting phase and the non-wetting phase. B: Capillary pressure curve plotted logarithmically.

Figure 3.6A represents relative permeability for the wetting phase, and Figure 3.6B represents capillary pressure in the model.

Equation 3.17 and Equation 3.18 illustrates the phase saturations for the wetting phase and the non-wetting phase, respectively, which are utilized in the benchmark model (Nordbotten et al., 2024).

$$s_{w,n} = max(\frac{s_w - s_{w,imm}}{1 - s_{w,imm}}, 0) \tag{3.17}$$

$$s_{n,n} = max(\frac{s_n - s_{n,imm}}{1 - s_{n,imm}}, 0) \tag{3.18}$$

Nordbotten et al. (2024) utilizes the Brooks-Corey saturation and relative permeability relationship, see Equation 3.19.

$$k_{r,\alpha}(s_\alpha) = (s_{\alpha,n})^{c_{\alpha,1}} \tag{3.19}$$

Where the nonlinearity of relative permeability is determined by the exponent $c_{\alpha,1}$, and based on the Levrett-J scaling, the capillary entry pressure has been defined for the SPE CSP 11B, see Equation 3.20 (Nordbotten et al., 2024; Abdoulghafour et al., 2020).

$$P_{entry} = \sqrt{\frac{\phi}{k_x}} \cdot 6.12 \times 10^{-3} N/m \tag{3.20}$$

The injection wells do not transfer heat after injection, and the right and left boundaries consist of insulated boundary conditions (Nordbotten et al., 2024).

Chapter 4

Results and Discussion

This chapter presents the numerical simulations, which examines the impact of salt precipitation on spatial distribution of CO_2 saturation after injection into brine-saturated heterogeneous and homogeneous reservoirs. Three main sections are included. The first presents the results from the layered cases, consisting of an introduction and discussion of the base case, followed by the three and 12 layered cases. The second main section presents the results from the SPE CSP 11B benchmark study. Here, two runs has been simulated: one case over 25 years and one case over three years. Salt precipitation is studied and compared with CO_2 saturation development. The third main section will include a comparison of all cases.

4.1 Layered Case

As described in chapter 3, this model consists of a 3D cake grid where CO_2 is injected into a saline aquifer for 37 days. Sub-runs are referred to with the identifier *a* or *b*, where the former represents runs including salt precipitation and the latter represents runs excluding salt precipitation. Separating lines have been incorporated in illustrative figures, which will be in 2D with a focus near the injection well, to clarify where the borders between each layer are.

4.1.1 Base Case

The base case will be referred to as Run 1. It consists of three layers with the following permeabilities descending from top to bottom in the reservoir, 1500 mD, 750 mD and 150 mD. Figure 4.1 comprises three plots illustrating the spatial distribution of non-wetting (CO_2) saturation and salt precipitation after injection for Run 1. Figure 4.1 (top) illustrates distribution of CO_2 saturation excluding salt precipitation (Run 1b), Figure 4.1 (middle) illustrates distribution of CO_2 saturation including salt precipitation (Run 1a) and Figure 4.1 (bottom) illustrates distribution of precipitated salt in Run 1a.

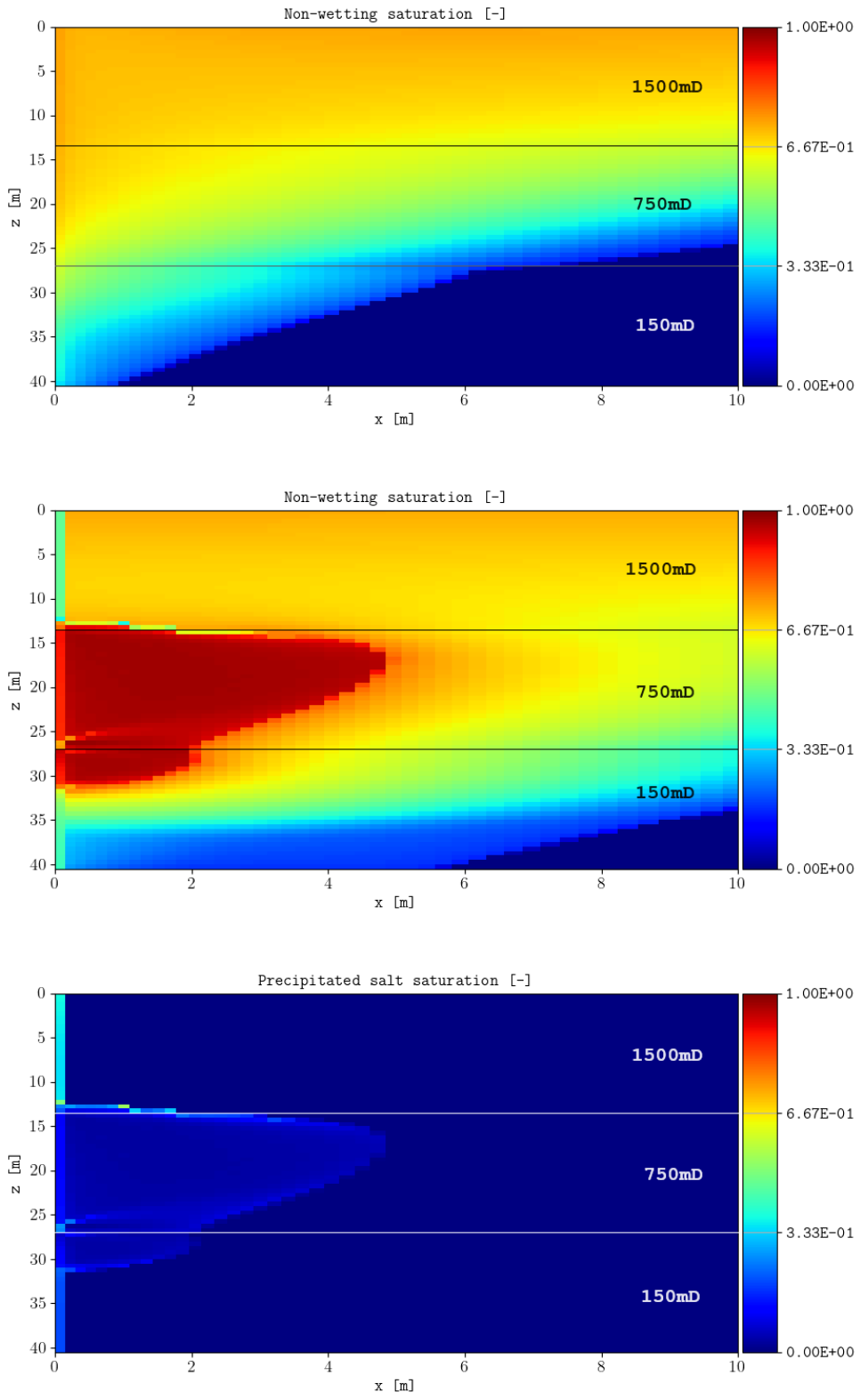

Figure 4.1: Plots of the spatial distribution of non-wetting (CO_2) saturation and salt precipitation after injection. Top: Spatial distribution of CO_2 saturation excluding salt precipitation (Run 1b). Middle: Spatial distribution of CO_2 saturation including salt precipitation (Run 1a). Bottom: Salt precipitation distribution (Run 1a). Note that the color scale in the top and middle figures represent the fraction of CO_2 saturation in the pore space of each cell, but for the bottom figure it represents the fraction of precipitated salt in the pore space of each cell. The vertical axes represent meters along the well and the horizontal axes represent meters away from the well.

The three layers in the formation are separated by differences in permeability, as indicated by the separating lines in the figure. The scale in Figure 4.1 (top) and Figure 4.1 (middle) represent the fraction of CO_2 saturation in the pore space of each cell, where a value of zero means no CO_2 is present in the pores and a value of one means 100% of the pore space is saturated with CO_2. As presented in chapter 2.2.1, three flow regions develop as CO_2 is injected into a saline aquifer, namely an aqueous region, a two-phase region and a dry-out zone (Ott et al., 2012; Zeidouni et al., 2009; Norouzi et al., 2021). Two of these flow regions can be observed in Figure 4.1 (top) in Run 1b, namely a two-phase region and an aqueous region. From the scale it is evident that the area with the highest CO_2 saturation is located predominantly in the top layer with a downwards gradient to the middle and bottom layer. The aqueous region is located mainly in the bottom layer. The upward migration of CO_2 is expected because of the differences in densities between the CO_2 and brine (Nordbotten et al., 2005). In addition to these gravity effects, the order of permeability decreases with depth, which could contribute to the ease of upwards vertical fluid flow.

Figure 4.1 (middle) represent CO_2 saturation in Run 1a. Here, the third region can be observed, namely the dry-out zone. The dry-out zone, as described in chapter 2.2.2, is where water has evaporated to the point where no brine is left in the pore spaces, only dry CO_2 (Liu et al., 2013). It is apparent from the figure that this zone is plume-shaped and mostly located in the middle layer, however, some dry-out has also occurred in the bottom layer. Between the border of the top- and middle layer, along the edge of the dry-out zone, some cells contain less CO_2 saturation. This could be because of capillary backflow, as explained in chapter 2.2.2. There is also less CO_2 saturation in the cells next to the well, specifically in the top and bottom layer. This could indicate that capillary backflow has occurred in these areas as well. Literature has found capillary backflow to occur in near well regions (Norouzi et al., 2021), which supports these assumptions. The dry-out zone, in addition to the areas with low CO_2 saturation next to the well, illustrate a clear distinction between the two sub-runs when salt precipitation is included versus when it is excluded.

Figure 4.1 (bottom) represents the distribution of salt precipitation for Run 1a after CO_2 injection. Contrary to the scales in the CO_2 saturation figures, the scale in this figure represents the fraction of precipitated salt in the pore space of each cell. To clarify, if this value is zero it means no solid salt occupies any of the pore space of a cell, and if the value is one, it means 100% of the pores in the cell is occupied by solid salt. It can be observed from Figure 4.1 (bottom) that salt precipitated along the well and in the dry-out zone. There is also an accumulation of salt precipitation in some cells along the border between the top and middle layer. The reason for the solid salt accumulation in these cells could be because of capillary backflow to the 750 mD layer where most of the dry-out zone is located. This assumption agrees with the findings of Peysson et al. (2014), which concluded from their experimental studies that capillary flows induced by drying can lead to transport of dissolved salt and pore clogging.

Furthermore, Miri and Hellevang (2016) explains that capillary backflow can contribute to salt precipitation, which again supports the assumption that this mechanism has occurred in these areas. Salt has precipitated in the dry-out area, which was expected based on literature (Miri & Hellevang, 2016; Liu et al., 2013). The impact of permeability on the distribution of salt precipitation during CO_2 injection can be further inspected by examining the development of salt precipitation and CO_2 saturation in each layer as a function of time. Figure 4.2 illustrates development of salt precipitation (smooth lines) and CO_2 saturation (dashed lines), from start until end of injection, for one cell in each layer.

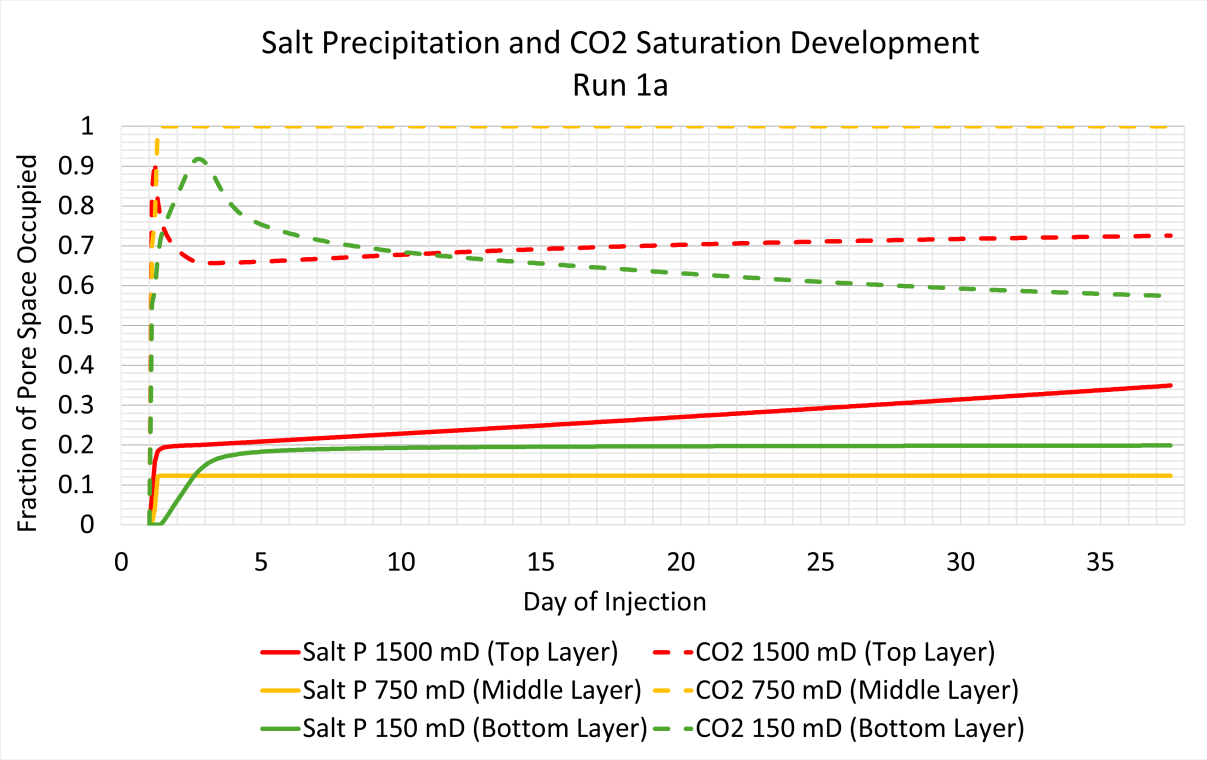

Figure 4.2: Salt precipitation and CO_2 saturation development in the pore space of three cells as a function of time. The first cell is located at the top layer (1500 mD), the second cell is located in the middle layer (750 mD), and the third cell is located at the bottom layer (150 mD). The colors illustrate permeability: red represents the highest permeability, yellow represents the medium permeability and green represents the lowest permeability. The solid lines represent salt precipitation (Salt P) and the dashed lines represent CO_2 saturation.

The first cell is located in the top layer (1500 mD) at 6.25 m depth from top to bottom of the injection well. The second cell is located in the middle layer (750 mD) at 20.8 m and the third cell is located in the bottom layer (150 mD) at 33.8 m. These locations were used because they are located approximately in the middle of each layer, and it provided an opportunity to compare how the spatial distribution of salt precipitation affected injection of CO_2 in areas with different permeability. In the top layer cell, 91.5% of the pore space was saturated with CO_2 on day one of injection. From the figure it is evident that the cell was subject to a blockage of solid salt that same time of the day where 16.4% salt precipitated. Then, the CO_2 saturation in the cell rapidly

decreased to 65.7% at day three of injection. The CO_2 saturation in the middle layer cell (750 mD) reaches a maximum value of one the first day, which indicates complete dry-out as no brine is left in the pore space (Liu et al., 2013). Salt precipitates in the cell over the first day until a value of 12.3% is reached, at which point it stays constant. The bottom layer comprises the lowest permeability value in the medium (150 mD). It can be observed that this cell reaches its highest CO_2 saturation during day two of injection, which is 91.5%. Salt precipitation occurs later in the 150 mD cell compared to the two cells in the higher permeability layers. This cell reaches its highest value of precipitated salt, which is 19.9%, on the last day of injection.

Figure 4.2 illustrates that the highest permeability cell was subject to the highest fraction of precipitated salt during injection, and that CO_2 saturation decreased after this. This indicates a solid salt clogging, which has the potential to affect the permeability of the cell. This assumption is supported by Peysson et al. (2014), which concluded from their core experiments that pores can be clogged when dissolved salt accumulates near the surface of injection, which can alter permeability. This rapid decrease of CO_2 saturation in the top layer cell (1500mD) could have occurred because of the high permeability in the layer providing capillary backflow of brine. This will be investigated further by comparison the other runs with varying heterogeneity in the next sections.

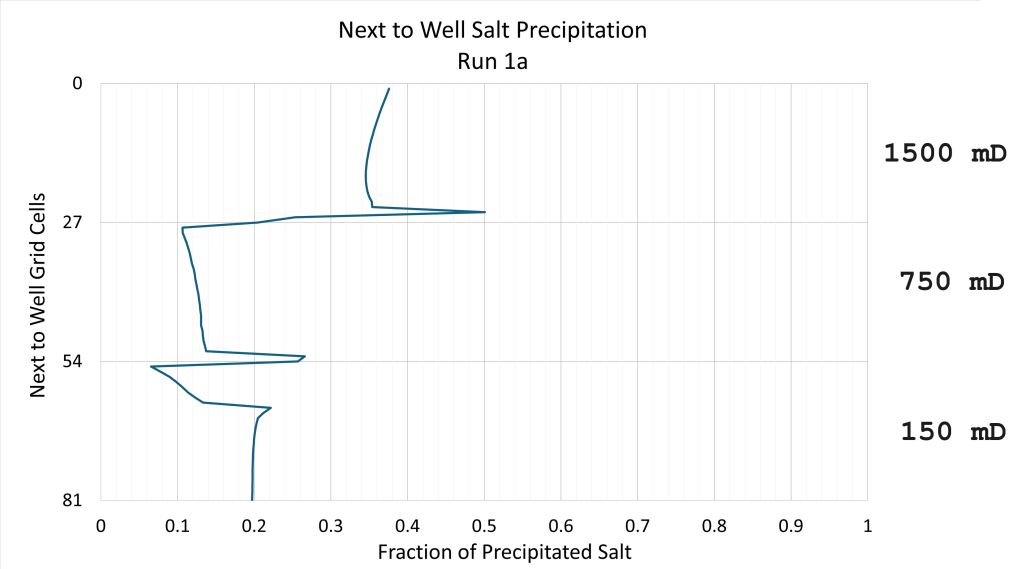

Figure 4.3: Graphical representation of the amount of precipitated salt in each cell next to the injection well. The 81 cells are represented on the vertical axis, and the horizontal axis represent fraction of precipitated salt in the pore space of each cell. The three layers in the medium, each consisting of 27 cells, are indicated by separating lines and their associated permeabilities are included for clarification.

Figure 4.3 illustrates the total fraction of solid salt at the end of injection, in the pore spaces of every cell located next to the well. This figure further illustrates that the 1500 mD layer contains the highest amount of precipitated salt compared to the other two layers. This indicates clogging of the cells next to the well, which can change permeability and porosity (Peysson et al., 2014). Between the borders of the layers, specifically the top and middle layer, a spike of solid salt can be observed. This further indicates that capillary backflow has occurred in the cells next to the well in the high permeability layer, and thus caused higher fractions of salt precipitation in this area. Berntsen et al. (2019) explains that capillary backflow of brine plays an essential role in wellbore clogging induced by salt precipitation, which aligns with these assumptions. The 750 mD layer contains less solid salt in most of its cells next to the well than the other two layers. The reason for the low fractions of precipitated salt could be because the dry-out zone is located in this layer, as discussed previously, see Figure 4.1 (bottom). Figure 4.4 illustrates the development in the cell containing the highest fraction of salt precipitation in the entire formation.

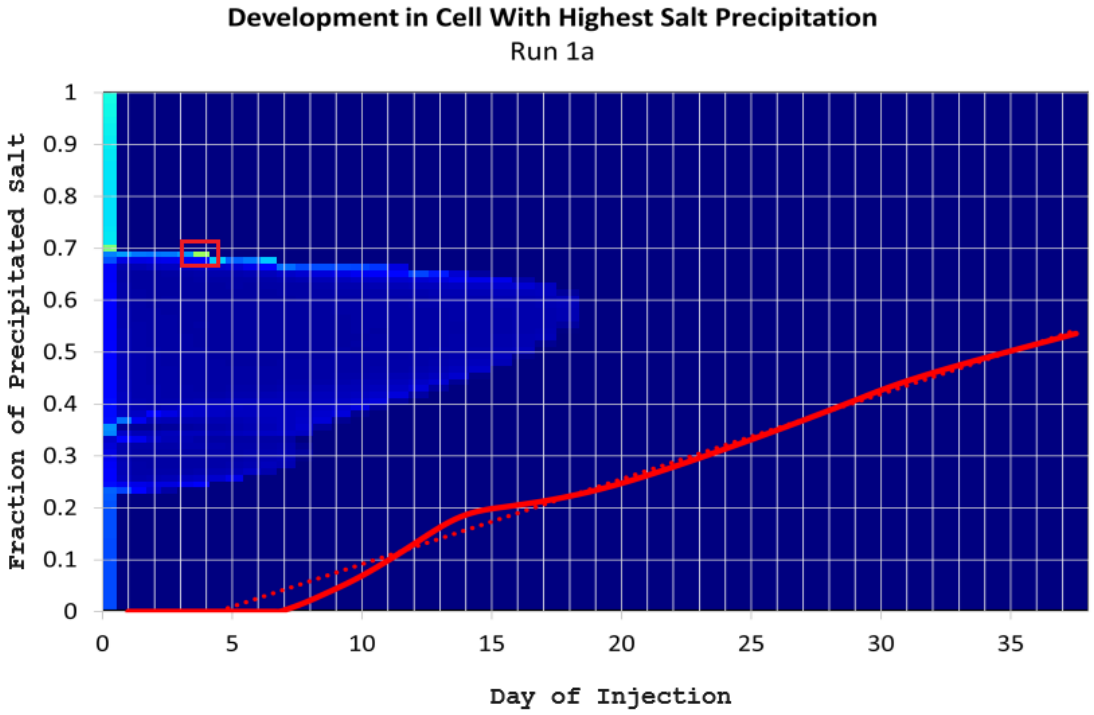

Figure 4.4: Schematic of salt precipitation development in the one cell containing the highest fraction of precipitated salt at the end of injection as a function of time. The cell is highlighted with a red frame in the background. The vertical axis represent the fraction of precipitated salt, the horizontal axis represent day of injection and the dotted line is the treadline.

It is apparent from Figure 4.4 that salt does not precipitate in this cell until day 7 of injection. From here, salt precipitation occurs until it reaches a value of 18.6% solid salt in the pore spaces at day 14, before it levels off for a few days. This was not expected, and could be because of an artifact in the numerical simulations. Preceding day 15 a new steady increase occurs until the pore space is occupied by 53.6% solid salt on the last day of injection. Capillary backflow seems

to occur mostly from the high permeability layer, backflow of brine being one of the mechanisms that can cause salt to precipitate (Miri & Hellevang, 2016).

Bottom hole pressure (BHP) was studied to provide an indication on the injectivity. Figure 4.5 displays a higher BHP when salt precipitation is included (Run 1a) versus when it is excluded (Run 1b). This could be because of salt precipitation next to the well in Run 1a, where the highest fraction of precipitated salt was found to be located in the top layer cells. During day one of injection, the BHP in Run 1a rises to its highest pressure value which is 217.9 bar, and the average pressure during the 37 days of injection is 217.6 bar. Run 1b reaches its highest BHP during day 37 of injection, which is 216.3 bar. The average pressure difference between the runs is 1.39 bar.

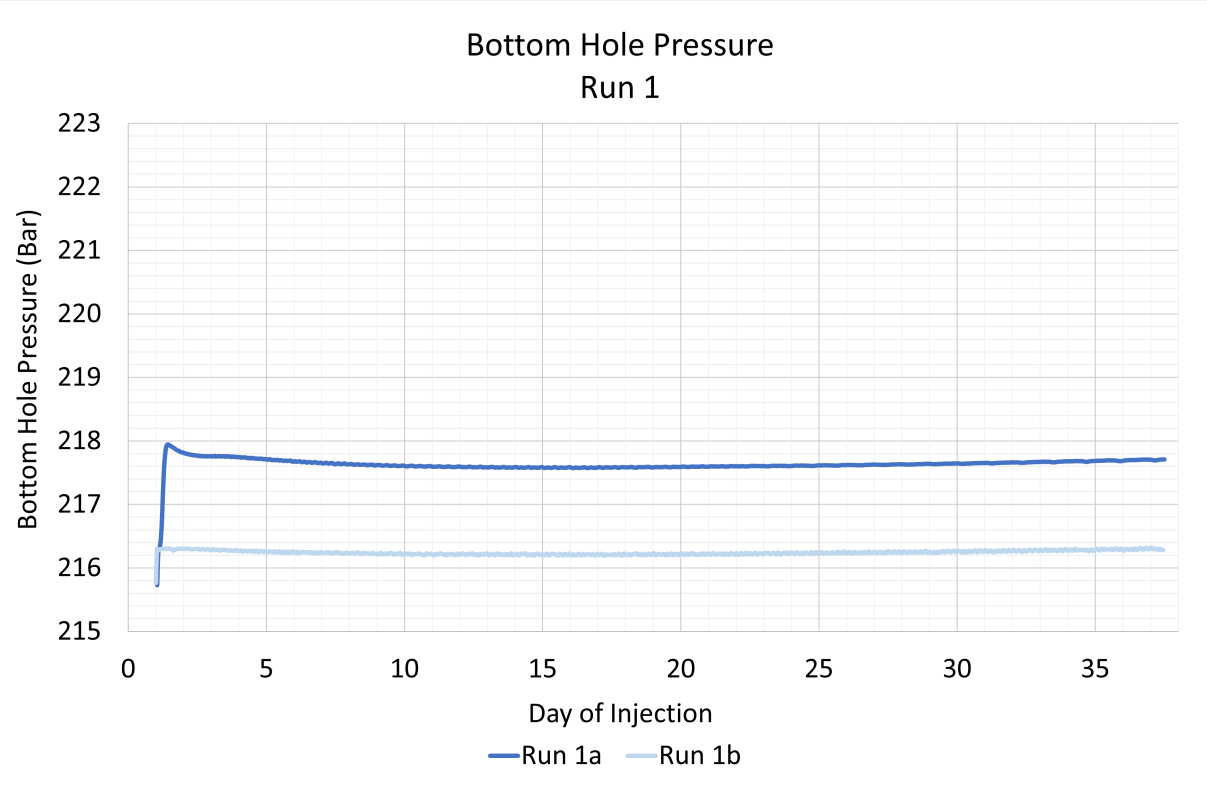

Figure 4.5: Bottom hole pressure during injection for Run 1. Run 1a (including salt precipitation) is represented by the dark blue color and Run 1b (excluding salt precipitation) is represented by the light blue color. The vertical axis represent BHP and the horizontal axis represent day of injection.

4.1.2 Summary of All Runs

A total of 32 runs have been simulated by performing permeability alterations, as well as change in number of layers, to analyze the effect of heterogeneity on salt precipitation and CO_2 saturation near the injection well. Identifiers *a* and *b* continue to be referred to as the cases including and excluding salt precipitation, respectively. Run 2 to Run 6 consists of three layers each with the same permeabilities to the base case, arranged in various orders in the medium. Run 7R to Run 12R consist of three layers with random generated permeabilities, which will be referred to with the identifier *R*, indicating that they are random. The next three runs (Run 13RM - Run 15RM) consist of 12 layers with random generated permeability. The identifier *M* is included to indicate that they consist of many layers. Lastly, one homogeneous run (Run 16H) is included for comparison. Here, the identifier *H* for homogeneous is included. The permeabilities in each run are summarised in Table 4.1 together with their standard deviation and the Dykstra-Parsons Coefficient (V_K), see Equation 2.1 and Equation 2.2, to indicate the degree of heterogeneity (Tiab & Donaldson, 2012).

Table 4.1: Summary of the runs, where the following labels are utilized for clear identification: a = including salt precipitation, b = excluding salt precipitation, R = random generated permeabilities, M = many layers. The order of permeabilities are represented from top to bottom in the formation. Standard deviation and Dykstra-Parsons Coefficient (V_K) are calculated to indicate the degree of heterogeneity in each run. Run 16H is not included in the table. This run is homogeneous and has a permeability of 800 mD.

Run number identifier	Permeability [mD]	Standard Deviation	V_k
1 (a & b)	1500, 750, 150	552	0.69
2 (a & b)	1500, 150, 750	552	0.69
3 (a & b)	750, 1500, 150	552	0.69
4 (a & b)	750, 150, 1500	552	0.69
5 (a & b)	150, 1500, 750	552	0.69
6 (a & b)	150, 750, 1500	552	0.69
7R (a & b)	947, 801, 652	120	0.15
8R (a & b)	768, 92, 1091	416	0.52
9R (a & b)	691, 922, 787	94.8	0.12
10R (a & b)	501, 1275, 624	340	0.43
11R (a & b)	418, 1167, 815	306	0.38
12R (a & b)	244, 1065, 1091	393	0.49
13RM (a & b)	1012, 802, 586	174	0.22
14RM (a & b)	998, 673, 729	142	0.18
15RM (a & b)	558, 1404, 438	430	0.54

The table illustrate that Run 1 - Run 6, as well as Run 8R and Run 15RM are very heterogeneous runs, Run 10R - Run 12R are heterogeneous, and Run 7R, Run 9R, Run 13RM and Run 14RM are slightly heterogeneous (Tiab & Donaldson, 2012). Run 9R has the lowest Dykstra-Parsons coefficient of all runs.

4.1.3 Three Layered Runs With Base Case Permeabilities

This section will present and discuss Run 2 to Run 6, which consist of three layers with the following permeabilities arranged in various orders in the formation: 1500 mD, 750 mD and 150 mD. Run 1a was previously found to have the highest fraction of salt precipitation in the 1500 mD layer next to the well. Salt had also precipitated in the dry-out zone, as was expected based on literature (Miri & Hellevang, 2016; Liu et al., 2013). Figure 4.6 illustrate total cells with salt precipitation for Run 1a - Run 6a. The horizontal axis represents total cells with salt precipitation and data points are included on the lines for legibility. The vertical axis represents the run number (Run 1 - Run 6).

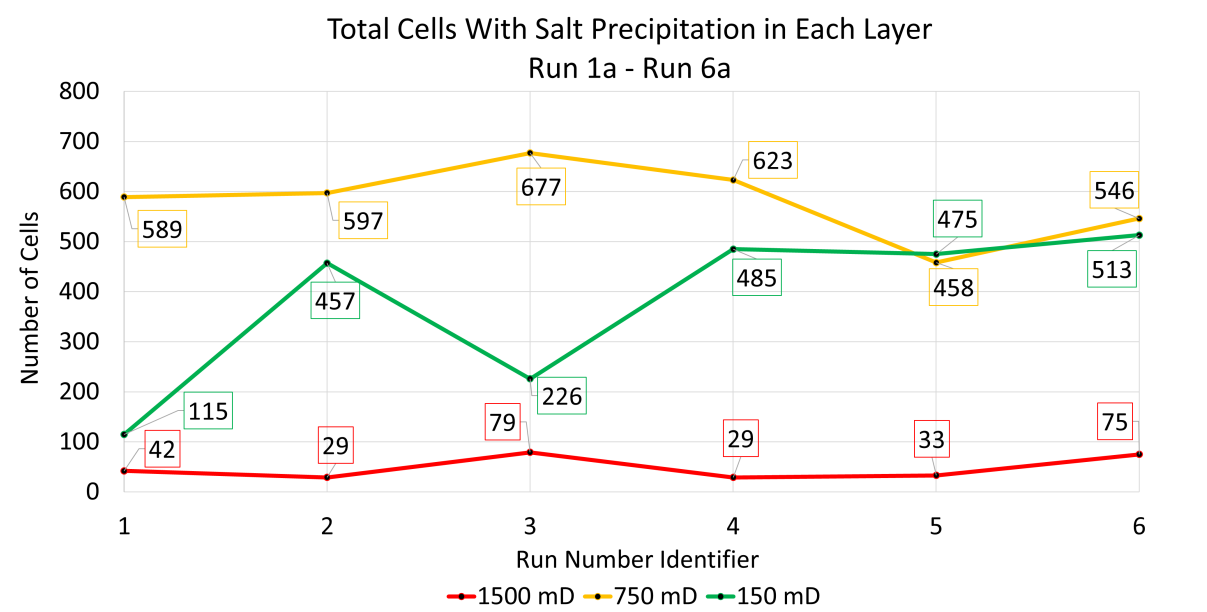

Figure 4.6: Line plot illustrating number of grid cells occupied by any fraction of solid salt for Run 1a to Run 6a. The horizontal axis represents run number, and the vertical axis represents number of grid cells in each run containing solid salt. The data points highlighted in the plot illustrate total grid cells. The colors illustrate permeability value: red represents the highest permeability, yellow represents the medium permeability and green represents the low permeability.

From Figure 4.6 it is evident that the 1500 mD layer contain the lowest number of total cells with salt precipitation in each run. This means that most of the salt has precipitated in the other two layers, where the dry-out zone is located. The average number of total cells with salt precipitation in the 1500 mD layers are 47.8 cells. The 750 mD layers contains on average 582 number of total cells, whilst the 150 mD layer display more variation depending on its location in the system.

The average number of cells with salt precipitation in this layer is 379 cells. Run 1a and Run 3a display relatively similar curves in the figure, and the same for Run 2a and Run 4a. In Run 5a and Run 6a the 150 mD layer and the 750 mD layer display a similar amount of total cells with solid salt. It can be observed that the common denominator for Run 1 and 3 is that the 150 mD layer is located at the bottom in the formation, for Run 2 and 4 it is located in the middle of the formation and in Run 5 and 6 is that the 150 mD layer.

In Run 3a the 1500 mD layer is located in the middle and the 150 mD layer at the bottom. This means there is a large ratio between the middle and lower layer. In comparison, for Run 1a where the 750 mD layer is located in the middle and the 150 mD layer is located at the bottom, the permeability ratio is smaller. A local accumulation of solid salt can be observed in the cell next to the well between the middle and bottom layer (at 26.75 m) in Run 3a, see Figure 4.7. This cell reaches a value of 99.9% solid salt. This could be because as CO_2 was injected, salt precipitated rapidly in the 1500 mD layer because of capillary backflow. This indicates solid salt clogging in these cells. Ott et al. (2010) observed local salt accumulation as a result of capillary backflow of brine, which agrees with these assumptions. As the bottom layer (150 mD) has the lowest permeability, it is more difficult for the CO_2 to permeate from it through the pores into the middle layer, which could have lead to a higher fraction of salt precipitation along this border. It would be easier for the CO_2 to flow into the top layer because of the higher permeability in addition to the gravity effects.

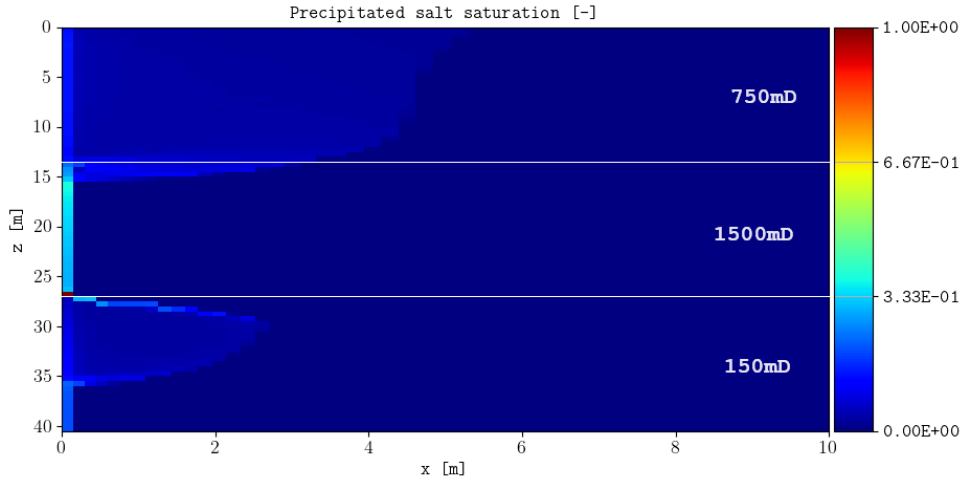

Figure 4.7: Schematic of salt precipitation distribution for Run 3a after CO_2 injection. The scale illustrates the fraction of solid salt in each cell. The vertical axis represents depth along the injection well and the horizontal axis represents meters away from the well. The run consist of three layers and their associated permeability are included for clarification.

Dispersion of solid salt for Run 2a and Run 4a after injection of CO_2 is illustrated in figure 4.8. The top layer (1500 mD) in Run 2a contains the highest fraction of precipitated salt, and capillary backflow has seemingly occurred in this area. This indicates clogging near the injection well. This assumption is in agreement with literature, as Miri and Hellevang (2016) describes that the backflow mechanism can cause salt to precipitate. The permeability ratio between the top and middle layers is significantly large, and a high fraction of local solid salt accumulation can be observed along the permeability border in two cells. This indicates clogging of solid salt in these cells as well. These observations also agrees with Ott et al. (2010) which observed local salt accumulation as a result of capillary backflow of brine. The cells with the highest fraction of precipitated salt at the end of injection reached 99.9% solid salt.

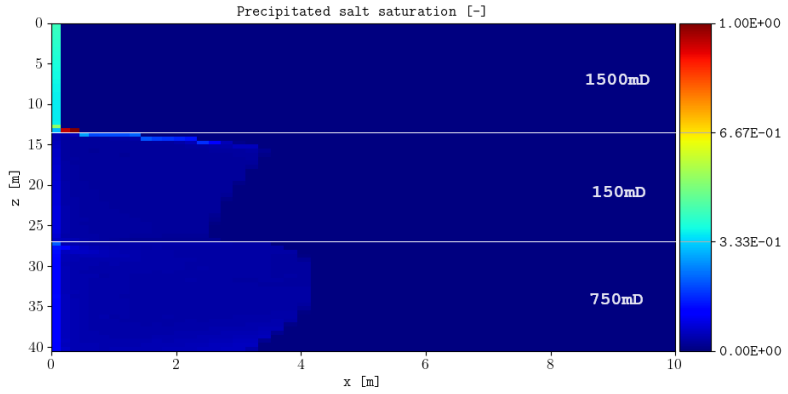

(A)

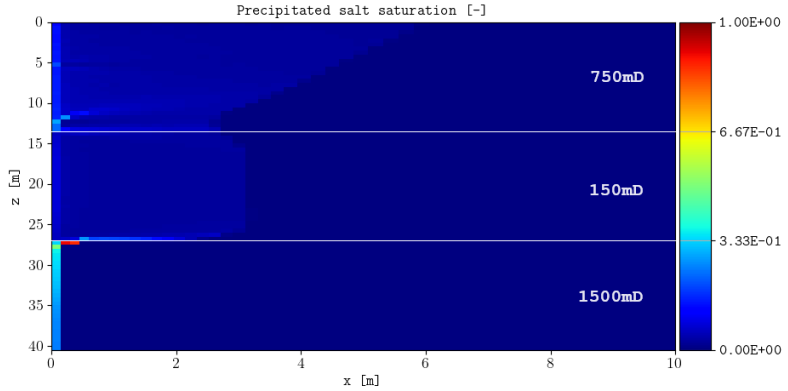

(B)

Figure 4.8: Plot of salt precipitation distribution after CO_2 injection for Run 2a and Run 4a. A: Run 2a, B: Run 4a. The scale illustrates the fraction of solid salt in each cell. The vertical axes represent depth along the injection well and the horizontal axes represent meters away from the well. The runs consist of three layers and their associated permeability are included for clarification.

In Run 4a the 1500 mD layer is located at the bottom, and capillary backflow has supplied brine upwards to the layers above. From the figure it is evident that this run also has two cells along

the border of the bottom and middle layer, filled high fractions of solid salt, where the highest fraction was found to be 90.5%. In Run 3a, only one cell along the border of the 1500 mD and 150 mD layer consisted of such a high fraction of solid salt. The reason could be because in Run 3, capillary backflow had two ways in which it could flow, either up to the layer above or down to the layer beneath, as the 1500 mD layer was located in middle of the formation. In Run 2a and Run 4a the blocked high permeability layer is located at the top and bottom, meaning the back flow of brine was forced to flow into the adjacent layer, thus causing higher fractions of solid salt in these cells. This means that, based on these results, the location of the high permeability layer are of significance in regards to the solid salt accumulation along borders between layers. Spatial distribution of salt precipitation after injection for Run 5a and Run 6a is illustrated in figure 4.9.

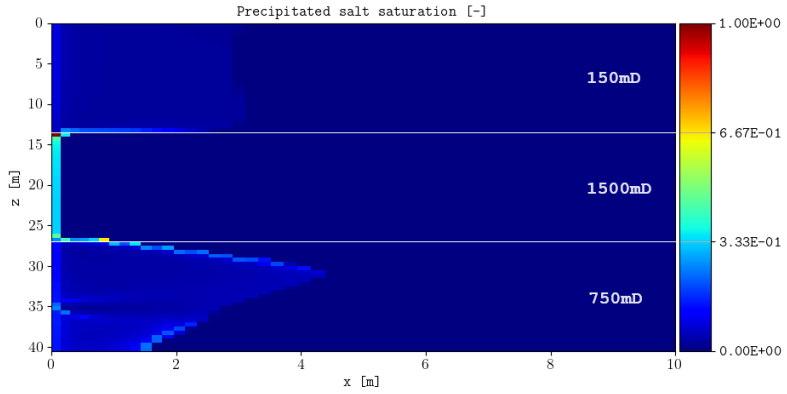

(A)

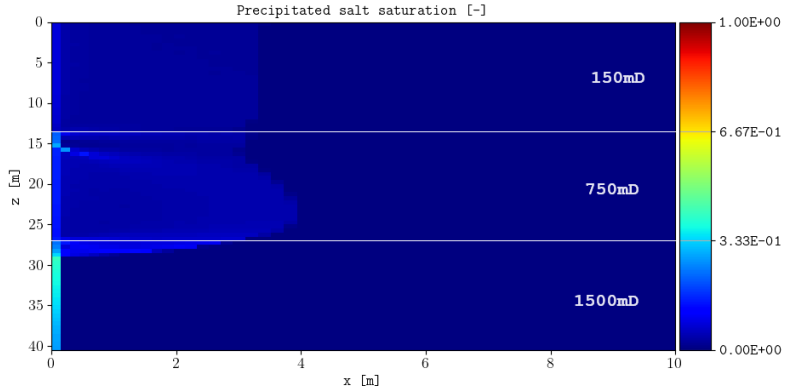

(B)

Figure 4.9: Plot of the spatial distribution of salt precipitation after CO_2 injection for Run 5a and Run 6a. A: Run 5a, B: Run 6a. The scale illustrates the fraction of solid salt in each cell. The vertical axes represent depth along the injection well and the horizontal axes represent meters away from the well. The runs consist of three layers and their associated permeability are included for clarification.

Run 5a and Run 6a display a similar number of total cells with any fraction of salt precipitation in their 150 mD and 750 mD layers, as seen in figure 4.6. Run 5a is the only run that has a larger number of cells with precipitated salt in the low permeability layer (150 mD) than in its other two layers. In Run 5a, equal to Run 3a, the 1500 mD layer is located in the middle of the formation, however, the 750 mD layer is located at the bottom and the 150 mD layer at the top. Run 3a and Run 5a display similar numbers of total cells with precipitated salt, as previously mentioned. Run 3a displayed a local accumulation of precipitated salt in the cell between the border of the bottom (150 mD) and middle (1500 mD) layer.

Run 5a displays such an accumulation at the border of the 150 mD and 1500 mD layer, and at the border of the 1500 mD layer and the 750 mD layer. From Figure 4.9 it is evident that the cell with the highest fraction of precipitated salt in Run 5, however, is located where the permeability ratio is the most significant. This cell is filled with total of 99.9% solid salt at the end of injection. In Run 6a there are no cells with such an accumulation of local precipitated salt in any cells, similar to Run 1a. In these runs there were no large permeability ratios between any layers, which could be a potential reason for this. From the results so far it has been observed that the permeability has contributed to the location and intensity of salt precipitation near the injection well. This will be further explored by examining the fraction of salt precipitation in each cell next to the well.

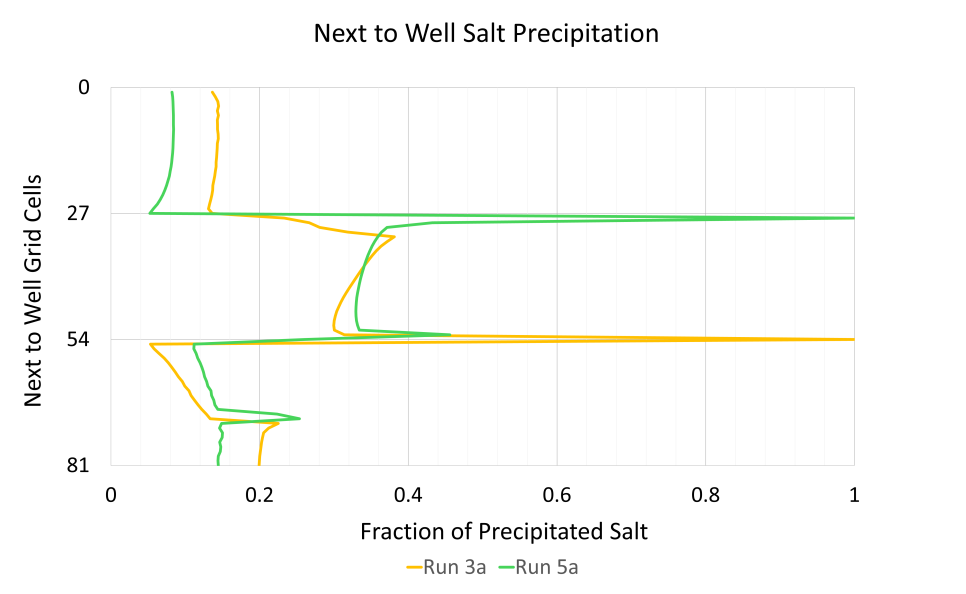

Figure 4.10: Graphical representation of the amount of precipitated salt in each cell next to the injection well for Run 3a (yellow) and Run 5a (green). The 81 cells are represented on the vertical axis, and the horizontal axis represents total fraction of precipitated salt in the pore space of each cell. The three layers, each consisting of 27 cells, are indicated by separating lines.

Figure 4.10 represents the total fraction of precipitated salt in each cell next to the well for Run 3a and Run 5a, both of which have their 1500 mD layer located in the middle of the formation. Both runs display a spike between the 1500 mD and 150 mD layer, where cells reach considerably higher values of solid salt. Run 3a reaches the highest value at a depth of 26.75 m in cell 54 (from top), where 99.97% of the pore space is filled with solid salt. Run 3a reaches the highest value at a depth of 13.75 m where 99.99% of the pore space is filled with solid salt. Run 1a did not display such large spikes of salt precipitation. The maximum value of solid salt filled in the pore space for this run was 0.5245% at a depth of 12.75 m, in cell 26. Run 2a, Run 4a and Run 6a did not display such high spikes between layers. A common factor for these runs is that they do not have the high permeability layer located in the middle.

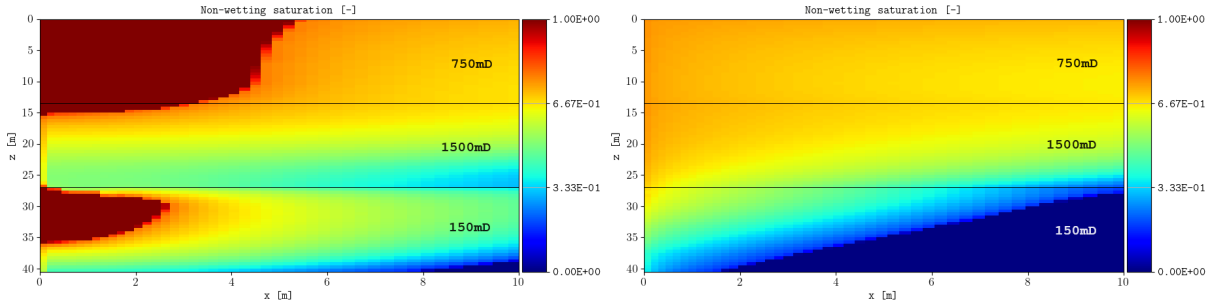

(A) Run 3a

(B) Run 3b

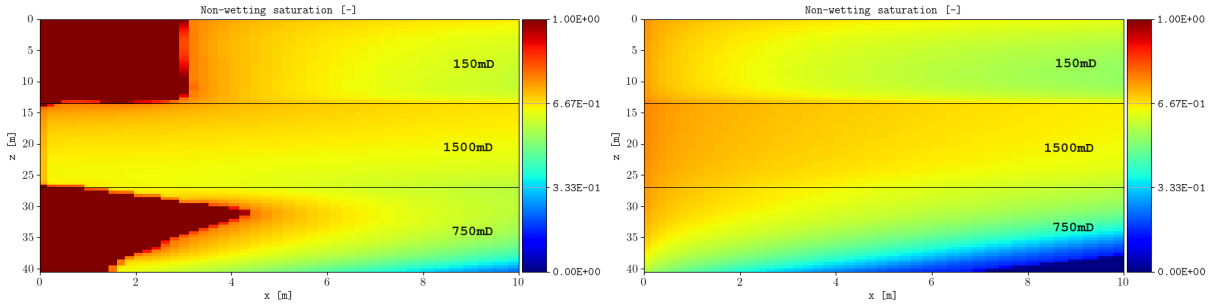

(C) Run 5a

(D) Run 5b

Figure 4.11: Schematic of the spatial distribution of CO_2 saturation after injection for Run 3 and Run 5. A: Run 3a (including salt precipitation), B: Run 3b (excluding salt precipitation), C: Run 5a (including salt precipitation), D: Run 5b (excluding salt precipitation). The vertical axis represents depth along the well and the horizontal axis represents meters away from the well. The three layers in each run are indicated by separating lines and their associated permeabilities are included for clarification. The scale represents the fraction of CO_2 in the pore space of each cell.

Figure 4.11 illustrates the spatial distribution of CO_2 after injection for Run 3a and Run 5a. Both runs have their high permeability layer located in the middle and display similar areas with dry-out. In Run 3a most of the two-phase region containing the highest fraction of CO_2 is located at the top layer where the permeability is 1500 mD. Most of the dry-out is located in this layer as well, as expected because of capillary backflow and salt precipitation next to the well in this layer, as discussed previously. An observation is that the dry-out zone is larger in the bottom

layer (750 mD) in Run 5a than in the bottom layer (150 mD) in Run 3a. This could be because in Run 5a capillary backflow has supplied additional brine to this layer because of the higher permeability. The figures illustrate that the solid salt next to the well in the 1500 mD layer has prevented injection of CO_2, when comparing them to the runs without salt precipitation.

The dry-out zones contribute to a significant difference in distribution of CO_2 when salt precipitation is included versus when it is excluded. In Run 3b, the highest fraction of CO_2 saturation in the two-phase zone is located in the top layer of the formation, with a downwards saturation gradient. In Run 5b, the top layer consists of the lowest permeability, and the highest fraction of CO_2 saturation in the two-phase zone is located in the middle layer with the highest permeability. Sun et al. (2023) explains that low permeability layers can contribute to horizontal migration of the CO_2, and this migration can be observed in Figure 4.11C and Figure 4.11D. This means that CO_2 has migrated as expected in Run 3b and Run 5b, horizontally into the formation, with permeability and gravity effects controlling the flow (Sun et al., 2023; Nordbotten et al., 2005). In Run 3a and Run 5a, similar areas with high fraction of CO_2 in the two-phase region can be observed, however, the dry-out zone contains a larger saturation gradient at the plume front, which was expected based on literature (Peysson et al., 2014; Miri & Hellevang, 2016).

The saturation profiles for Run 2, Run 4 and Run 6 are presented in figure 4.12. In Run 2a the high permeability layer is located at the top of the formation. Because of the solid salt blockage near the well, there is less CO_2 saturation in the top layer of this run than it is in the top layer of Run 2b. The dry-out zone is located in the middle and bottom layers of Run 2a, and a higher saturation of CO_2 in these areas than in Run 2b can be observed, see Figure 4.12A and Figure 4.12B. In Run 4a and Run 6a the high permeability layer is located at the bottom, and the dry-out zones have occurred in the middle and top layers. As the cells in the bottom layers next to the well are clogged with solid salt, but the gravity effects causes CO_2 migrate upwards, the difference in spatial distribution of CO_2 saturation between Run 4a and Run 4b, and between Run 6a and Run 6b, is less significant than between Run 2a and Run 2b.

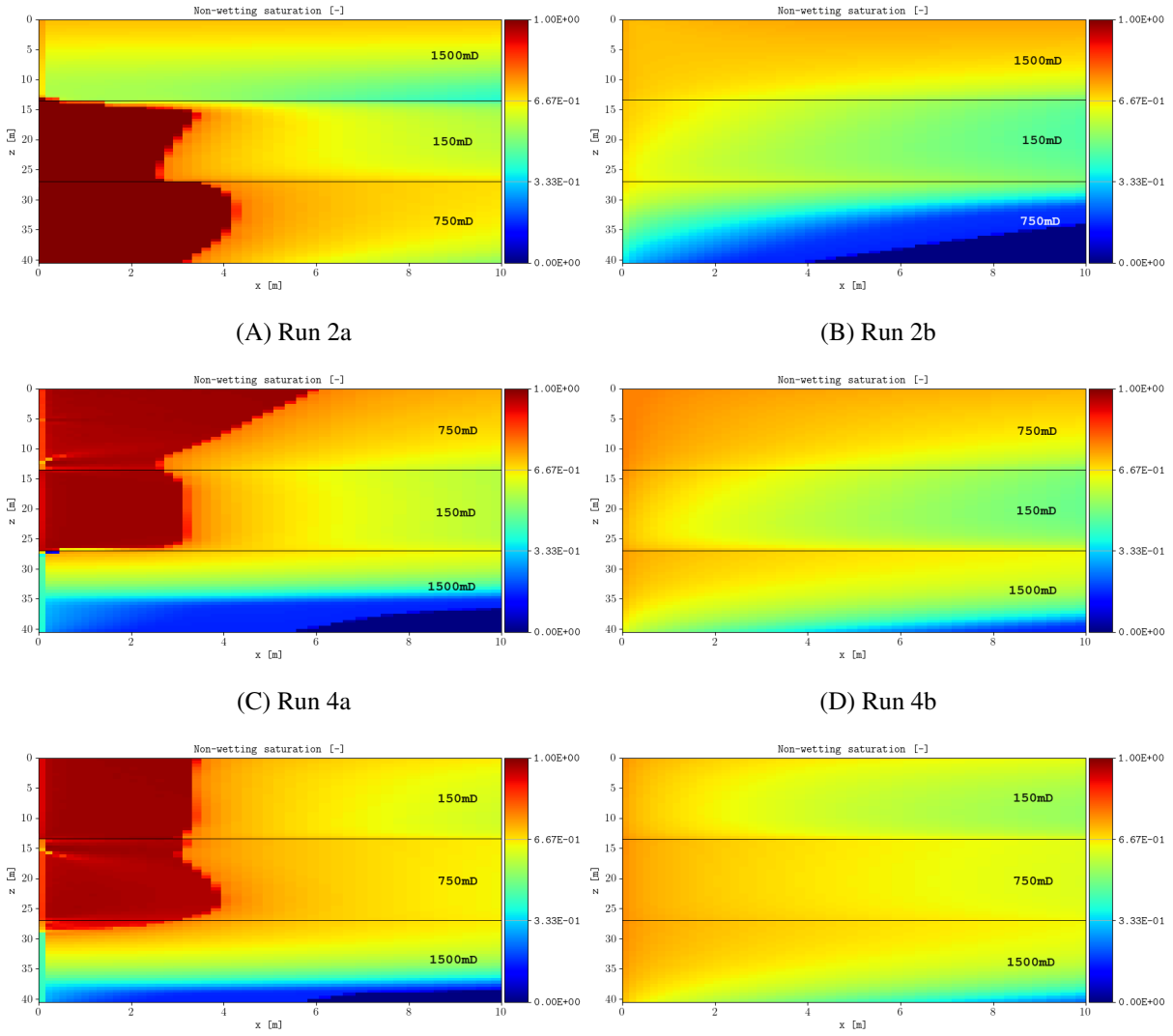

(A) Run 2a

(B) Run 2b

(C) Run 4a

(D) Run 4b

(E) Run 6a

(F) Run 6b

Figure 4.12: Schematic of the spatial distribution of CO_2 saturation after injection for Run 2, Run 4 and Run 6. A: Run 2a (including salt precipitation), B: Run 2b (excluding salt precipitation), C: Run 4a (including salt precipitation), D: Run 4b (excluding salt precipitation), E: Run 6a (including salt precipitation), F: Run 6b (excluding salt precipitation). The vertical axis represents depth along the well and the horizontal axis represents meters away from the well. The three layers in each run are indicated by separating lines and their associated permeabilities are included for clarification. The scale represents the fraction of CO_2 in the pore space of each cell.

4.1.4 Three Layered Runs With Random Generated Permeability

Run 7R - Run 12R consist of three layers with random generated permeabilities. The homogeneous run (Run 16H) is included in this section for comparison. All runs exhibit a permeability average of 800 mD. These runs are included to further investigate how heterogeneity affects the distribution of CO_2 saturation after salt precipitation in the near well region. Table 4.2 shows total grid cells with any fraction of salt precipitation for each run and total cells with any fraction of salt precipitation in each layer for each run. The table illustrate that the heterogeneous run (Run 16H) and the slightly heterogeneous runs (Run 7R and Run 9R) contain the least number of total cells with salt precipitation. Another observation is that the runs displaying the most total cells with solid salt are Run 8Ra and Run 12Ra, which are more heterogeneous. This could indicate that the dry-out zone is greater in the more heterogeneous runs.

Table 4.2: Total number of grid cells in the entire formation and in each layer containing any fraction of precipitated salt for Run 7Ra - Run 12Ra. Each run consists of three layers with random generated permeability. One homogeneous run (Run 16H) is included in this table for comparison.

Run number identifier	Total cells with salt precipitation	Permeability in each layer [mD]	Cells with salt precipitation in each layer
7Ra	820	947	85
		801	78
		652	657
8Ra	1125	768	665
		92	432
		1540	28
9Ra	690	691	189
		922	27
		787	474
10Ra	929	501	729
		1275	146
		624	54
11Ra	959	418	753
		1167	179
		815	27
12Ra	1013	244	764
		1065	222
		1091	27
16H	668	800	668

Another observation is that in Run 1 - Run 6, the high permeability layer (1500 mD) had the least total cells with salt precipitation. This is not the case for all of the random generated permeability runs, as they display more variation in which the least total cells with salt precipitation are located. This indicates that formation heterogeneity affects the spatial distribution of precipitated salt. Figure 4.13 illustrates the distribution of salt precipitation after CO_2 injection for Run 7Ra, Run 9Ra and Run 16H, the first two runs being slightly heterogeneous, and with small permeability ratios between layers. Run 16H is homogeneous.

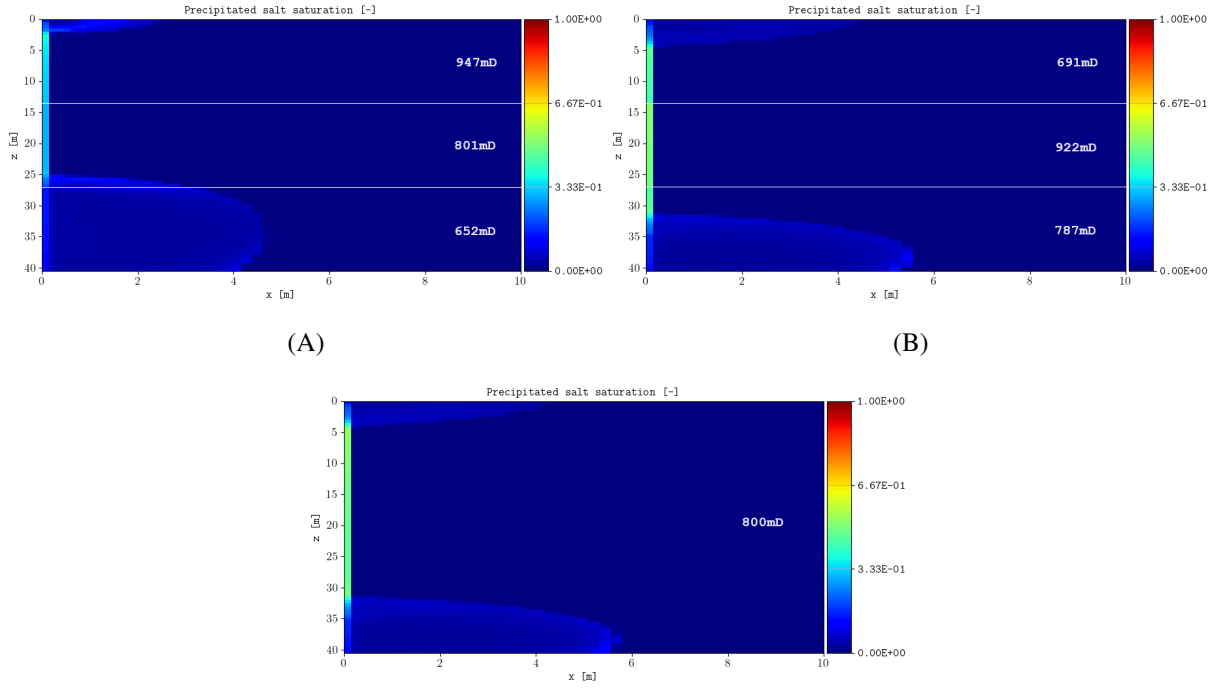

Figure 4.13: Plot of the the spatial distribution of salt precipitation after CO_2 injection. A: Run 7Ra, B: Run 9Ra, C: Run 16H. The scale illustrates the fraction of solid salt in each cell. The vertical axis represents depth along the injection well and the horizontal axis represents meters away from the well. The runs consist of three layers each and their associated permeabilities are included for clarification.

Figure 4.13 display larger vertical extents of salt precipitation next to the well for the homgoeneous and slightly heterogeneous runs, than for the previous discussed runs, indicating greater blockage by solid salt. This will effect injection of CO_2. Miri et al. (2015) describes that injectivity can be reduced as a result of near-well salt precipitation, which supports this assumption. Run 10R and Run 11R, similar to Run 3 and Run 5, have their highest permeability layer located in the middle, see Figure 4.14. In Run 10Ra and Run 11Ra most of the salt precipitation has occurred in the bottom two layers. Run 10Ra displays an accumulation of solid salt between the bottom and middle layer. Run 11Rb displays no such accumulation of cells with high fractions of solid salt between layers. This indicates that the permeability ratio between layers has affected the local accumulation of solid salt between layers in these results.

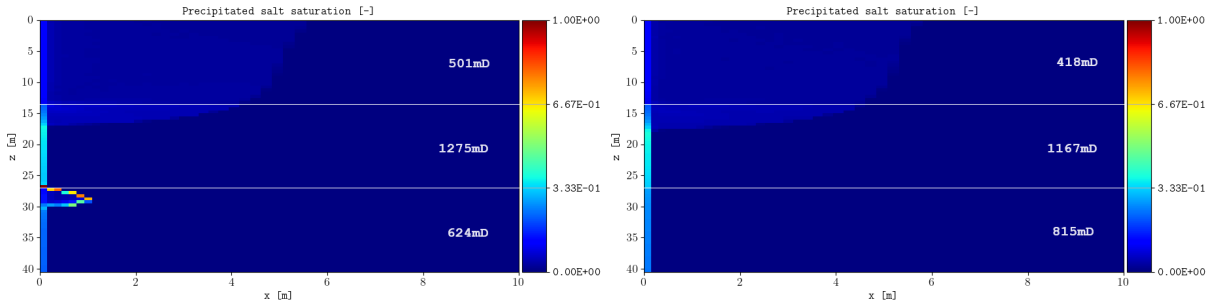

(A) (B)

Figure 4.14: Schematic of the spatial distribution of salt precipitation after CO_2 injection. A: Run 10Ra, B: Run 11Ra. The scale illustrates the fraction of solid salt in each cell. The vertical axes represent depth along the injection well and the horizontal axes represent meters away from the well. The runs consist of three layers each and their associated permeabilities are included for clarification.

Figure 4.15 illustrates salt precipitation for Run 8Ra and Run 12Ra. Run 12Ra was found to be heterogeneous, and Run 8R was found to be very heterogeneous. Run 8R is the run with the largest permeability ratio between the bottom and middle layer, out of any run. An accumulation of solid salt can be observed along this border in Run 8Ra, in contrast to Run 12Ra, which displays no such accumulation with high fractions of salt precipitation in any cells. Based on the results so far, a solid salt accumulation was expected in this run because of the permeability ratio between the top and middle layer. The permeability in the bottom and middle layer in Run 12Ra are similarly high, and it is evident that salt has precipitated next to the well in both layers. This indicates more clogging near the injection well in Run 12Ra than in Run 8Ra.

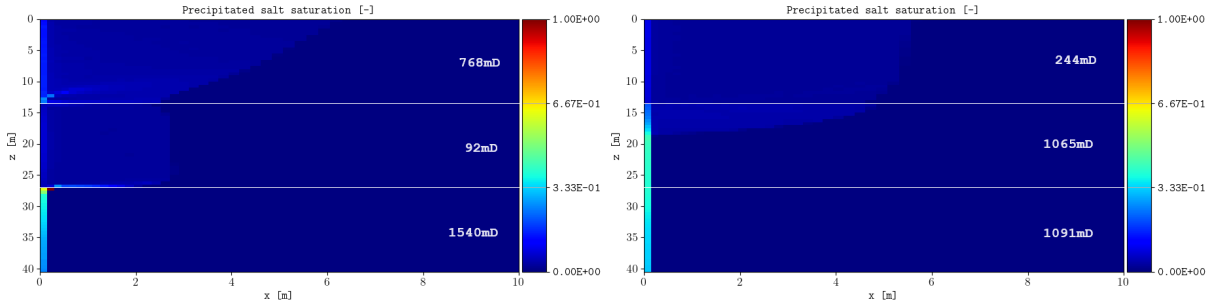

(A) (B)

Figure 4.15: Schematic of the spatial distribution of salt precipitation after CO_2 injection. A: Run 8Ra, B: Run 12Ra. The scale illustrates the fraction of solid salt in each cell. The vertical axes represent depth along the injection well and the horizontal axes represent meters away from the well. The runs consist of three layers each and their associated permeabilities are included for clarification.

The runs presented this far (Run 1 - Run 6, Run 7R - Run 12R and Run 16H) have displayed various fractions of salt precipitation next to the well. Run 16H, as well as the slightly heterogeneous runs (Run 7R and Run 9R) displayed a longer vertical extent of precipitated salt along the well than Run 1 - Run 6, which was very heterogeneous runs. This indicates that the degree of

heterogeneity affects the level of salt precipitation near the well. Consequently, CO_2 injection will be affected, as described by Miri et al. (2015). The effect of heterogeneity on near well salt precipitation can be further investigated by comparing the fraction of salt precipitation next to the well in a homogeneous run (Run 16H) versus a very heterogeneous run (Run 8R).

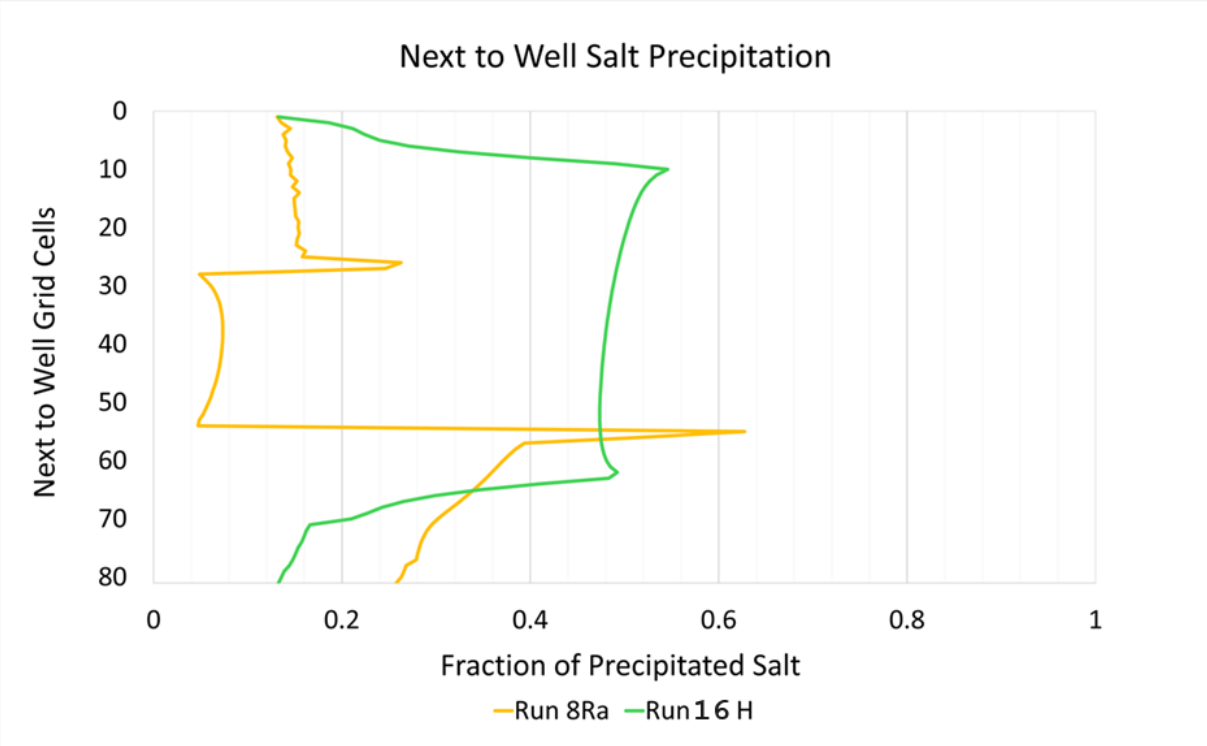

Figure 4.16: Graphical representation of the fraction of precipitated salt in each cell next to the injection well for Run 8Ra (yellow) and Run 16H (green). The 81 cells next to the well are represented on the vertical axis, and the horizontal axis represent the fraction of precipitated salt in the pore space of each cell.

Figure 4.16 illustrate that Run 16H has a much longer vertical extent with high fractions of solid salt next to the well than Run 8Ra. I Run 8Ra, the highest fraction of precipitated salt is located in the bottom layer which consist of the highest permeability in that run (1540 mD). The average percentage of precipitated salt in these cells in Run 16H is 40.2% and the average percentage of precipitated salt in Run 8Ra is 18.6%. This illustrates a greater blockage by solid salt next to the well in the homogeneous run. Run 9Ra was the run with the lowest Dykstra-Parsons coefficient, indicating that the run is only slightly heterogeneous. The development of salt precipitation and CO_2 saturation as a function of time, for Run 9Ra, is illustrated in Figure 4.17. Here, data for one cell in each layer is demonstrated. The first cell is located in the top layer (691 mD) at 6.25 m depth from top to bottom of the injection well. The second cell is located in the middle layer (922 mD) at 20.8 m and the third cell is located in the bottom layer (787 mD) at 33.8 m. These locations were used because they are located approximately in the middle of each layer, and it provided an opportunity to compare how the spatial distribution of salt precipitation affected injection of CO_2 in areas with different permeability.

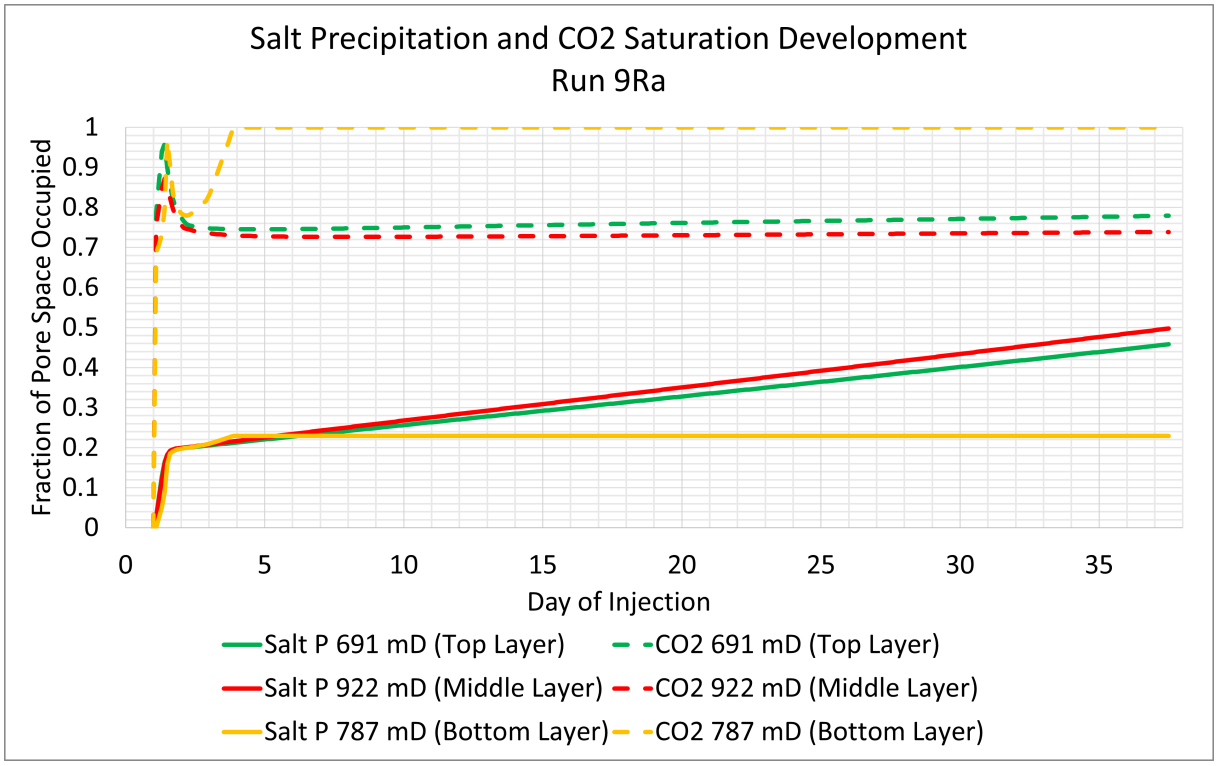

Figure 4.17: Salt precipitation and CO_2 saturation development in the pore space of three cells as a function of time. The first cell is located at the top layer (691 mD), the second cell is located in the middle layer (922 mD), and the third cell is located at the bottom layer (787 mD). The colors illustrates permeability: red represents the highest permeability, yellow represents the medium permeability and green represents the lowest permeability. The solid lines represent salt precipitation (Salt P) and the dashed lines represent CO_2 saturation.

Figure 4.17 illustrates that salt precipitation in Run 9Ra occurred in every cell at the beginning of injection, in contrast to Run 1a, where salt precipitation in the bottom layer (150 mD) started later, see figure 4.2. At the end of injection, the top and middle layered cells have a total of 45.8% and 49.8% of their pore spaces filled with solid salt, respectively. In Run 1, the two cells with the highest salt precipitation at the end of injection were located in the top and bottom layer. The top layer cell had 34.9% of its pore space filled with solid salt and the bottom layer cell had 19.9% of its pore space filled with solid salt at the end of injection. This demonstrates a significant difference between the Run 9Ra and Run 1a. The reason for this difference could be because of the variation in degree of heterogeneity. In a very heterogeneous run, less solid salt precipitated next to the well than in the slightly homogeneous and completely homogeneous runs.

Saturation profiles for Run 8R, Run 10R, Run 11R and Run 12R are presented in Figure 4.18. These are the most heterogeneous runs of all random generated permeability runs. From the Dykstra-Parsons coefficient, Run 10R, Run 11R and Run 12R were found to be heterogeneous, and Run 8R was found to be very heterogeneous.

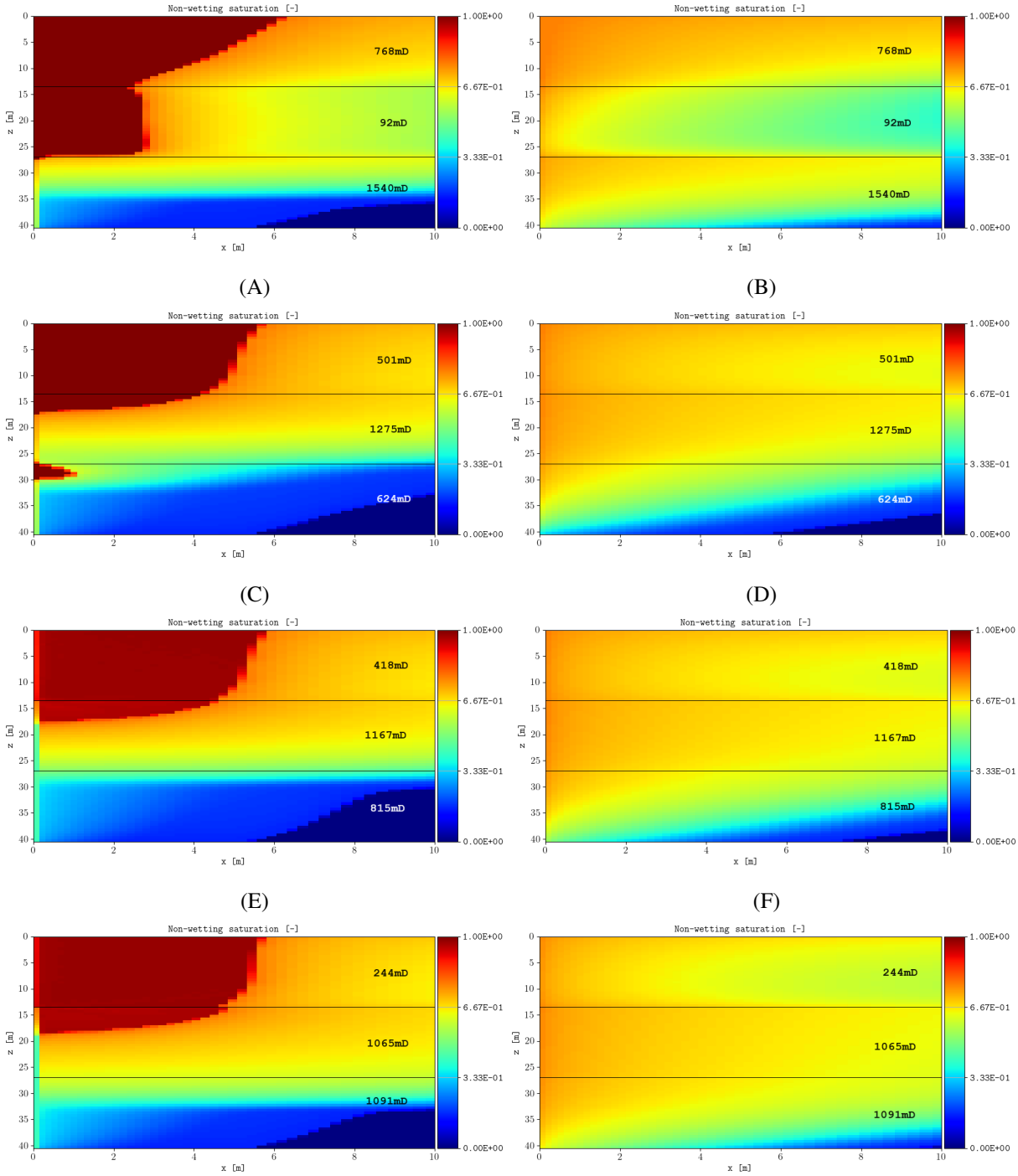

Figure 4.18: Schematic of the spatial distribution of CO_2 saturation after injection for Run 8R, 10R, 11R and Run 12R. A: Run 8Ra (including salt precipitation), B: Run 8Rb (excluding salt precipitation), C: Run 10a (including salt precipitation), D: Run 10Rb (excluding salt precipitation), E: Run 11Ra (including salt precipitation), F: Run 11Rb (excluding salt precipitation), G: Run 12Ra (including salt precipitation), H: Run 12Rb (excluding salt precipitation). The vertical axis represents depth along the well and the horizontal axis represents meters away from the well. The three layers in each run are indicated by separating lines and their associated permeabilities are included for clarification. The scale represents the fraction of CO_2 in the pore space of each cell.

When salt precipitation is included in these runs they have more total cells with solid salt than the less heterogeneous runs, see Table 4.2. Run 8Ra, Run 10Ra, Run 11Ra and Run 12Ra all have most of their dry-out zones located towards the top in the formation. This could be because of capillary backflow from the high permeability layers, located in the middle and bottom of the formations. The dry-out zone, as previously discussed, illustrates a large difference in CO_2 saturation when compared to Run 8Rb, Run 10Rb, Run 11Rb and Run 12Rb where salt precipitation has not occurred.

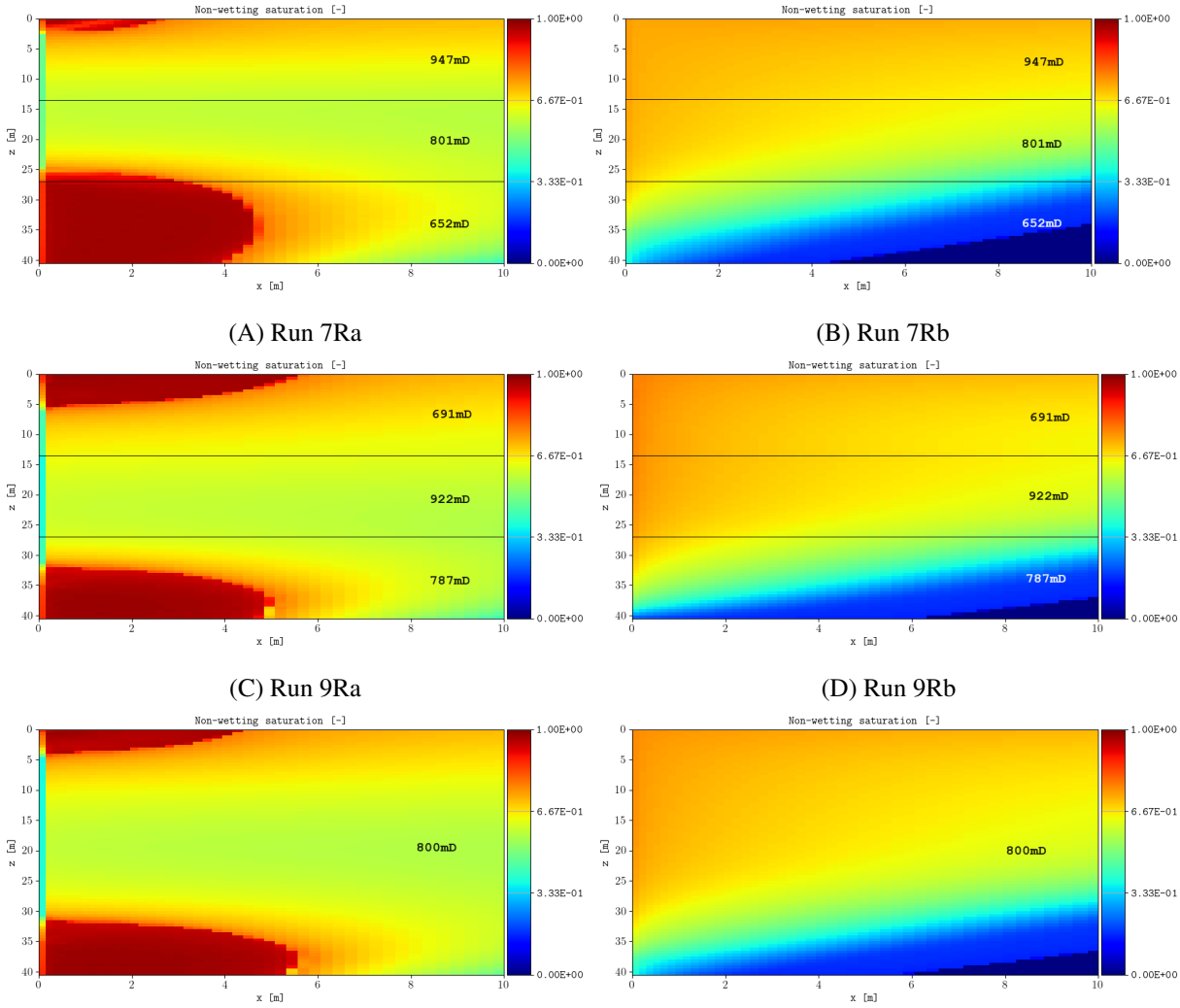

(A) Run 7Ra

(B) Run 7Rb

(C) Run 9Ra

(D) Run 9Rb

(E) Run 16Ha

(F) Run 16Hb

Figure 4.19: Schematic of the spatial distribution of CO_2 saturation after injection for Run 7Ra, Run 9Ra and Run 16H. A: Run 7Ra (including salt precipitation), B: Run 7Rb (excluding salt precipitation), C: Run 9Ra (including salt precipitation), D: Run 9Rb (excluding salt precipitation), E: Run 16Ha (including salt precipitation), F: Run 16Hb (excluding salt precipitation). The vertical axis represents depth along the well and the horizontal axis represents meters away from the well. The three layers in Run 7R and Run 9R are indicated by separating lines. The permeabilities in each run are included for clarification. The scale represents the fraction of CO_2 in the pore space of each cell.

As discussed previously, Run 7R and Run 9R are only slightly heterogeneous and therefore display similar physics as Run 16H, which is completely homogeneous, see Figure 4.19. This figure illustrate less CO_2 saturation in the layers where solid salt has clogged the well, compared to Run 7Rb, Run 9Rb and Run 16Hb. The dry-out zone in these three runs are located at the top and at the bottom of the medium. It was not expected that a dry-out zone would occur at the bottom in the homogeneous run because of the gravity effects. This means there could be an error in the numerical simulations. The dry-out zone does, however, present another clear distinction when compared to run 7Rb, 9Rb and 16Hb where salt precipitation is excluded.

4.1.5 Twelve Layered Runs With Random Generated Permeabilities

This section presents the last three runs which consist of more complex layering. Each run consists of four zones with three layers each, providing a total of 12 layers. Each zone has an average permeability of 800 mD. Table 4.3 presents total cells with any fraction of solid salt in the entire formation as well as in each layer of each run.

Table 4.3: Number of grid cells with salt precipitation for run 13RMa, Run 14RMa and 15RMa. Total cells in each layer represents total cells with solid salt in each layer in each zone. To clarify, for Run 13RMa, the 1012 mD layer is present four times in the medium, on in each zone, and the numbers correspond to these layers. This means that a total of 180 cells with salt precipitation are present in the top 1012 mD layer, 103 total cells in the second 1012 mD layer, and so forth.

Run number identifier	Total cells with salt precipitation	Permeability in each layer [mD]	Cells with salt precipitation in each layer in each zone
13RMa	847	1012	180, 103, 6, 7
		802	163, 42, 7, 9
		586	138, 109, 7, 89
14RMa	768	998	227, 28, 6, 7
		673	204, 7, 7, 29
		729	139, 7, 7, 100
15RMa	955	558	190, 155, 41, 7
		1404	167, 104, 7, 6
		438	132, 112, 27, 7

Run 15Rma was previously found to be very heterogeneous, and displays the most total number of cells with solid salt. Run 13RMa and Run 14RMa were found to be slightly heterogeneous. All runs display more variation in each layer compared to the previously discussed runs, however, a general trend is that the bottom layers contain the least number of cells with salt precipitation. Figure 4.20 illustrates the spatial distribution of salt precipitation after injection of CO_2 for Run 13RMa - Run 15RMa.

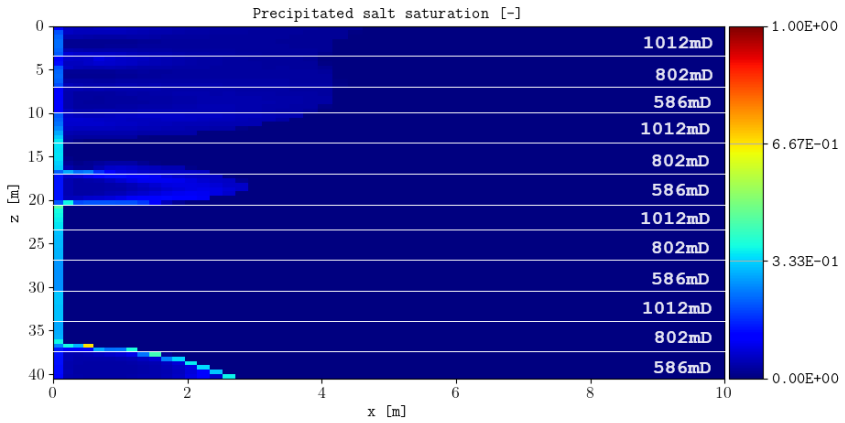

(A)

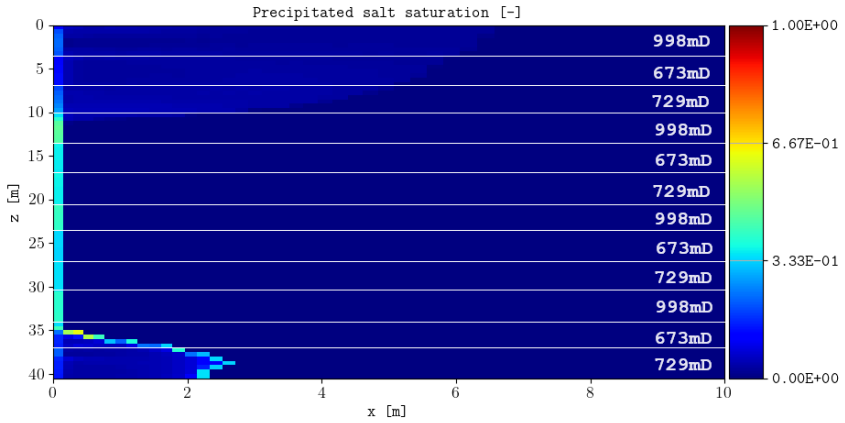

(B)

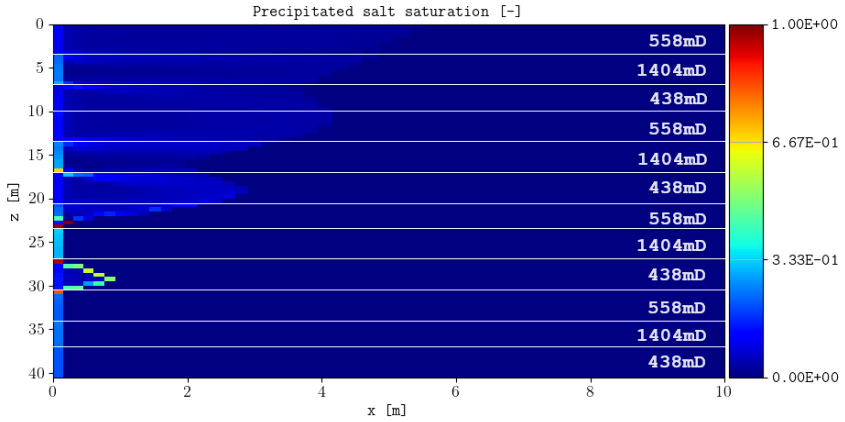

(C)

Figure 4.20: Plot of the spatial distribution of salt precipitation after CO_2 injection. A: Run 13RMA, B: Run 14RMA, C: Run 15RMA. The scale illustrates the fraction of solid salt in each cell. The vertical axis represents depth along the injection well and the horizontal axis represents meters away from the well. The runs consist of three layers each and their associated permeabilities are included for clarification.

From Figure 4.20, it is evident that the highest fraction of salt precipitation near the injection well has occurred in Run 14RMa, which is a slightly heterogeneous run. Run 13RMa displays less fraction of solid salt in that area, and Run 15RMa, which is very heterogeneous, displays the

least. These findings are consistent with the previous runs, where the homogeneous run (Run 16H) had a large vertical extent with salt precipitation next to the well. This implies that a large area of the well is clogged, which affects injection of CO_2. These assumptions are also consistent with the findings of Berntsen et al. (2019), which concluded that clogging occurred close to the wellbore. The fraction of solid salt in the pores spaces of each cell next to the well, for Run 13RMa, Run 14RMa and Run 15RMa, are displayed in Figure 4.21.

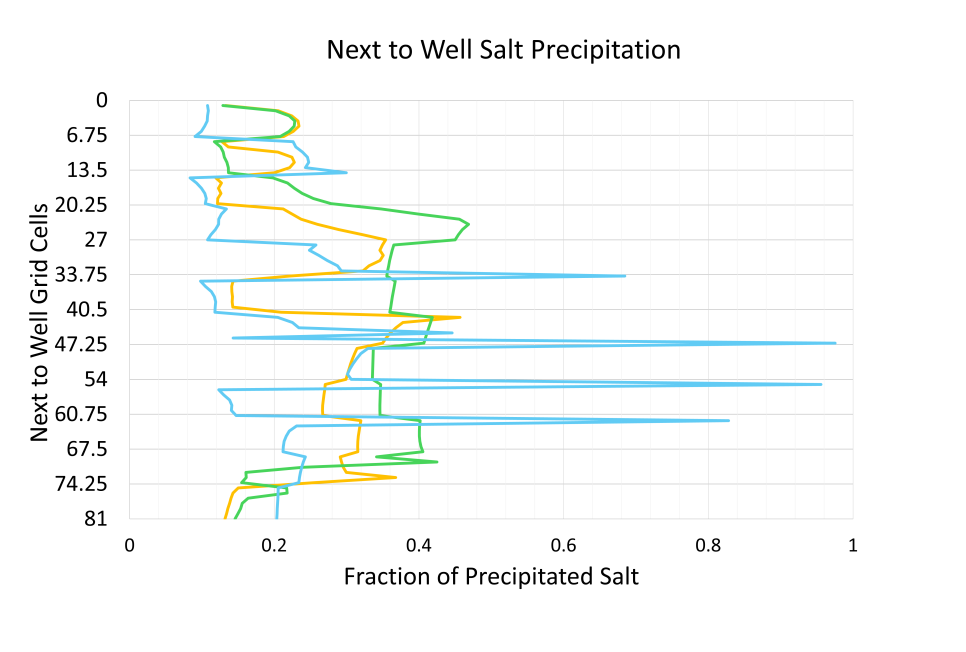

Figure 4.21: Graphical representation of the fraction of precipitated salt in each cell next to the injection well for Run 13RMa (yellow), Run 14RMa (green) and Run 15RMa (blue). The 81 cells next to the well are represented on the vertical axis, and the horizontal axis represent the fraction of precipitated salt in the pore space of each cell. The lines on the figure represent the border between each of the 12 layers.

From Figure 4.21, Run 13RMa (yellow) displays two minor spikes with higher fractions of salt precipitation. The largest spike is located in grid cell 42 at a depth of 20.8 m, and this cell is filled with 45.7% solid salt at the end of injection. The second spike is located in cell 73 at a depth of 36.3 m, and this cell is filled with 36.8% solid salt at the end of injection. Run 14RMa (green) reaches its highest value of solid salt in cell 24 at a depth of 11.8 m, when 46.8% of the pore space is filled with solid salt. The next 55 cells all contain between 30-40% salt precipitation in this run. Run 15RMa has four large spikes of solid salt. Cell number 47, located at 23.25 m depth, is filled with 97.5% solid salt at the end of injection. The other three cells reach percentages of 68.5%, 95.6% and 82.8% solid salt. These four cells can be observed in Figure 4.20C. Run 14RMa displays the largest average of solid salt in the cells next to the well, which is 30.4%. As previously discussed, this implies a significant blockage near the injection well in the slightly heterogeneous runs. This affects injection of CO_2, as can be observed by the saturation profiles for the twelve layered runs, see Figure 4.22.

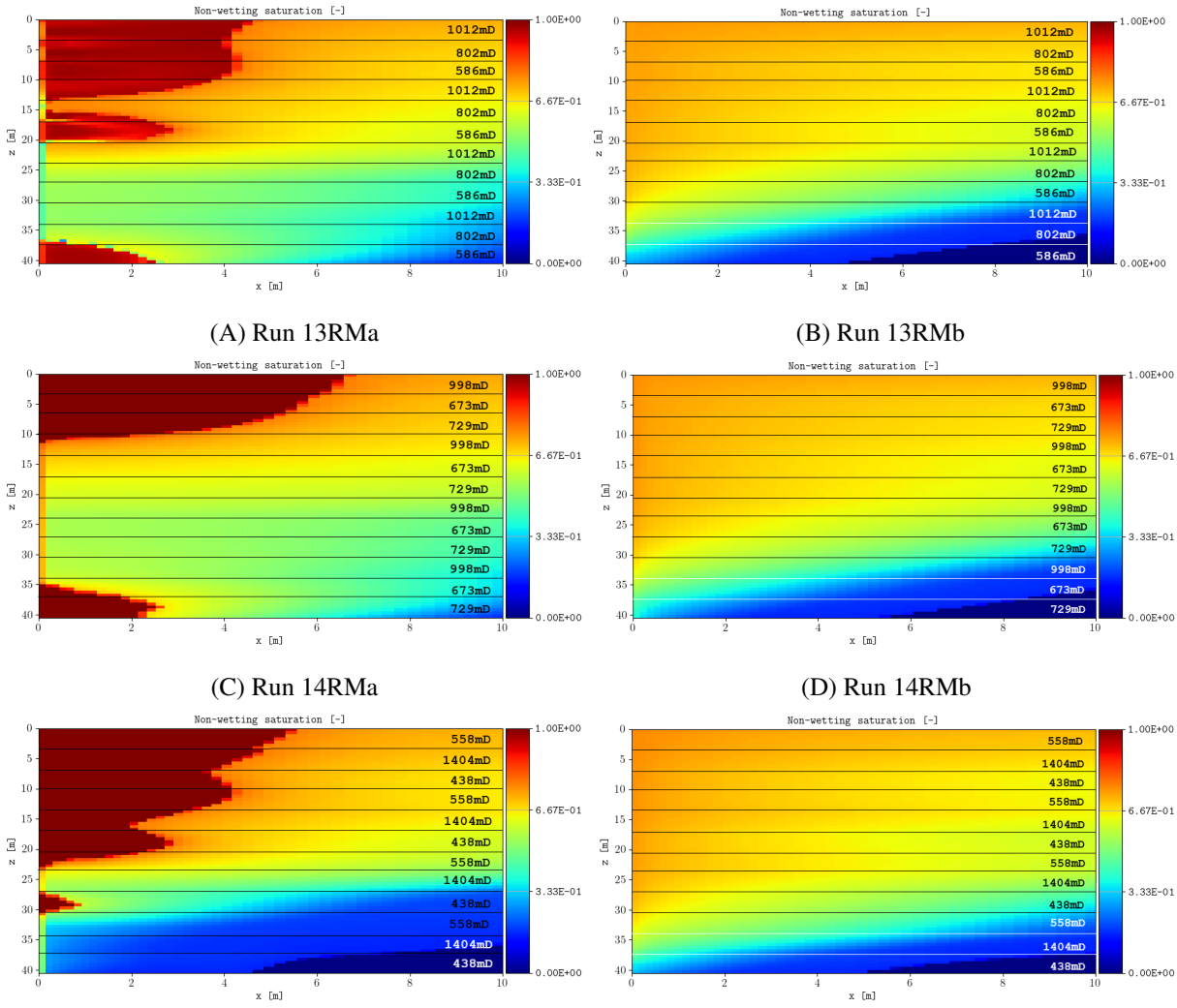

(A) Run 13RMa

(B) Run 13RMb

(C) Run 14RMa

(D) Run 14RMb

(E) Run 15RMa

(F) Run 15RMb

Figure 4.22: Schematic of the spatial distribution of CO_2 saturation after injection for Run 13RMa, Run 14RMa and Run 15RMa. A: Run 13RMa (including salt precipitation), B: Run 13RMb (excluding salt precipitation), C: Run 14RMa (including salt precipitation), D: Run 14RMb (excluding salt precipitation), E: Run 15RMa (including salt precipitation), F: Run 15RMb (excluding salt precipitation). The vertical axes represent depth along the well and the horizontal axes represent meters away from the well. The layers and their associated permeability in each run are indicated by separating lines. The scale represents the fraction of CO_2 in the pore space of each cell.

Run 13RMa displays variation in the location of the dry-out zone, mostly at the top of the medium but also between the layers where solid salt has clogged the pores. Run 14RMa display similar results to Run 16H, as expected, where the dry out zone is located at the top of the formation. It was, however, not expected that dry-out would occur at the bottom in this run. In Run 15RMa the dry out zone is located mostly at the top of the medium with a few cells in the 438 mD layer at the bottom of the third zone. Less cells next to the well is blocked by precipitated salt in this run, which is consistent with previous heterogeneous and very heterogeneous runs. This means CO_2 injection was not affected to the same degree, as can be seen when compared to

Run 15RMb. The slightly heterogeneous runs (Run 13RMa and Run 14RMa) display that solid salt has clogged several layers near the injection well, when compared to Run 13RMb and Run 14RMb, and consequently effected injection of CO_2.

4.2 SPE CSP 11B Case

This section present the results form the SPE CSP 11B benchmark case. This case was chosen to study a more realistic system. One case has been simulated over 25 years including salt precipitation, where two cells at the bottom of the well consist of the following permeabilities from top to bottom: 100 mD and 1500 mD. One run with identical permeabilities has also been studied without salt precipitation, however, this run was only simulated for three years. Figure 4.23 illustrates the development of salt precipitation and CO_2 saturation for the two cells in the run including salt precipitation. These two cells were chosen because they are located next to the well, as the near-well region is the location where literature has found capillary backflow to be a chief component for precipitation of salt (Norouzi et al., 2021). After 14 years, salt precipitation occurred in one additional cell. This cell is located above the 100 mD cell and has a permeability of 1013.25 mD (the original permeability of the facie, as described in chapter 3.3.2). For that reason this cell is included in the figure.

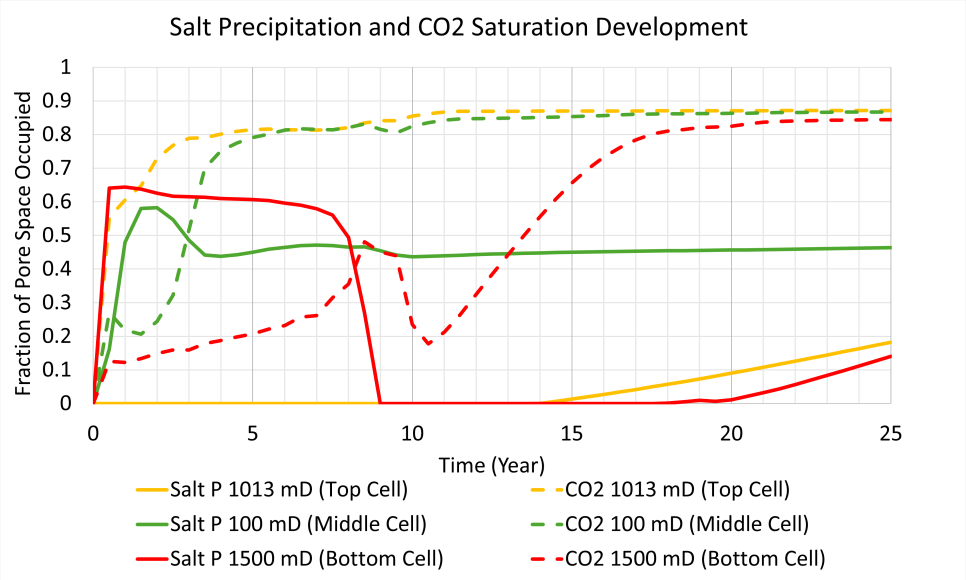

Figure 4.23: Time series of salt precipitation and CO_2 saturation development for the SPE CSP 11B benchmark study. The figure represent the development in three cells over 25 years. The colors illustrates permeability: red represents the cell with highest permeability, yellow represents the cell with medium permeability and green represents the cell with lowest permeability. The solid lines represents salt precipitation (indicated as Salt P in the legends) and the dashed lines represent CO_2 saturation.

From Figure 4.23 it is evident that in the highest permeability cell (1500 mD), represented by the solid red line on the figure, a significant fraction of salt precipitates during the first year of

injection. The maximum fraction of salt precipitation in this cell was 64.4% solid salt at the beginning of year one. From year one to year nine solid salt steadily decreases to 0.00%. From year 18 to end of injection the cell exhibits salt precipitation until 14.1% of the cell is filled with solid salt. Similarly, the 100 mD cell displays salt precipitation from year one of injection, however, the fractions of solid salt in the cell is lower than in the 1500 mD layer. The maximum fraction of solid salt is reached at year 1.5, where 58.0% of the pore space is filled with solid salt. At year 10, salt precipitation stabilizes with an average of 45.0% solid salt over the next 15 years. After year 14, salt precipitation occurred in the 1013 mD cell. The maximum fraction of solid salt in this cell was 18.2% at the last year of injection. Figure 4.24 represent the spatial distribution of CO_2 over three years including and excluding salt precipitation.

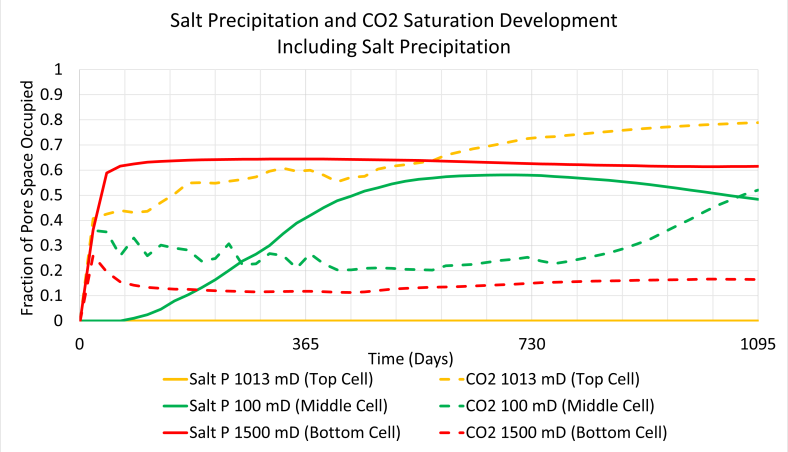

(A)

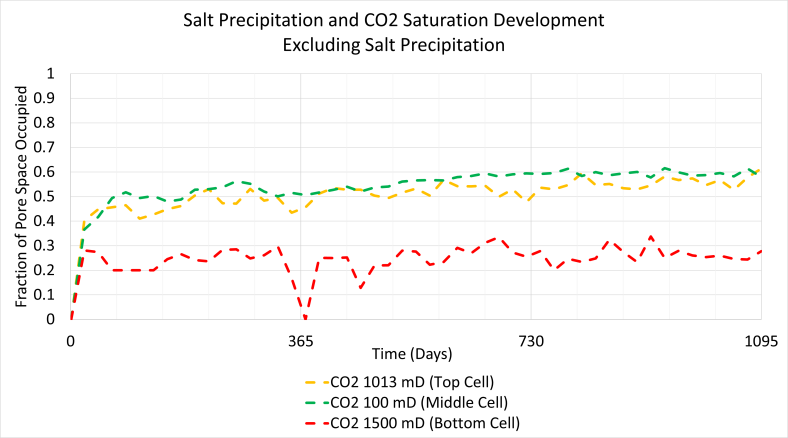

(B)

Figure 4.24: Time series on the spatial distribution of CO_2 for the SPE CSP 11B benchmark study. A: Including salt precipitation. B: Excluding salt precipitation. The figures represent CO_2 saturation in three cells over three years. The colors illustrate permeability: red represents the cell with highest permeability, yellow represents the cell with medium permeability and green represents the cell with lowest permeability. The solid lines represent salt precipitation (indicated as Salt P in the legends) and the dashed lines represent CO_2 saturation.

From the figure it is evident that the fraction of CO_2 saturation in the cells are different when salt precipitation occurs versus when it does not. For the highest permeability cell (1500 mD), the run with salt precipitation resulted in less CO_2 saturation in the cell. Average CO_2 saturation in this cell during the three years was 14.1%, and average CO_2 saturation in the run excluding salt precipitation over the same time period was 24.3%. The cell with the lowest permeability (100 mD) displayed a larger difference in CO_2 saturation when salt precipitation was included versus when it was excluded, than the highest permeability cell. In this cell, when salt precipitation was included, the average CO_2 saturation was 27.7%, and when it was excluded, average CO_2 saturation in the cell was 54.1%. In the top cell with the original permeability (1013.25mD), CO_2 saturation reached higher fraction in the cell when salt precipitation was included versus when it was excluded. The average percentage of CO_2 saturation with salt precipitation was 62.0%, and the average percentage without salt precipitation was 50.5%.

4.3 Comparison of All Runs

A total of 32 different runs have been discussed for the layered case, as well as two runs for the SPE CSP 11B benchmark case. The SPE CSP 11B benchmark case had its highest fraction of precipitated salt in the 1500 mD layer, which was located at the bottom of the injection well, see Figure 4.23. This displayed similar results as for Run 1a - Run 6a in the layered case, where the highest fractions of precipitated salt also occurred in the 1500 mD layer cells near the well. Injection of CO_2 was similarly effected in both cases, where CO_2 saturation decreased after salt had precipitated in the effected layers/cells. The time of this occurrence did, however, vary.

For the layered case, which was a much simpler model, in which injection occurred over a much shorter time, CO_2 saturation in the 1500 mD cell decreased during day one of injection, when 16.4% of the pore space was occupied by solid salt. In the SPE CSP 11 case, CO_2 saturation in the 100 mD cell reached a value of 64% during year one of injection. The low permeability cell in the SPE CSP 11B case (100 mD) had the highest fraction of precipitated salt at the end of injection, while the high permeability cell in Run 1a (1500 mD) had the highest fraction of precipitated salt at the end of injection. This demonstrates a difference between the runs. These two cases do, however, have a significant difference in their complexity, as well as the total time of injection, which affects the comparison of the results.

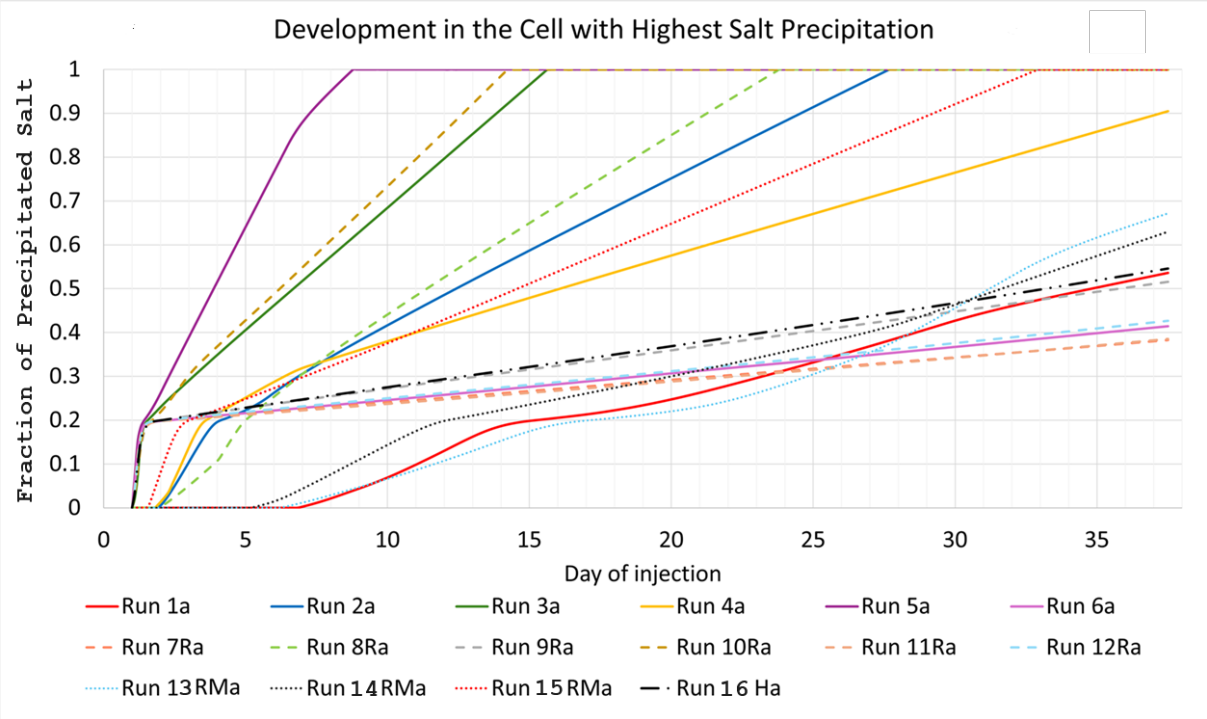

Figure 4.25: Time series of salt precipitation in the one cell containing the highest fraction of solid salt at the end of injection for Run 1a - Run 6a, Run 7Ra - Run 12Ra, Run 13RMa - Run 15RMa and Run 16Ha. The vertical axis represents the fraction of precipitated salt and the horizontal axis represents day of injection. The solid lines represents Run 1a - Run 6a, the dashed lines represent Run 7Ra - Run 12Ra, the round dotted lines represent Run 13Rma - Run 15RMa and the long dash dot line represent Run 16Ha.

Figure 4.25 illustrates the cell in each run containing the highest fraction of solid salt at the end of injection for each run in the layered case. In Run 1a and in Run 13Rma, salt starts to precipitate in the cell after day six of injection. This could be because these cells are located farther away from the well, see Figure 4.4 and Figure 4.20A. The runs where the cell is filled with 99.9-100% solid salt at the end of injection are all either heterogeneous or very heterogeneous runs. The runs where no cells reach 100% solid salt occur regardless of the degree of heterogeneity. These observations indicate that heterogeneity affects the spatial distribution of salt precipitation. It has been found that heterogeneities can be essential in directing of the injected CO_2 as well as for development of salt precipitation (Pruess & Müller, 2009), which align with these observations. An observable trend is that the homogeneous run and the slightly heterogeneous runs had longer vertical extents of salt precipitation next to the injection well than in the other runs. This is illustrated in Figure 4.26.

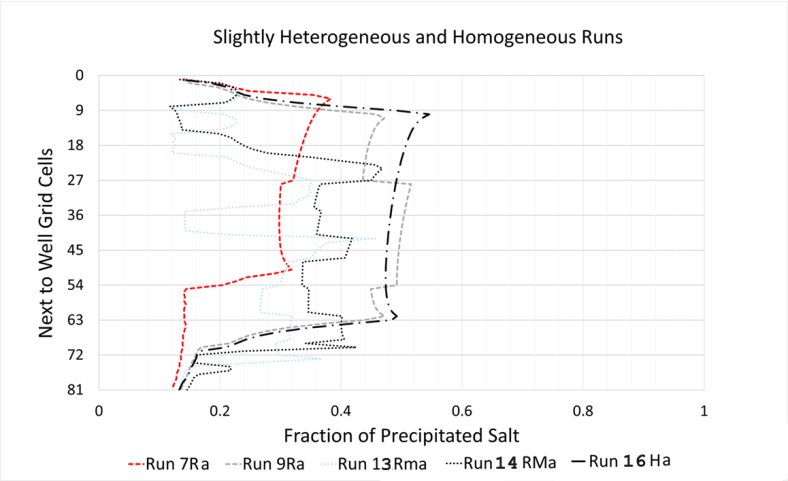

(A)

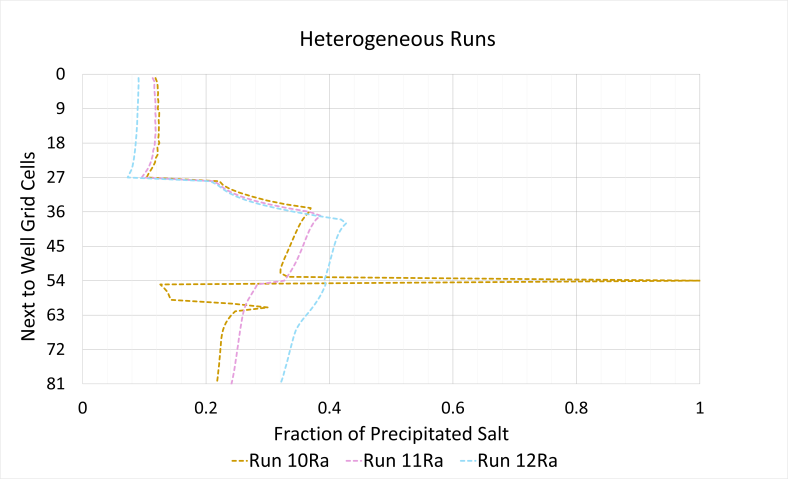

(B)

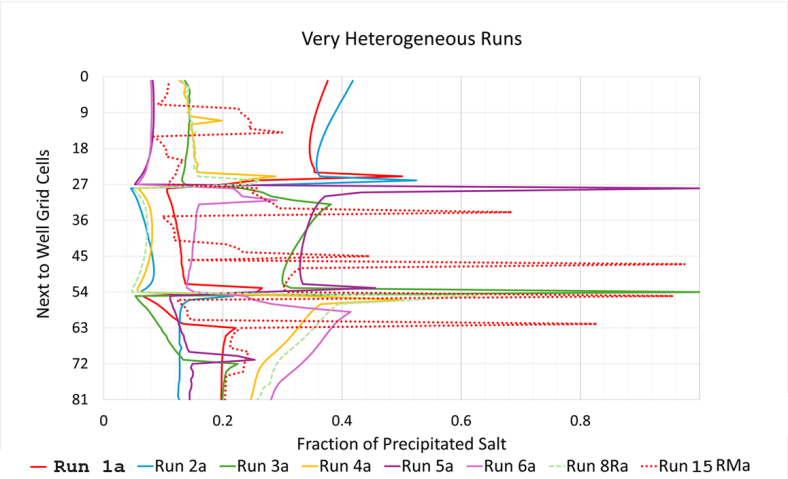

(C)

Figure 4.26: Fraction of precipitated salt in grid cells next to the well for each run in the layered case. A: Slightly heterogeneous runs. B: Heterogeneous runs. C: Very heterogeneous runs. The vertical axes represent each cell next to the injection well, and the horizontal axes represent fraction of precipitated salt in each cell.

Figure 4.26 illustrates that the homogeneous run and the slightly heterogeneous runs were subject to more clogging near the injection well than the heterogeneous runs and very heterogeneous runs. This indicates reduction of injectivity, which can be observed on the CO_2 saturation figures that have been presented for each run. In these runs the CO_2 was blocked by the solid salt and forced into the nearby layers. These observations agree with literature, which has found that salt precipitation can effect injectivity of a reservoir (Guyant et al., 2015; Zhang et al., 2024; Bacci et al., 2011; Norouzi et al., 2021). The heterogeneous- and very heterogeneous runs had less solid salt next to the well, which lead to better injectivity than in the homogeneous and slightly heterogeneous runs.

This can further be investigated by studying the bottom hole pressure for each run, to provide a indication on injectivity, as Norouzi et al. (2021) describes that injection flow rate is reduced when BHP increases. Figure 4.27 illustrates BHP for Run 16H. From the figure it is evident that there is a significantly larger BHP when salt precipitation is included in the run versus when it is excluded. The average BHP during injection for Run 16Ha was 221.6 bar and the average BHP for Run 16Hb was 216.6 bar. The average BHP difference between the runs was 5.057 bar.

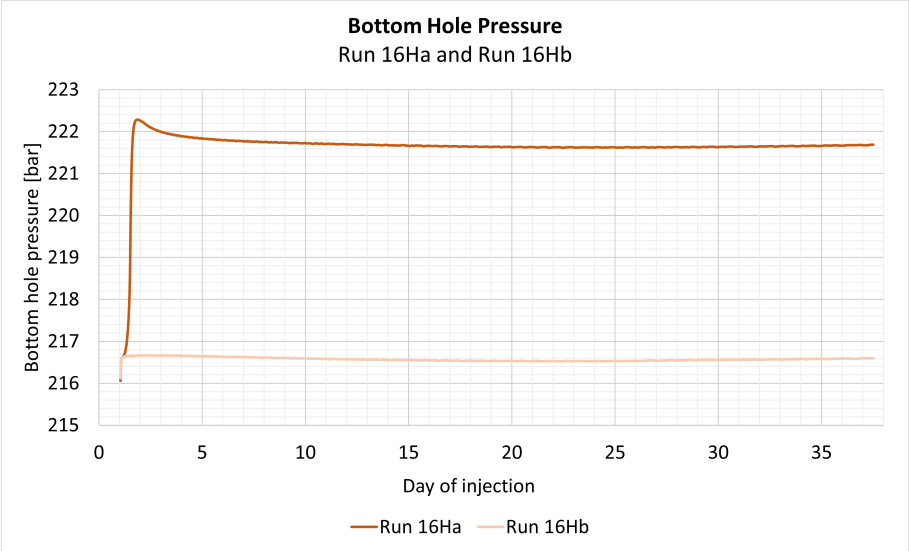

Figure 4.27: Bottom hole pressure during CO_2 injection for Run 16H. Run 16Ha (dark color) has salt precipitation included in the simulation and Run 16Hb (lighter color) does not.

Figure 4.28 illustrates BHP for Run 1 - Run 6. These runs display similar attributes to Run 16H, where the runs including salt precipitation have a higher BHP than the runs excluding salt precipitation. The BHP for the runs with salt precipitation, however, are lower than Run 16Ha. The average BHP for Run 1a - Run 6a is 218.1 bar and the average BHP for Run 1b - Run 6b is 216.5 bar. Run 1 - Run 6 were found to be very heterogeneous, which could be the reason as to the difference in BHP compared to the homogeneous run. These runs displayed better injectivity of CO_2 than Run 16Ha, as discussed previously.

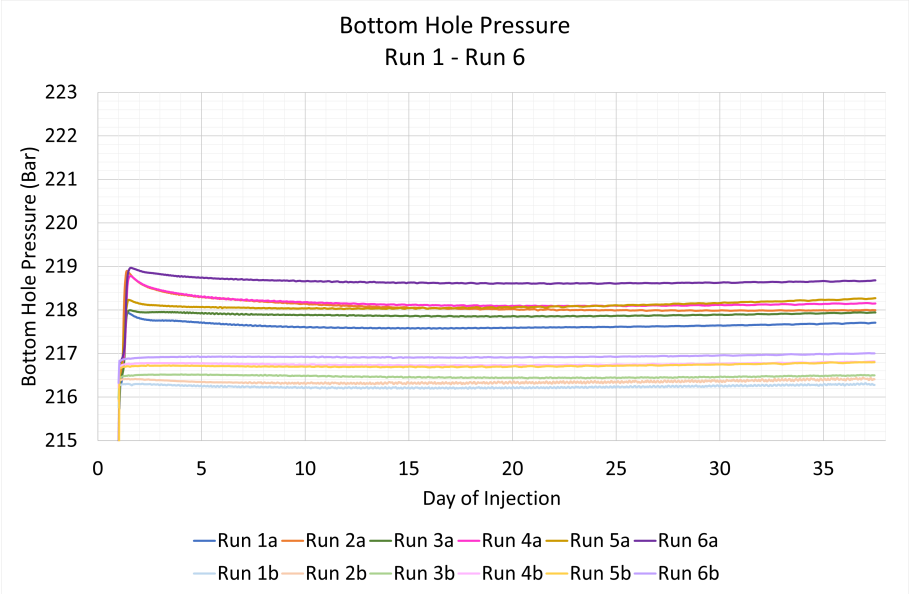

Figure 4.28: Bottom hole pressure during CO_2 injection for Run 1 - Run 6. Runs including salt precipitation (a) are represented by the dark colors and runs excluding salt precipitation (b) are represented by the light colors.

Figure 4.29 illustrates BHP for Run 7Ra - Run 12Ra. Run 9Ra, which was slightly heterogeneous, display similar BHP to Run 16Ha, as expected. Run 12Ra also displays a high BHP. This could be because the bottom and middle layer permeabilities were both high, and it therefore displayed high fractions of solid salt next to the well in both layers.

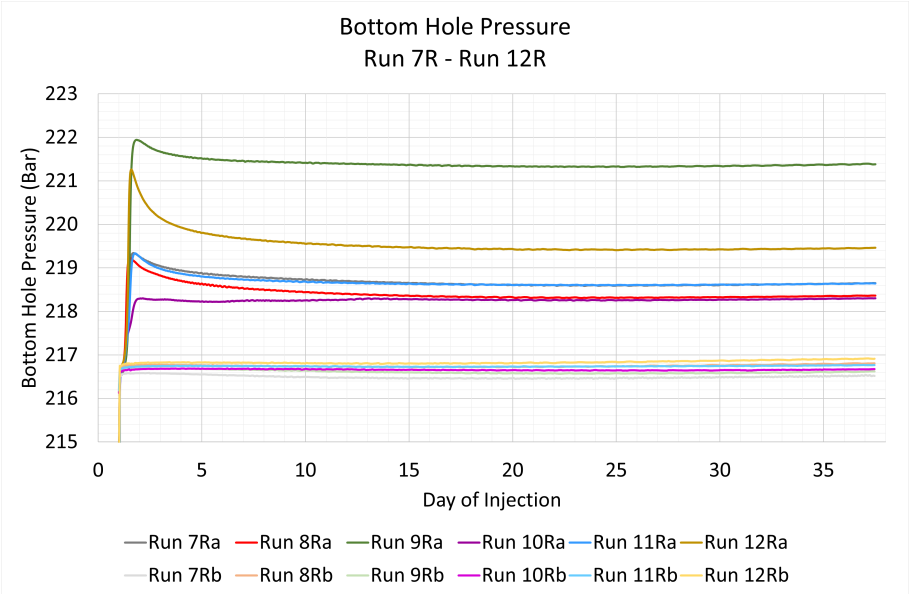

Figure 4.29: Bottom hole pressure during CO_2 injection for Run 7Ra - Run 12Ra. Runs including salt precipitation (a) are represented by the dark colors and runs excluding salt precipitation (b) are represented by the light colors.

Figure 4.30 illustrates BHP for Run 13RMa - Run 15RMa. Run 13 RMa and Run 14RMa were slightly heterogeneous, and both runs displayed higher BHP than Run 15RMa which was very heterogeneous. These results are important because it illustrates that more heterogeneous formations lead to less clogging of the well during CO_2 injection.

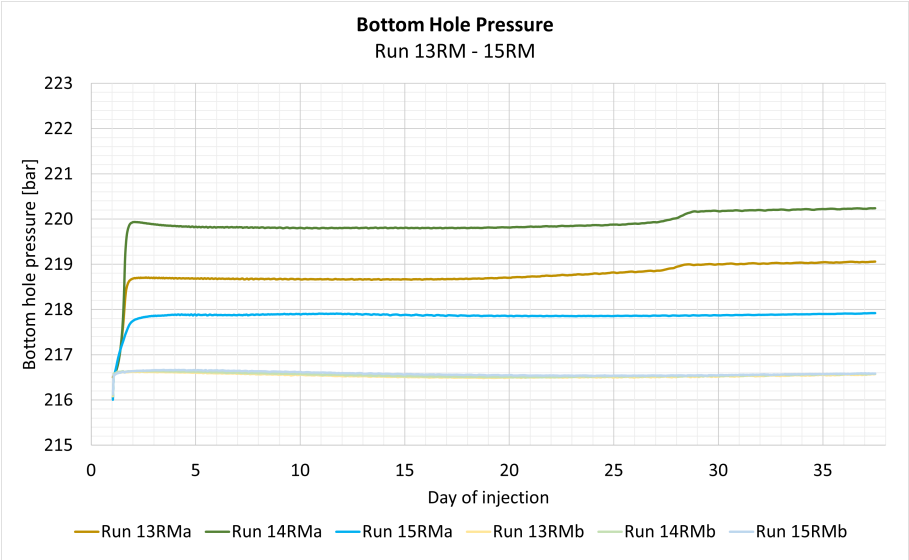

Figure 4.30: Bottom hole pressure during CO_2 injection for Run 13RMa - 15RMa. Runs including salt precipitation are represented by the dark colors and runs excluding salt precipitation are represented by the light colors

These results have illustrated that the homogeneous and slightly heterogeneous runs displayed more cells with high fractions of solid salt next to the well compared to the heterogeneous and very heterogeneous runs. Some of the heterogeneous and very heterogeneous runs displayed spikes with high fractions of solid salt in some cells near the injection well, see Figure 4.26B and Figure 4.26C. This did, however, not affect injection of CO_2 to the same degree as when longer vertical extents of precipitated salt occurred near the well. Another observation is that the heterogeneous and very heterogeneous runs displayed more total cells with any fraction of salt precipitation than the homogeneous and slightly heterogeneous runs, see Figure 4.6, Table 4.2 and Table 4.3. This indicates a larger dry-out zone in these runs. This did, however, not effect the injected CO_2 nearly as much as when high fractions of salt precipitated next to the injection well in the homogeneous and slightly heterogeneous runs.

Figure 4.31 further illustrates that the slightly heterogeneous runs (Run 7Ra, Run 9Ra, Run 13RMa and Run 14RMa), as well as the completely homogeneous run (Run 16Ha) contain less total cells 100% saturated with CO_2, and contain less cells with any fraction of precipitated salt than the other runs. These results align with conclusions from Akindipe et al. (2022), which described that, in an oil reservoir, the time for salt precipitation to occur, as well as its duration and the amount of precipitates, is affected by heterogeneity and wettability of the system. The authors found that homogeneous carbonates contained less saturation of salt than heterogeneous

carbonates. Figure 4.31 illustrate total cells completely dry with CO_2 and total cells with any fraction of salt precipitation for each run in the layered case.

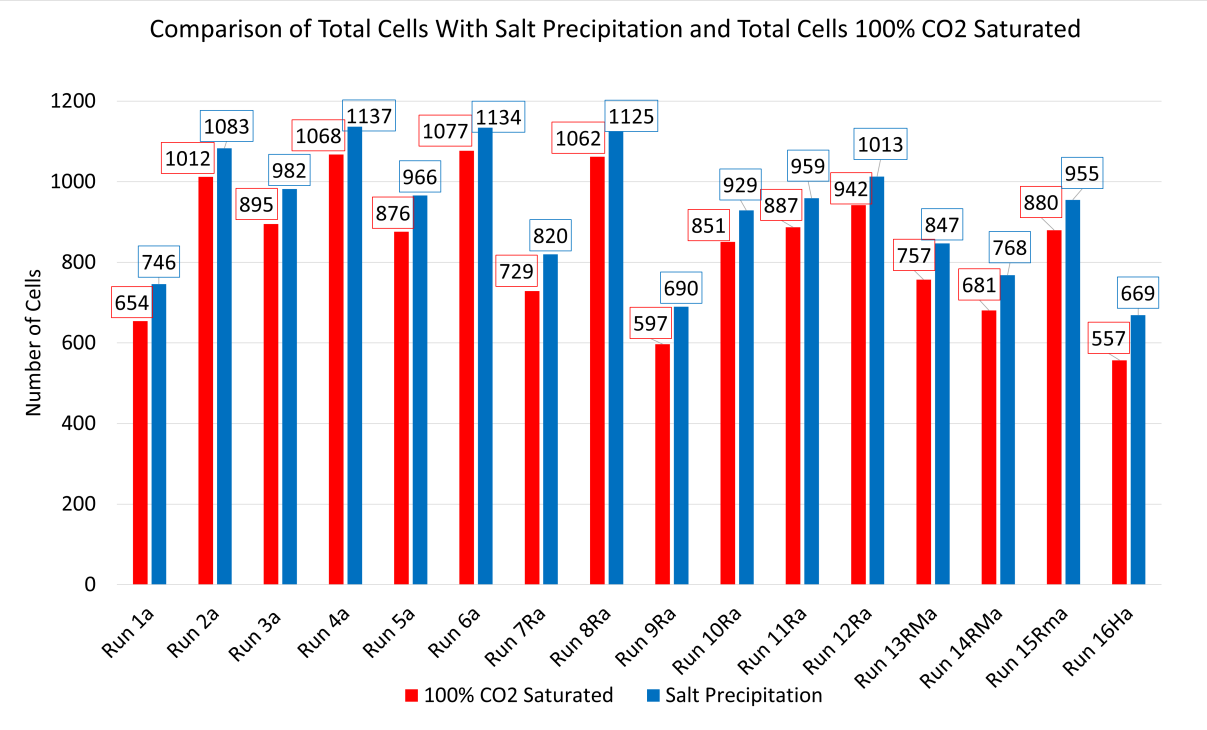

Figure 4.31: Comparison of total cells 100% saturated with CO_2 and total cells containing any fraction of precipitated salt for each run in the layered case. The red color illustrates cells that are 100% saturated with CO_2 at the end of injection, which forms the dry-out zone. The blue color represents total cells that contain any percentage (0-100%) of precipitated salt in the pore space. The vertical axis represents number of cells, which are highlighted with red and blue frames. The horizontal axes represents the run number.

Even though the more heterogeneous runs contained more total cells with salt, it did not clog the injection well and thus did not affect the injectivity of CO_2 to the same extent as in the more homogeneous reservoirs. An exception is Run 1a, which had much lower number of cells with salt precipitation than the other very heterogeneous runs. A reason for this could be the order of layering in the system. An observation based on Figure 4.31 is that the difference between cells with any salt precipitation and cells with 100% CO_2 saturation are large for the slightly heterogeneous runs and the homogeneous runs. As an example, Run 16H displays a total of 669 cells with salt precipitation and a total of 557 cells with 100% CO_2 saturation. The difference between them yields a total of 112 cells with salt precipitation that are not 100% CO_2 saturated. This illustrates that these cells are not located in the dry-out zone, and as previously found, they are located next to the well. In contrast, Run 8Ra, which is very heterogeneous, had a total of 1125 cells with salt precipitation and a total of 1062 cells that were 100% saturated with CO_2. The difference between these cells provides a total of 63 cells that are not located in the dry-out zone. This is significantly fewer cells than in Run 16RH, which further illustrates that solid salt has caused increased clogging next to the well in the homogeneous run.

Chapter 5

Conclusion

This thesis has investigated the effect of formation heterogeneity on the spatial distribution of salt precipitation numerically. Two models have been studied. One of them was a layered case, where a total of 16 runs including salt precipitation with different permeabilities, different order of layering, and various numbers of layers were simulated. A total of 16 runs excluding salt precipitation, with identical permeabilities as the runs with salt precipitation, have also been simulated. This provided an opportunity for comparison of how salt precipitation affected CO_2 saturation during and after injection into systems with varying degrees of heterogeneity. The second model was based on the 2D geometry of the SPE CSP 11B benchmark grid. Here, one run was simulated over 25 years with salt precipitation included, and one run was simulated over three years were it was not. Permeability was adjusted in two cells at the bottom of the injection well, and CO_2 saturation distribution was compared between the two runs.

Salt precipitation distribution was compared between the layered cases and the SPE CSP 11B benchmark case. In the very heterogeneous runs, the highest permeability layers had high fractions of solid salt near the injection well, which caused clogging, and effected injection of CO_2. The high permeability layers, which provided better flow capabilities, lead to capillary backflow having a better effect. In SPE CSP 11B case, the highest fractions of solid salt also occurred in the high permeability cell, however, as this case was simulated over a much longer time period, this cell did not have the highest fraction of solid salt at the end of injection.

The very heterogeneous runs were the least affected by high fractions of salt precipitation near the injection well. The homogeneous run and the slightly heterogeneous runs, however, had higher fractions of solid salt over longer vertical extents next to the injection well, which caused clogging and affected CO_2 saturation into the layers. These runs also had a higher bottom hole pressure out of any of the runs. The location of the dry-out zone in the homogeneous run and the slightly heterogeneous runs did, however, provide unexpected results.

The heterogeneous and very heterogeneous runs had the highest number of total cells with any fraction of salt precipitation at the end of injection. Even though more total cells in these systems

consisted of salt precipitation, it did not effect CO_2 saturation to the same degree as in the homogeneous and slightly heterogeneous runs, as it did not cause blocking near the injection well. Most of the cells with salt precipitation in these runs were located in the dry-out zone. This indicated that parallel distribution of salt precipitation into the layers was better than vertical distribution next to the injection well.

In systems where there was a significant ratio between the permeability of layers, high fractions of solid salt occurred in some cells at the border between them. This did, however, not affect injectivity to the same degree as when less fractions of solid salt were present in more cells next to the injection well. The systems where complexity was increased, with more total layers, displayed similar results as for the systems with fewer layers. The location of the dry-out zone was, however, more spread out between layers.

Based on the results of this study, formation heterogeneity effects the spatial distribution of salt precipitation during CO_2 injection, and the results align with available literature. Further research on more complex systems is necessary to understand how a real life reservoir is effected by salt precipitation during injection of CO_2.

Chapter 6

Future Work

This numerical study was performed to investigate effects of heterogeneity on the spatial distribution of salt precipitation. The subsequent effect on CO_2 saturation was also evaluated. Further research on the scope of this thesis could be conducted. Research topics could include the following:

- Study thermal effects by examining the impacts of salt precipitation distribution in a cold versus warm basin.
- Increasing heterogeneity by changing permeability in more cells in the SPE CSP 11B benchmark model.
- Study salt precipitation in the 3D geometry of the SPE CSP 11C benchmark model.
- A comparative study of salt precipitation between various simulators to see if results are in agreement.

Appendices

Appendix A

Configuration Files

A.1 Base Case Configuration Files

```
"""Set the full path to the flow executable and flags"""
flow --linear-solver=cprw --enable-tuning=true --enable-opm-rst-file=true --enable-well-operability-check=false--min-time-step-before-shutting-problematic-wells-in-days=1e-99

"""Set the model parameters"""
saltprec base #Model (co2store/h2store/co2eor/saltprec)
cake 60      #Grid type (radial/cartesian/cake) and size (width/theta/theta [in degrees])
10000 40.5     #Reservoir dimensions [m] (Lenght and height)
400 81 7.1   #Number of x- and z-cells [-] and exponential factor for the telescopic x-gridding
0.04 0 0     #Well diameter [m], well transmiscibility (0 to use the computed one internally in Flow), and remove the smaller cells than the well diameter
21.3e6 60 0  #Pressure [Pa] on the top, uniform temperature [°], and initial phase in the reservoir (0 wetting, 1 non-wetting)
-1 0         #Pore volume multiplier on the boundary [-] (0 to use well producers instead) and deactivate cross flow within the wellbore (see XFLOW in OPM Manual)
0 2 10       #Activate perforation [-], number of well perforations [-], and number of x-direction cells [-]
3 0 0 8.5e-10 #Number of layers [-], hysteresis (1 to activate), and econ for the producer (for h2 models)
138 268 2153 0.8 0.8 100001 1.3e-2 default #Ini salt conc [kg/m3], salt sol lim [kg/m3], prec salt den [kg/m3], gamma [-], phi_r [-], npoints [-], and threshold [-]
0            #The function for the reservoir surface

"""Set the saturation functions"""
((sw - swi) / (1.0 - swi - sni)) ** 4.0    #Wetting rel perm saturation function [-]
(1-((sw - swi) / (1.0 - swi - sni)) ** 2.0) * (1-(sw - swi) / (1.0 - swi - sni)) ** 2    #Non-wetting rel perm saturation function [-]
pec * (((sw - swi) / (1. - swi)) ** (-(1./npe)) - 1.) ** (1. - npe) #Capillary pressure saturation function [Pa]

"""Properties sat functions"""
"""swi [-], swrg [-], krg [-], krw [-], pe [Pa], threshold cP evaluation, ignore swi for cP?"""
SWI1 0.12 SNI1 0.15 KRW1 1 KRN1 1 PEC1 6120.00 NKRW1 0.457 NKRN1 0.457 NPE1 0.457 THRE1 6e-4 IGN1 0.23
SWI1 0.12 SNI1 0.15 KRW1 1 KRN1 1 PEC1 6120.00 NKRW1 0.457 NKRN1 0.457 NPE1 0.457 THRE1 6e-4 IGN1 0.23
SWI1 0.12 SNI1 0.15 KRW1 1 KRN1 1 PEC1 6120.00 NKRW1 0.457 NKRN1 0.457 NPE1 0.457 THRE1 6e-4 IGN1 0.23

"""Properties rock"""
"""Kx [mD], Kz [mD], phi [-], thickness [m]"""
PERMX2 1500. PERMZ2 1500. PORO2 0.20 THIC1 13.5
PERMX2 750. PERMZ2 750. PORO2 0.20 THIC1 13.5
PERMX2 150. PERMZ2 150. PORO2 0.20 THIC1 13.5

"""Define the injection values"""
"""injection time [d], time step size to write results [d], maximum time step [d], injected fluid (0 water, 1 co2), injection rates [kg/day]"""
0.1 .1 .0001 1 145800.0
0.4 .1 .001 1 145800.0
6 .1 .005 1 145800.0
30 .1 .01 1 145800.0
```

Figure A.1: Configuration file for the Base Case including salt precipitation.

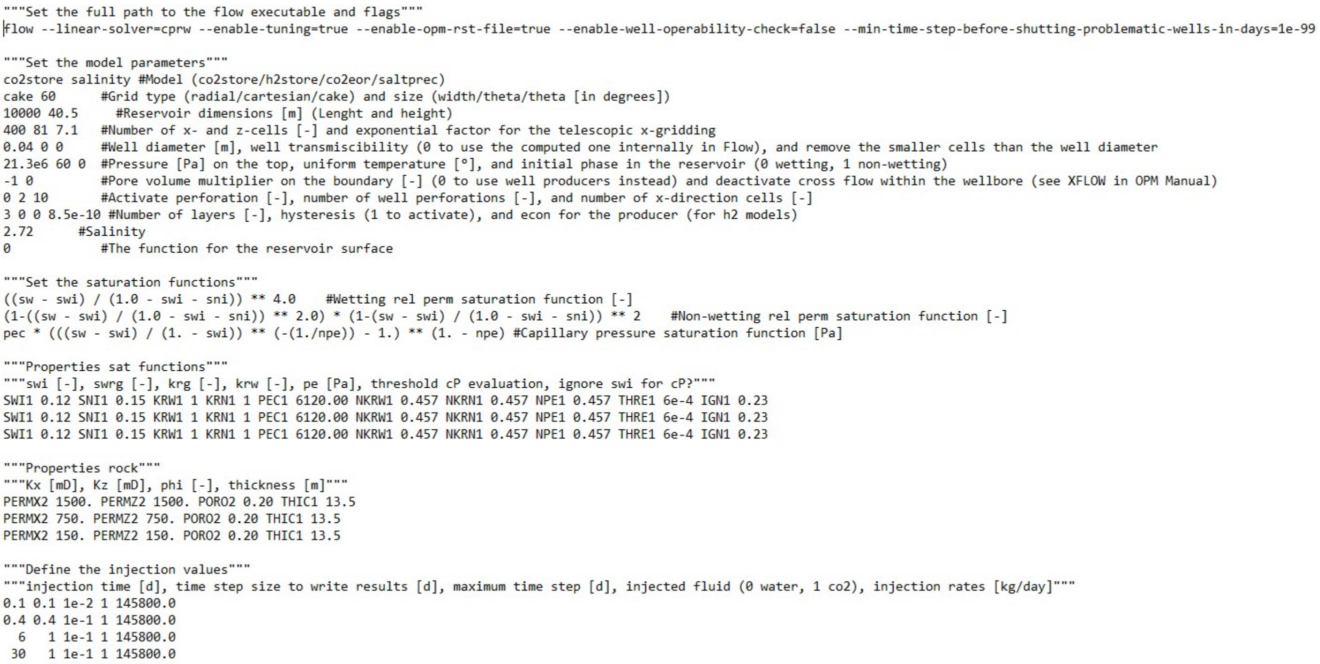

```
"""Set the full path to the flow executable and flags"""
flow --linear-solver=cprw --enable-tuning=true --enable-opm-rst-file=true --enable-well-operability-check=false --min-time-step-before-shutting-problematic-wells-in-days=1e-99

"""Set the model parameters"""
co2store salinity #Model (co2store/h2store/co2eor/saltprec)
cake 60      #Grid type (radial/cartesian/cake) and size (width/theta/theta [in degrees])
10000 40.5     #Reservoir dimensions [m] (Lenght and height)
400 81 7.1   #Number of x- and z-cells [-] and exponential factor for the telescopic x-gridding
0.04 0 0     #Well diameter [m], well transmiscibility (0 to use the computed one internally in Flow), and remove the smaller cells than the well diameter
21.3e6 60 0  #Pressure [Pa] on the top, uniform temperature [°], and initial phase in the reservoir (0 wetting, 1 non-wetting)
-1 0         #Pore volume multiplier on the boundary [-] (0 to use well producers instead) and deactivate cross flow within the wellbore (see XFLOW in OPM Manual)
0 2 10       #Activate perforation [-], number of well perforations [-], and number of x-direction cells [-]
3 0 0 8.5e-10 #Number of layers [-], hysteresis (1 to activate), and econ for the producer (for h2 models)
2.72      #Salinity
0             #The function for the reservoir surface

"""Set the saturation functions"""
((sw - swi) / (1.0 - swi - sni)) ** 4.0    #Wetting rel perm saturation function [-]
(1-((sw - swi) / (1.0 - swi - sni)) ** 2.0) * (1-(sw - swi) / (1.0 - swi - sni)) ** 2    #Non-wetting rel perm saturation function [-]
pec * (((sw - swi) / (1. - swi)) ** (-(1./npe)) - 1.) ** (1. - npe) #Capillary pressure saturation function [Pa]

"""Properties sat functions"""
"""swi [-], swrg [-], krg [-], krw [-], pe [Pa], threshold cP evaluation, ignore swi for cP?"""
SWI1 0.12 SNI1 0.15 KRW1 1 KRN1 1 PEC1 6120.00 NKRW1 0.457 NKRN1 0.457 NPE1 0.457 THRE1 6e-4 IGN1 0.23
SWI1 0.12 SNI1 0.15 KRW1 1 KRN1 1 PEC1 6120.00 NKRW1 0.457 NKRN1 0.457 NPE1 0.457 THRE1 6e-4 IGN1 0.23
SWI1 0.12 SNI1 0.15 KRW1 1 KRN1 1 PEC1 6120.00 NKRW1 0.457 NKRN1 0.457 NPE1 0.457 THRE1 6e-4 IGN1 0.23

"""Properties rock"""
"""Kx [mD], Kz [mD], phi [-], thickness [m]"""
PERMX2 1500. PERMZ2 1500. PORO2 0.20 THIC1 13.5
PERMX2 750. PERMZ2 750. PORO2 0.20 THIC1 13.5
PERMX2 150. PERMZ2 150. PORO2 0.20 THIC1 13.5

"""Define the injection values"""
"""injection time [d], time step size to write results [d], maximum time step [d], injected fluid (0 water, 1 co2), injection rates [kg/day]"""
0.1 0.1 1e-2 1 145800.0
0.4 0.4 1e-1 1 145800.0
  6   1 1e-1 1 145800.0
 30   1 1e-1 1 145800.0
```

Figure A.2: Configuration File for the Base Case excluding salt precipitation

A.2 SPE CSP 11B Configuration File

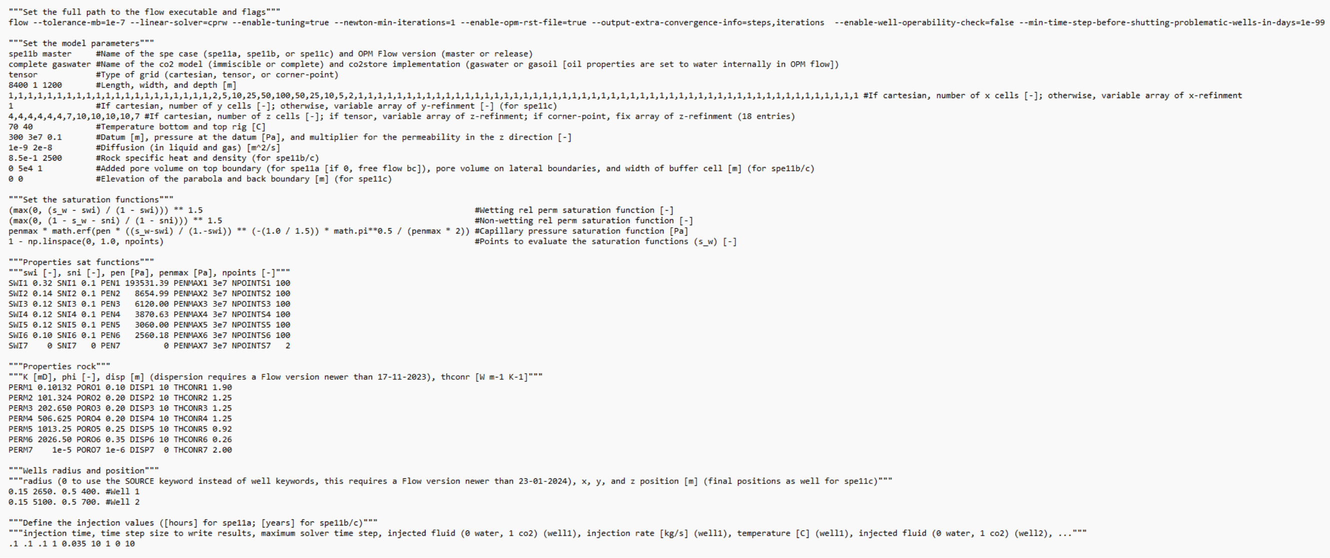

```
"""Set the full path to the flow executable and flags"""
flow --tolerance-mb=1e-7 --linear-solver=cprw --enable-tuning=true --newton-min-iterations=1 --enable-opm-rst-file=true --output-extra-convergence-info=steps,iterations  --enable-well-operability-check=false --min-time-step-before-shutting-problematic-wells-in-days=1e-99

"""Set the model parameters"""
spe11b master     #Name of the spe case (spe11a, spe11b, or spe11c) and OPM Flow version (master or release)
complete gaswater #Name of the co2 model (immiscible or complete) and co2store implementation (gaswater or gasoil [oil properties are set to water internally in OPM flow])
tensor            #Type of grid (cartesian, tensor, or corner-point)
8400 1 1200       #Length, width, and depth [m]
1,1,1,1,1,1,1,1,1,1,1,1,1,1,1,1,1,1,1,1,2,5,10,25,50,100,50,25,10,5,2,1,1,1,1,1,1,1,1,1,1,1,1,1,1,1,1,1,1,1,1,1,1,1,1,1,1,1,1,1,1,1,1,1,1,1,1,1,1,1,1,1,1,1,1,1,1,1,1,1,1,1,1,1 #If cartesian, number of x cells [-]; otherwise, variable array of x-refinment
1                 #If cartesian, number of y cells [-]; otherwise, variable array of y-refinment [-] (for spe11c)
4,4,4,4,4,4,7,10,10,10,10,7 #If cartesian, number of z cells [-]; if tensor, variable array of z-refinment; if corner-point, fix array of z-refinment (18 entries)
70 40             #Temperature bottom and top rig [C]
300 3e7 0.1       #Datum [m], pressure at the datum [Pa], and multiplier for the permeability in the z direction [-]
1e-9 2e-8         #Diffusion (in liquid and gas) [m^2/s]
8.5e-1 2500       #Rock specific heat and density (for spe11b/c)
0 5e4 1           #Added pore volume on top boundary (for spe11a [if 0, free flow bc]), pore volume on lateral boundaries, and width of buffer cell [m] (for spe11b/c)
0 0               #Elevation of the parabola and back boundary [m] (for spe11c)

"""Set the saturation functions"""
(max(0, (s_w - swi) / (1 - swi))) ** 1.5                                                        #Wetting rel perm saturation function [-]
(max(0, (1 - s_w - sni) / (1 - sni))) ** 1.5                                                    #Non-wetting rel perm saturation function [-]
penmax * math.erf(pen * ((s_w-swi) / (1.-swi)) ** (-(1.0 / 1.5)) * math.pi**0.5 / (penmax * 2)) #Capillary pressure saturation function [Pa]
1 - np.linspace(0, 1.0, npoints)                                                                #Points to evaluate the saturation functions (s_w) [-]

"""Properties sat functions"""
"""swi [-], sni [-], pen [Pa], penmax [Pa], npoints [-]"""
SWI1 0.32 SNI1 0.1 PEN1 193531.39 PENMAX1 3e7 NPOINTS1 100
SWI2 0.14 SNI2 0.1 PEN2   8654.99 PENMAX2 3e7 NPOINTS2 100
SWI3 0.12 SNI3 0.1 PEN3   6120.00 PENMAX3 3e7 NPOINTS3 100
SWI4 0.12 SNI4 0.1 PEN4   3870.63 PENMAX4 3e7 NPOINTS4 100
SWI5 0.12 SNI5 0.1 PEN5   3060.00 PENMAX5 3e7 NPOINTS5 100
SWI6 0.10 SNI6 0.1 PEN6   2560.18 PENMAX6 3e7 NPOINTS6 100
SWI7    0 SNI7   0 PEN7         0 PENMAX7 3e7 NPOINTS7   2

"""Properties rock"""
"""K [mD], phi [-], disp [m] (dispersion requires a Flow version newer than 17-11-2023), thconr [W m-1 K-1]"""
PERM1 0.10132 PORO1 0.10 DISP1 10 THCONR1 1.90
PERM2 101.324 PORO2 0.20 DISP2 10 THCONR2 1.25
PERM3 202.650 PORO3 0.20 DISP3 10 THCONR3 1.25
PERM4 506.625 PORO4 0.20 DISP4 10 THCONR4 1.25
PERM5 1013.25 PORO5 0.25 DISP5 10 THCONR5 0.92
PERM6 2026.50 PORO6 0.35 DISP6 10 THCONR6 0.26
PERM7    1e-5 PORO7 1e-6 DISP7  0 THCONR7 2.00

"""Wells radius and position"""
"""radius (0 to use the SOURCE keyword instead of well keywords, this requires a Flow version newer than 23-01-2024), x, y, and z position [m] (final positions as well for spe11c)"""
0.15 2650. 0.5 400. #Well 1
0.15 5100. 0.5 700. #Well 2

"""Define the injection values ([hours] for spe11a; [years] for spe11b/c)"""
"""injection time, time step size to write results, maximum solver time step, injected fluid (0 water, 1 co2) (well1), injection rate [kg/s] (well1), temperature [C] (well1), injected fluid (0 water, 1 co2) (well2), ..."""
.1 .1 .1 1 0.035 10 1 0 10
```

Figure A.3: Configuration file for SPE CSP 11B.

Appendix B

Data Files Including Salt Precipitation

B.1 Base Case Data File

```
-- Copyright (C) 2023 NORCE
--------------------------------------------------------------------------------

RUNSPEC

--------------------------------------------------------------------------------

DIMENS
400 1 81 /

WATER
GAS
BRINE
PRECSALT
VAPWAT
CO2STORE
DISGASW

METRIC

START
1 'JAN' 2000 /

EQLDIMS /

TABDIMS
3 1* 10000 /
```

```
WELLDIMS
81 81 1 81 /

UNIFIN
UNIFOUT
--------------------------------------------------
GRID
--------------------------------------------------

INCLUDE
'GEOLOGY.INC' /
--------------------------------------------------
PROPS
--------------------------------------------------
INCLUDE
'TABLES.INC' /

SALTSOL
268.0 2153.0/
/

ROCK
276.0 8.5e-10 /

INCLUDE
'PERMFACT.INC' /
--------------------------------------------------
REGIONS
--------------------------------------------------
INCLUDE
'REGIONS.INC' /
--------------------------------------------------
SOLUTION
--------------------------------------------------
EQUIL
0 213.0 0 0 0 0 1 1 0 /

SALTVD
0 138.0
```

```
40.5 138.0 /

RTEMPVD
0 60.0
40.5 60.0 /

RPTRST
'BASIC=2' FLOWS FLORES DEN VISC /
```

SUMMARY

```
CGIR
INJ0 /
/

CGIRL
INJ0 /
/

CPI
INJ0 /
/

WGIRL
'INJ0' 1 /
/

CGIT
INJ0 /
/

CGITL
INJ0 /
/

WGITL
'INJ0' 1 /
/
```

CPR
/

CPRL
INJ0 /
/

FPR

FGIP

FWIP

FGIR

FWIR

FGIT

FWIT

FWCD

WGIR
/

WGIT
/

WBHP
/

WPI
/

RPR
/

RWIP

```
/

RGIP
/
_____________________________________________

SCHEDULE
_____________________________________________

RPTRST
'BASIC=2' FLOWS FLORES DEN VISC PCOW PCOG /

WELSPECS
'INJ0' 'G1' 1 1 1* GAS 3* /
/

COMPDAT
'INJ0' 1 1 1 81 'OPEN' 1* 1* 0.04 /
/

TUNING
1e-2 0.0001 1e-10 2* 1e-12/
/
/

WCONINJE
'INJ0' 'GAS' OPEN
'RATE' 7.803343E+04 1* 400 /
/

TSTEP
1*0.1
/

TUNING
1e-2 0.001 1e-10 2* 1e-12/
/
/

WCONINJE
```

```
'INJ0' 'GAS' OPEN
'RATE' 7.803343E+04 1* 400 /
/

TSTEP
4*0.1
/

TUNING
1e-2 0.005 1e-10 2* 1e-12/
/
/

WCONINJE
'INJ0' 'GAS' OPEN
'RATE' 7.803343E+04 1* 400 /
/

TSTEP
60*0.1
/

TUNING
1e-2 0.01 1e-10 2* 1e-12/
/
/

WCONINJE
'INJ0' 'GAS' OPEN
'RATE' 7.803343E+04 1* 400 /
/

TSTEP
300*0.1
/
```

B.2 SPE CSP 11B Data File

```
– Copyright (C) 2023 NORCE
– This deck was generated by pyopmspe11
https://github.com/OPM/pyopmspe11

-------------------------------------------------------------------------------

RUNSPEC

-------------------------------------------------------------------------------

DIMENS
359 1 78 /

EQLDIMS
/

TABDIMS
7 1* 100 /

WATER
GAS
BRINE
PRECSALT
VAPWAT
CO2STORE
DISGASW

METRIC

START 1 'JAN' 2025 /

WELLDIMS
2 78 2 2 /

UNIFIN
UNIFOUT

-------------------------------------------------------------------------------

GRID

-------------------------------------------------------------------------------

INIT
INCLUDE
```

```
'DX.INC' /
DY
28002*1.0 /
INCLUDE
'DZ.INC' /
TOPS
359*0.0 /

INCLUDE
'PERMX.INC' /

COPY
PERMX PERMY /
PERMX PERMZ /
/

MULTIPLY
PERMZ 0.1 /
/

INCLUDE
'PORO.INC' /

EQUALS
PERMX 100 154 174 1 1 40 40 /
PERMZ 100 154 174 1 1 40 40 /
PERMX 1500 154 174 1 1 41 41 /
PERMZ 1500 154 174 1 1 41 41 /
/

----------

EDIT

----------

INCLUDE
'PVBOUNDARIES.INC' /

----------

PROPS

----------

INCLUDE
```

```
'TABLES.INC' /

SALTSOL
268.0 2153.0/
/

ROCK
276.0 8.5e-10 /

INCLUDE
'PERMFACT.INC' /
------------------------------------------------------------
REGIONS
------------------------------------------------------------
INCLUDE
'SATNUM.INC' /
INCLUDE
'FIPNUM.INC' /
------------------------------------------------------------
SOLUTION
------------------------------------------------------------
EQUIL
900.0 300.0 0 0 0 0 1 1 0 /

RPTRST
'BASIC=2' DEN PCGW/

SALTVD
0 138.0
1200.0 138.0 /

RTEMPVD
0 40.0
1200.0 70.0 /
------------------------------------------------------------
SUMMARY
------------------------------------------------------------
PERFORMA
FPR
```

```
FGIP
FGIR
FGIT
RGKDI
/
RGKDM
/
RGIP
/
RWCD
/
WBHP
/
WGIR
/
WGIT
/
BWPR
319 1 32 /
325 1 4 /
/
```

SCHEDULE

```
RPTRST
'BASIC=2' DEN RESIDUAL PCGW/

WELSPECS
'INJ0' 'G1' 164 1 1* 'GAS' 0.15/
/
COMPDAT
'INJ0' 164 1 37 41 'OPEN' 2* 0.3 /
/

TUNING
0.0001 1 1e-10 2* 1e-12/
/
/
WCONINJE
```

```
'INJ0' 'GAS' OPEN
'RATE' 1.618471E+03 1* 400/
/
TSTEP
50*182.5
/
```

Appendix C

Data Files Excluding Salt Precipitation

C.1 Base Case Data File

```
-- Copyright (C) 2024 NORCE
--------------------------------------------------------------------------
RUNSPEC
--------------------------------------------------------------------------
DIMENS
400 1 81 /

WATER
GAS
CO2STORE
DISGASW

METRIC

START
1 'JAN' 2000 /

EQLDIMS
/

TABDIMS
3 1* 10000 /

WELLDIMS
81 81 1 81 /
```

UNIFIN
UNIFOUT

GRID

INCLUDE
'GEOLOGY.INC' /

PROPS

INCLUDE
'TABLES.INC' /

ROCK
276.0 8.5e-10 /

SALINITY
$2.72/35-40g/l \rightarrow 35-40g/kg \rightarrow 0.63-0.72mol/g$

REGIONS

INCLUDE
'REGIONS.INC' /

SOLUTION

EQUIL
0 213.0 0 0 0 0 1 1 0 /

RTEMPVD
0 60.0
40.5 60.0 /

RPTRST
'BASIC=2' FLOWS FLORES DEN VISC /

SUMMARY

```
CGIR
INJ0 /
/

CGIRL
INJ0 /
/

CPI
INJ0 /
/

WGIRL
'INJ0' 1 /
/

CGIT
INJ0 /
/

CGITL
INJ0 /
/

WGITL
'INJ0' 1 /
/

CPR
/

CPRL
INJ0 /
/

FPR

FGIP
```

```
FWIP

FGIR

FWIR

FGIT

FWIT

FWCD

WGIR
/

WGIT
/

WBHP
/

WPI
/

RPR
/

RWIP
/

RGIP
/

----------

SCHEDULE

----------

RPTRST
'BASIC=2' FLOWS FLORES DEN VISC PCOW PCOG /
```

```
WELSPECS
'INJ0' 'G1' 1 1 1* GAS 3* /
/
COMPDAT
'INJ0' 1 1 1 81 'OPEN' 1* 1* 0.04 /
/
TUNING
1e-2 0.01 1e-10 2* 1e-12/
/
/
WCONINJE
'INJ0' 'GAS' OPEN
'RATE' 7.803343E+04 1* 400 /
/
TSTEP
1*0.1
/
TUNING
1e-2 0.1 1e-10 2* 1e-12/
/
/
WCONINJE
'INJ0' 'GAS' OPEN
'RATE' 7.803343E+04 1* 400 /
/
TSTEP
1*0.4
/
TUNING
1e-2 0.1 1e-10 2* 1e-12/
/
/
WCONINJE
'INJ0' 'GAS' OPEN
'RATE' 7.803343E+04 1* 400 /
/
TSTEP
6*1.0
/
```

```
TUNING
1e-2 0.1 1e-10 2* 1e-12/
/
/
WCONINJE
'INJ0' 'GAS' OPEN
'RATE' 7.803343E+04 1* 400 /
/
TSTEP
30*1.0
```

C.2 SPE CSP 11B Data File

```
– Copyright (C) 2023 NORCE
– This deck was generated by pyopmspe11
https://github.com/OPM/pyopmspe11
------------------------------------------------------------

RUNSPEC

------------------------------------------------------------

DIMENS
359 1 78 /

EQLDIMS
/

TABDIMS
7 1* 100 /

WATER
GAS
CO2STORE
DISGASW

METRIC

START
1 'JAN' 2025 /
```

```
WELLDIMS
2 78 2 2 /

UNIFIN
UNIFOUT
--------------------------------------------------
GRID
--------------------------------------------------
INIT
INCLUDE
'DX.INC' /
DY
28002*1.0 /
INCLUDE
'DZ.INC' /
TOPS
359*0.0 /

INCLUDE
'PERMX.INC' /

COPY
PERMX PERMY /
PERMX PERMZ /
/

MULTIPLY
PERMZ 0.1 /
/

INCLUDE
'PORO.INC' /

EQUALS
PERMX 100 154 174 1 1 40 40 /
PERMZ 100 154 174 1 1 40 40 /
PERMX 1500 154 174 1 1 41 41 /
PERMZ 1500 154 174 1 1 41 41 /
```

/

EDIT

INCLUDE
'PVBOUNDARIES.INC' /

PROPS

INCLUDE
'TABLES.INC' /

ROCK
276.0 8.5e-10 /

SALINITY
$2.72/35-40g/l \rightarrow 35-40g/kg \rightarrow 0.63-0.72mol/g$

REGIONS

INCLUDE
'SATNUM.INC' /
INCLUDE
'FIPNUM.INC' /

SOLUTION

EQUIL
900.0 300.0 0 0 0 0 1 1 0 /

RPTRST
'BASIC=2' DEN PCGW/

RTEMPVD
0 40.0
1200.0 70.0 /

SUMMARY

```
PERFORMA
FPR
FGIP
FGIR
FGIT
RGKDI
/
RGKDM
/
RGIP
/
RWCD
/
WBHP
/
WGIR
/
WGIT
/
BWPR
319 1 32 /
325 1 4 /
/
------------------------------------------------------------
SCHEDULE
------------------------------------------------------------
RPTRST
'BASIC=2' DEN RESIDUAL PCGW/

WELSPECS
'INJ0' 'G1' 164 1 1* 'GAS' 0.15/
/
COMPDAT
'INJ0' 164 1 37 41 'OPEN' 2* 0.3 /
/

TUNING
0.0001 1 1e-10 2* 1e-12/
/
```

```
/
WCONINJE
'INJ0' 'GAS' OPEN
'RATE' 1.618471E+03 1* 400/
/
TSTEP
50*36.5
/
```

Bibliography

Abdoulghafour, H., Sarmadivaleh, M., Hauge, L. P., Fernø, M., & Iglauer, S. (2020). Capillary pressure characteristics of co2-brine-sandstone systems. *International Journal of Greenhouse Gas Control*, *94*, 102876. https://doi.org/10.1016/j.ijggc.2019.102876.

Akindipe, D., Saraji, S., & Piri, M. (2021). Salt precipitation during geological sequestration of supercritical co2 in saline aquifers: A pore-scale experimental investigation. *Advances in Water Resources*, *155*, 104011. https://doi.org/10.1016/j.advwatres.2021.104011.

Akindipe, D., Saraji, S., & Piri, M. (2022). Salt precipitation in carbonates during supercritical co2 injection: A pore-scale experimental investigation of the effects of wettability and heterogeneity. *International Journal of Greenhouse Gas Control*, *121*, 103790. https://doi.org/10.1016/j.ijggc.2022.103790.

Anderson, W. G. (1987). Wettability Literature Survey Part 4: Effects of Wettability on Capillary Pressure. *Journal of Petroleum Technology*, *39(10)*, 1283–1300. https://doi.org/10.2118/15271-PA.

Bacci, G., Korre, A., & Durucan, S. (2011). Experimental investigation into salt precipitation during co2 injection in saline aquifers. *Energy Procedia*, *4*, 4450–4456. https://doi.org/10.1016/j.egypro.2011.02.399.

Bachu, S. (2015). Review of co2 storage efficiency in deep saline aquifers. *International Journal of Greenhouse Gas Control*, *40*, 188–202. https://doi.org/10.1016/j.ijggc.2015.01.007.

Baxendale, D. (2023). OPM Flow Referance Manual. Retrieved February 1, 2024 from https://opm-op.com/manual/OPM_Flow_Reference_Manual_2023-10_Rev-0.pdf.

Benson, S., Cook, P., Andersen, J., Bachu, S., Nimir, H. B., Basu, B., Bradshaw, J., Deguchi, G., Gale, J., von Goerne, G., Heidung, W., Holloway, S., Kamal, R., Keith, D., Lloyd, P., Rocha, P., Senior, B., Thomson, J., Torp, T., Wildenborg, T., Wilson, M., Zarlenga, F., & Zhou, D. (2005). Chapter 5 - Underground geological storage. IPCC Special Report on CO2 capture and sequestration. (pp. 197–265). https://www.researchgate.net/publication/264

453028_Capter_5_-_Underground_geological_storage_IPCC_Special_Report_on_CO2_capture_and_sequestration.

Berntsen, A., Todorovic, J., Raphaug, M., Torsæter, M., Panduro, E. A. C., & Gawel, K. (2019). Salt clogging during supercritical CO2 injection into a downscaled borehole model. *International Journal of Greenhouse Gas Control*, *86*, 201–210. https://doi.org/10.1016/j.ijggc.2019.04.009.

Celia, M. A., Bachu, S., Nordbotten, J. M., & Bandilla, K. W. (2015). Status of CO2 storage in deep saline aquifers with emphasis on modeling approaches and practical simulations. *Water Resources Research*, *51(9)*, 6846–6892. https://doi.org/10.1002/2015WR017609.

Chadwick, R. A., Zweigel, P., Gregersen, U., Kirby, G. A., Holloway, S., & Johannessen, P. N. (2004). Geological reservoir characterization of a CO2 storage site: The Utsira Sand, Sleipner, northern North Sea. *Energy*, *29(9)*, 1371–1381. https://doi.org/10.1016/j.energy.2004.03.071.

Corey, A. T. (1954). The interrelation between gas and oil relative permeabilities. Prod. Mon 19 (1), 38-41.

Edem, D. E., Abba, M. K., Nourian, A., Babaie, M., & Naeem, Z. (2022). Experimental Study on the Interplay between Different Brine Types/Concentrations and CO2 Injectivity for Effective CO2 Storage in Deep Saline Aquifers. *Sustainability*, *14 (2)*, 986. 10.3390/su14020986.

Fernø, M. A., Haugen, M., Eikehaug, K., Folkvord, O., Benali, B., Both, J. W., Storvik, E., Nixon, C. W., Gawthrope, R. L., & Nordbotten, J. M. (2023). Room-Scale CO2 Injections in a Physical Reservoir Model with Faults. *Transport in Porous Media*, *151*, 913–937. https://doi.org/10.1007/s11242-023-02013-4.

Flett, M., Gurton, R., & Weir, G. (2007). Heterogeneous saline formations for carbon dioxide disposal: Impact of varying heterogeneity on containment and trapping. *Journal of Petroleum Science and Engineering*, *57(1)*, 106–118. https://doi.org/10.1016/j.petrol.2006.08.016.

Guyant, E., Han, W. S., Kim, K. Y., Park, M. H., & Kim, B. Y. (2015). Salt precipitation and co2/brine flow distribution under different injection well completions. *International Journal of Greenhouse Gas Control*, *37*, 299–310. https://doi.org/10.1016/j.ijggc.2015.03.020.

He, D., Jiang, P., & Xu, R. (2019). Pore-Scale Experimental Investigation of the Effect of Supercritical CO2 Injection Rate and Surface Wettability on Salt Precipitation. *Environmental Science and Technology*, *53(24)*, 14744–14751. https://doi.org/10.1021/acs.est.9b03323.

Huang, M. T., & Zhai, P. M. (2021). Achieving Paris Agreement temperature goals requires carbon neutrality by middle century with far-reaching transitions in the whole society. *Advances in Climate Change Research*, *12(2)*, 281–286. https://doi.org/10.1016/j.accre.2021.03.004.

IEA (2020). *The role of CCUS in low-carbon power systems*, IEA, Paris. Retrieved April 26, 2024 from https://www.iea.org/reports/the-role-of-ccus-in-low-carbon-power-systems, Licence: CC BY 4.0.

IEA (2021). *The world has vast capacity to store CO2: Net zero means we'll need it*, IEA, Paris. Retrieved May 20, 2024 from https://www.iea.org/commentaries/the-world-has-vast-capacity-to-store-co2-net-zero-means-we-ll-need-it.

Intergovenmental Panel on Climate Change (IPCC) (2023). *Climate Change 2022 - Mitigation of Climate Change: Working Group III Contribution to the Sixth Assessment Report of the Intergovernmental Panel on Climate Change.*. Cambridge: Cambridge University Press. https://doi.org/10.1017/9781009157926.

Intergovernmental Panel on Climate Change (IPCC) (n.d.). *About the IPCC*. Retrieved April 28, 2024 from https://www.ipcc.ch/about/.

Khalili, Y., & Ahmadi, M. (2023). Reservoir Modeling Simulation: Advancements, Challenges, and Future Perspectives. *Journal of Chemical and Petroleum Engineering*, *57(2)*, 343–364. https://doi.org/10.22059/JCHPE.2023.363392.1447.

Kim, K., Kim, D., Na, Y., Song, Y., & Wang, J. (2023). A review of carbon mineralization mechanism during geological CO2 storage. *Heliyon*, *9(12)*, e23135. https://doi.org/10.1016/j.heliyon.2023.e23135.

Krevor, S., de Coninck, H., Gasda, S. E., Ghaleigh, N. S., de Gooyert, V., Hajibeygi, H., Juanes, R., Neufeld, J., Roberts, J. J., & Swennenhuis, F. (2023). Subsurface carbon dioxide and hydrogen storage for a sustainable energy future. *Nature Reviews Earth and Environment*, *4(2)*, 102–118. https://doi.org/10.1038/s43017-022-00376-8.

Landa-Marbán, D., Zamani, N., Sandve, T. H., & Gasda, S. E. (2024). *Impact of Intermittency on Salt Precipitation During CO2 Injection*. Paper presented at the SPE Norway Subsurface Conference, Bergen, Norway, April 2024. https://doi.org/10.2118/218477-MS.

Landa-Merban, D., Franc, J., & Møyner, O. (2023). pyopmspe11: A Python framework using OPM Flow for the SPE11 benchmark project. Retrieved February 15, 2024 from https://github.com/OPM/pyopmspe11.

Landa-Merban, D., & von Schultzendorff, P. M. (2023). pyopmnearwell: A Python framework to simulate near well dynamics using OPM Flow. Retrieved November 1, 2023 from https://github.com/daavid00/pyopmnearwell.

Liu, H. H., Zhang, G., Yi, Z. L., & Wang, Y. (2013). A permeability-change relationship in the dryout zone for CO2 injection into saline aquifers. *International Journal of Greenhouse Gas Control*, *15*, 42–47. https://doi.org/10.1016/j.ijggc.2013.01.034.

Loizzo, M., Lecampion, B., Bérard, T., Harichandran, A., & Jammes, L. (2010). Reusing OG-Depleted Reservoirs for CO2 Storage: Pros and Cons. *SPE Projects, Facilities Construction*, *5(3)*, 166–172. https://doi.org/10.2118/124317-PA.

Miri, R. (2015), . *Effects of CO2-Brine-Rock Interactions on CO2 Injectivity - Implications for CCS* [Doctoral dissertation, University of Oslo]. DUO vitnearkiv. https://www.duo.uio.no/handle/10852/48598.

Miri, R., & Hellevang, H. (2016). Salt precipitation during CO2 storage-A review. *International Journal of Greenhouse Gas Control*, *51*, 136–147. https://doi.org/10.1016/j.ijggc.2016.05.015.

Miri, R., van Noort, R., Aagaard, P., & Hellevang, H. (2015). New insights on the physics of salt precipitation during injection of CO2 into saline aquifers. *International Journal of Greenhouse Gas Control*, *43*, 10–21. https://doi.org/10.1016/j.ijggc.2015.10.004.

Nordbotten, J. M., & Celia, M. A. (2011). *Geological Storage of CO2: Modeling Approaches for Large-Scale Simulation*. John Wiley Sons, Inc.

Nordbotten, J. M., Celia, M. A., & Bachu, S. (2005). Injection and Storage of CO2 in Deep Saline Aquifers: Analytical Solution for CO2 Plume Evolution During Injection. *Transport in Porous Media*, *58*, 339–360. https://doi.org/10.1007/s11242-004-0670-9.

Nordbotten, J. M., Ferno, M. A., Flemisch, B., Kovscek, A. R., & Lie, K.-A. (2024). The 11th Society of Petroleum Engineers Comparative Solution Project: Problem Definition. *SPE Journal*, *29(5)*, 1–18. URL: https://dx.doi.org/10.2118/218015-PA. https://doi.org/10.2118/218015-PA.

Norouzi, A. M., Babaei, M., Han, W. S., Kim, K. Y., & Niasar, V. (2021). CO2-plume geothermal processes: A parametric study of salt precipitation influenced by capillary-driven backflow. *Chemical Engineering Journal*, *425*, 130031. https://doi.org/10.1016/j.cej.2021.130031.

Ott, H., Kloe, K., Taberner, C., Marcelis, F., Wang, Y., & Makurat, A. (2010). Rock/fluid interaction by injection of supercritical CO2/H2S: Investigation of dry-zone formation near

the injection well. *Society of Core Analysis Conference Paper SCA2010-20*, . https://www.researchgate.net/publication/266493644_Rockfluid_interaction_by_injection_of_supercritical_CO2H2S_Investigation_of_dry-zone_formation_near_the_injection_well.

Ott, H., Kloe, K. D., Bakel, M. V., Vos, F., Pelt, A. V., Legerstee, P., Bauer, A., Eide, K., Linden, A. V. D., Berg, S., & Makurat, A. (2012). Core-flood experiment for transport of reactive fluids in rocks. *Review of Scientific Instruments*, *83(8)*, 84501. https://doi.org/10.1063/1.4746997.

Ott, H., Roels, S. M., & de Kloe, K. (2015). Salt precipitation due to supercritical gas injection: I. Capillary-driven flow in unimodal sandstone. *International Journal of Greenhouse Gas Control*, *43*, 247–255. https://doi.org/10.1016/j.ijggc.2015.01.005.

Pettersen, O. (2006), . *Basics of Reservoir Simulation With the Eclipse Reservoir Simulator* [PDF]. https://mj-oystein.no/index_htm_files/ResSimNotes.pdf.

Peysson, Y., André, L., & Azaroual, M. (2014). Well injectivity during CO2 storage operations in deep saline aquifers—Part 1: Experimental investigation of drying effects, salt precipitation and capillary forces. *International Journal of Greenhouse Gas Control*, *22*, 291–300. https://doi.org/10.1016/j.ijggc.2013.10.031.

Pruess, K., & Müller, N. (2009). Formation dry-out from CO2 injection into saline aquifers: 1. Effects of solids precipitation and their mitigation. *Water Resources Research*, *45(3)*. https://doi.org/10.1029/2008WR007101.

Rasmussen, A. F., Sandve, T. H., Bao, K., Lauser, A., Hove, J., Skaflestad, B., Klöfkorn, R., Blatt, M., Rustad, A. B., Sævareid, O., Lie, K. A., & Thune, A. (2021). The Open Porous Media Flow reservoir simulator. *Computers Mathematics with Applications*, *81*, 159–185. https://doi.org/10.1016/j.camwa.2020.05.014.

ResInsight (n.d.). *About*. ResInsight. Retrieved May 19, 2024 from https://resinsight.org/about/.

Ringrose, P. (2020). *How to Store CO2 Underground: Insights from early-mover CCS Projects* Springer. https://doi.org/10.1007/978-3-030-33113-9.

Roels, S. M., Ott, H., & Zitha, P. L. (2014). μ-CT analysis and numerical simulation of drying effects of CO2 injection into brine-saturated porous media. *International Journal of Greenhouse Gas Control*, *27*, 146–154. https://doi.org/10.1016/j.ijggc.2014.05.010.

Society of Petroleum Engineers (2023). *The 11th Society of Petroleum Engineers Comparative Solution Project*. Retrieved April 29, 2024 from https://www.spe.org/en/csp/.

Sun, X., Cao, Y., Liu, K., Alcalde, J., Cabello, P., Travé, A., Cruset, D., & Gomez-Rivas, E. (2023). Effects of fluvial sedimentary heterogeneity on co2 geological storage: Integrating storage capacity, injectivity, distribution and co2 phases. *Journal of Hydrology*, *617*, 128936. https://doi.org/10.1016/j.jhydrol.2022.128936.

Tiab, D., & Donaldson, E. C. (2012). *Chapter 3 - Porosity and Permeability*. In D. Tiab, & E. C. Donaldson (Eds.), *Petrophysics (Third Edition)* (pp. 85–219). Gulf Professional Publishing. https://doi.org/10.1016/B978-0-12-383848-3.00003-7.

UNFCCC (n.d.). *The Paris Agreement. What is the Paris Agreement?* United Nations Climate Change. Retrieved May 26, 2024 from https://unfccc.int/process-and-meetings/the-paris-agreement.

United Nations (2022). *Renewable energy – powering a safer future*. United Nations. Retrieved April 26, 2024 from https://www.un.org/en/climatechange/raising-ambition/renewable-energy.

United Nations (n.d.). *Causes and Effects of Climate Change*. United Nations. Retrieved January 18, 2024 from https://www.un.org/en/climatechange/science/causes-effects-climate-change.

Wang, D. (2013). *Chapter 4 - Polymer Flooding Practice in Daqing*. Sheng, J, J. (Eds.), *Enchanced Oil Recovery Field Case Studies* (pp. 83-116). Gulf Professional Publishing. https://doi.org/10.1016/B978-0-12-386545-8.00004-X.

Yang, J., Lei, T., Wang, G., Xu, Q., Chen, J., & Luo, K. H. (2023). Lattice Boltzmann modelling of salt precipitation during brine evaporation. *Advances in Water Resources*, *180*, 104542. https://doi.org/10.1016/j.advwatres.2023.104542.

Zeidouni, M., Pooladi-Darvish, M., & Keith, D. (2009). Analytical solution to evaluate salt precipitation during CO2 injection in saline aquifers. *International Journal of Greenhouse Gas Control*, *3(5)*, 600–611. https://doi.org/10.1016/j.ijggc.2009.04.004.

Zhang, D., & Song, J. (2013). Mechanisms for Geological Carbon Sequestration. *Procedia IUTAM*, *10*, 319–327. https://doi.org/10.1016/j.piutam.2014.01.027.

Zhang, H., Sun, Z., Zhang, N., & Zhao, B. (2024). Brine Drying and Salt Precipitation in Porous Media: A Microfluidics Study. *Water Resources Research*, *60(1)*. https://doi.org/10.1029/2023WR035670.

Zolotukhin, A. B., & Ursin, J.-R. (2000). *Introduction to Petroleum Reservoir Engineering*. Høyskoleforlaget AS.